Physics of the Cosmos (PCOS)
Program Technology Development
2018

Program Technology Development Quad Charts

Directly Deposited Optical-Blocking Filters for Imaging X-ray Detectors

PI: Mark Bautz / MIT Kavli Institute

Objective and Key Challenges:

- Silicon imaging X-ray detectors require thin filters (< 300 nm) to block noise/background from UV and optical light
- State-of-the-art, free-standing filters use fragile, thin substrates
- Objective: deposit blocking filter directly on CCD X-ray detector, eliminating substrate
- Challenges:
  — Deposit filter directly without compromising CCD performance
  — Deposit sufficiently thin, uniform filters

Significance of Work:

- Filter deposited on detector requires no fragile substrate
- Allows cheaper, more robust sensors (no vacuum housing!)
- Improves crucial soft-X-ray QE and enables larger focal planes

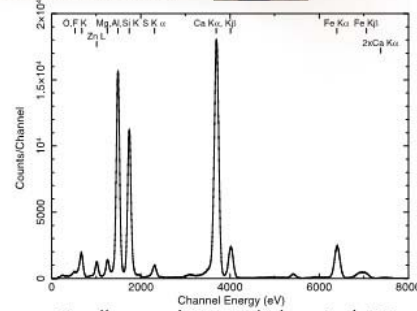Excellent resolution with deposited OBF

Approach:

- Exploit existing stocks of (engineering grade/flight spare) X-ray CCD detectors at MIT Lincoln Laboratory
- Screen, thin, passivate, package, and apply filters to detectors
- Filter is Al with AlO_2 cap
- Start thick (220-nm Al), get progressively thinner
- Use existing MIT facilities for X-ray characterization
- Use existing and upgraded facilities for optical characterization

Key Collaborators:

- Bautz, Kissel, Thayer et al. (MIT Kavli Institute)
- Suntharalingam, Ryu, Burke, and O'Brien (MIT Lincoln Laboratory)
- Masterson, Chodas, and Megerssa (MIT Dept. of Aero. and Astro.)

Current Funded Period of Performance:

Jul 2012 – Jun 2018

Recent Accomplishments:

- ✓ Reduced pinhole fraction to < 1% (OD < 7) for 220-nm OBF
- ✓ Tested devices with 70-nm and 100-nm-thick Al OBF; optical blocking as expected
- ✓ With REXIS, developed and qualified underside coating as effective countermeasure for near-IR leakage through package
- ✓ Supported environmental tests of REXIS flight CCDs/OBFs through launch
- ✓ Students developed and secured PCOS approval for TRL-6 demo plan; vibe and thermal cycling completed successfully to modified plan

Next Milestone:

- Request final TRL assessment, surpassing project goals (2018)

Applications:

Every X-ray imaging or grating spectroscopy mission
- Explorers (Arcus, STAR-X, TAO-ISS, etc.)
- Probes (TAP, AXIS, etc.)
- Flagship (Athena, Lynx)

$TRL_{In} = 5$ $TRL_{Current} = 5$ $TRL_{Target} = 6$

Providing Enabling & Enhancing Technologies for a Demonstration Model of the Athena X-IFU

PI: Caroline Kilbourne / GSFC

Objectives and Key Challenges:

- Develop and deliver large-format arrays of X-ray microcalorimeters for the Athena (ESA's L2 mission) X-ray Integral Field Unit (X-IFU)
- Optimize performance of arrays when read out using ESA's baselined frequency-division multiplexed (FDM) readout technique
- Develop time-division (TDM) and code-division (CDM) multiplexing capability to screen large-format arrays, and to potentially provide backup multiplexed readout capability

Significance of Work:

- Provides key technology for the X-IFU Instrument on Athena to allow high-resolution spectroscopy with high spatial resolution and wide field of view

X-IFU scale calorimeter array mounted on testing setup with similar design as X-IFU Focal Plane Assembly

Approach:

- Develop microcalorimeters with superconducting Transition Edge Sensors (TES); Mo/Au TES with Au/Bi X-ray absorbers
- Improve understanding of underlying physics to optimize TES design for FDM or TDM readout
- Produce large arrays of pixels designed for X-IFU with optimal performance, uniformity, and robustness
- Advance TDM and CDM readout technology

Key Collaborators:

- J. Adams, S. Bandler, M. Eckart, F. Finkbeiner, R. Kelley, A. Miniussi, F.S. Porter, K. Sakai, S. Smith, N. Wakeham, R. Hummatov, S. Beaumont, J. Chervenak, A. Datesman, A. Ewin, J. Sadleir, and E. Wassell (GSFC)
- J. Ullom, D. Bennett, W. Doriese, C. Reintsema, and D. Swetz (NIST)
- K. Irwin (Stanford)

Current Funded Period of Performance:

Oct 2015 – Sep 2028

Recent Accomplishments:

- ✓ Improved performance of TES when read out with FDM.
- ✓ Delivered demonstration model array for testing
- ✓ Completed report on implications of TDM as backup readout.
- ✓ Produced fight-scale array and continued development of test setup

Next Milestones:

- First tests of flight-scale arrays
- TDM demonstration of kilo-pixel array of latest TES designs

Application:

- Contribution to the X-ray Integral Field Unit instrument on the ESA Athena mission
- Other potential missions needing high-resolution imaging x-ray spectroscopy

$$TRL_{In} = 4 \quad TRL_{Current} = 4 \quad TRL_{Target} = 6$$

Hybrid Lightweight X-ray Optics for Half-Arcsec Imaging
PI: Paul Reid / SAO

Objectives and Key Challenges:

- Develop lightweight, thin, sub-arcsec grazing-incidence X-ray optics suitable for the Lynx mission concept
- Key challenges:
  - Combination of adjustable optics and differential deposition
  - Need correction bandwidths of both technologies to overlap

Significance of Work:

- Adjustable optics cannot correct all errors – those higher frequency than $1/(2 \times$ adjuster size) cannot be corrected
- Differential deposition is most efficient for mid-frequency errors
- Marrying the two technologies improves the probability of successfully meeting Lynx mirror-figure requirements on thin, lightweight segments

Approach:

- Combine low-spatial-frequency error correction of adjustable X-ray optics with mid-frequency correction of differential deposition
- Apply continuous thin-film piezoelectric material to backside of Wolter segment to correct low-frequency fabrication and mounting errors as well as enable on-orbit thermal-error correction
- Apply differential deposition on front side of segments to correct mid-spatial frequency errors

Key Collaborators:

- C. Deroo, V. Cotroneo, V. Marquez, D. Schwartz, E. Schwartz, and A. Vikhlinin (SAO)
- S. Trolier-McKinstry, J. Walker, T. Jackson, T. Liu, and M. Tandulkar (PSU)
- B. Ramsey, S. O'Dell K. Kilaru, and D. Broadway (MSFC)

Current Funded Period of Performance:

02/21/17 – 02/20/19 (initial funding 05/10/17)

Iterative Correction of HFDFC3:
Figure Space Using Savitsky-Golay Filtered IFs
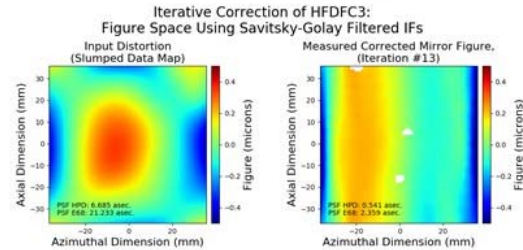
Deterministic control of mirror figure: test mirror with 112 adjusters corrected figure error (left, 7") to within 0.5" of predicted value (right)

Recent Accomplishments:

- ✓ Improved adjustable mirror-figure control to within better than 0.5 arcsec of predicted value
- ✓ Verified slumped mirror surface roughness meets Lynx requirement

Next Milestones:

- MSFC facilitize for differential deposition on segments (Oct 2018)
- Improve mirror mount (Sep 2018)
- Fabricate hybrid mirror segment (Feb 2019)

Applications:

- Lynx Mission Concept

$TRL_{In} = 2$ $TRL_{Current} = 2$ $TRL_{Target} = 3$

Development of a Critical-Angle Transmission Grating Spectrometer

PI: Mark Schattenburg / MIT MKI

### Objectives and Key Challenges:

- Develop key technology to enable a Critical-Angle X-ray Transmission Grating Spectrometer (CATGS), advancing to TRL 6 in preparation for proposed mid- and large-size missions over the next decade
- Develop improved grating fabrication processes
- Develop frame mounting, alignment, and assembly techniques for CAT grating arrays

Significance of Work:

- Improved diffraction efficiency and resolving power for CATGS
- Ability to manufacture large-area, light-weight grating arrays
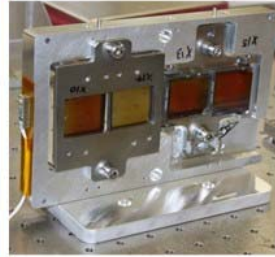
Four large co-aligned CAT gratings
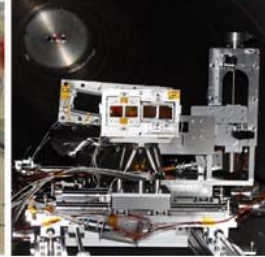
Test setup at Panter X-ray facility: two co-aligned SPOs (not visible) are illuminating all four gratings simultaneously

Approach:

- Integrated wafer front/back-side fabrication process using silicon-on-insulator (SOI) wafers
- Fabrication combines DRIE with silicon polishing in KOH
- Wafer front side: CAT grating and Level 1 support structure
- Wafer back side: Level 2 support mesh structure
- Bonded to flexured athermal metal support frame (Level 3)
- Use laser reflection tool for alignment of arrays of gratings
- X-ray tests of prototypes at ALS, MSFC facility, and PANTER
- Environmental tests to advance TRL

Key Collaborators:

- William Zhang (GSFC)
- Steve O'Dell (MSFC)

Current Funded Period of Performance:

CY 2017 – CY 2018

Recent Accomplishments:

- ✓ Aligned four large ($32{\times}32$ mm^2) gratings to each other, illuminated with two co-aligned SPO X-ray mirror modules obtained predicted (by ray-trace) performance
- ✓ Fabricated several Arcus-sized gratings ($25{\times}26$ mm^2)
- ✓ Integrated laser-based alignment technique with frame bonding station and bonded first Arcus grating facet

Next Milestone:

- Build a more flight-like array of grating facets, align, demonstrate X-ray performance before and after environmental tests (Jun 2019)

Application:

- Flagship X-ray missions
- Explorer X-ray missions
- Laboratory X-ray analysis (materials science, energy research)

$TRL_{In} = 3$ $TRL_{Current} = 4$ $TRL_{Target} = 6$

Next-Generation X-ray Optics: High Angular Resolution, High Throughput, and Low Cost

PI: William W. Zhang / GSFC

Objectives and Key Challenges:

- Develop an X-ray mirror technology that achieves better than Chandra's 0.5" Half-Power Diameter (HPD) angular resolution, while reducing mass and production cost by at least an order of magnitude on a per-unit effective area basis

Significance of Work:

- Enables significant increase in effective collection area for high-performance X-ray telescopes within mass and cost constraints, allowing high science return
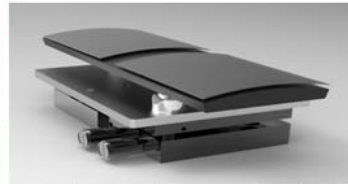
Technology Development Module (TDM) containing one pair of parabolic-hyperbolic mirror segments
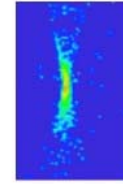
X-ray image with 2.2-arcsec HPD

Approach:

- Precision-polish mono-crystalline silicon to fabricate lightweight mirror substrate
- Develop a coating process to maximize X-ray reflectance without introducing figure distortion
- Develop an alignment process to locate and orient mirror segments to optimize their image
- Develop attachment process to bond mirror segments without introducing alignment and/or figure error

Key Collaborators:

- Kim Allgood, Michael Biskach, Kai-Wing Chan, Michal Hlinka, John Kearney, James Mazzarella, Ryan McClelland, Ai Numata, Raul Riveros, Timo Saha, and Peter Solly (GSFC)

Current Funded Period of Performance:

Oct 2017 – Sept 2019

Recent Accomplishments:

- ✓ Fabricated mono-crystalline silicon mirror substrates that are comparable to or better than Chandra's mirrors in figure quality
- ✓ Validated the meta-shell alignment and bonding approach by aligning, bonding, and X-ray-testing a pair of silicon mirrors

Next Milestones:

- Continue to refine mirror fabrication process to improve figure and roughness quality while reducing production cost and time (Dec 2019)
- Refine mirror-alignment bonding process to fully realize mirror segment potential of 0.5-arcsec HPD (Dec 2020)

Applications:

- Flagship (e.g., Lynx) and Probe-class X-ray missions (e.g., AXIS, TAP, HEX-P and JAXA's FORCE)
- Explorer-type X-ray missions (e.g., STAR-X)
- Medical research and diagnosis

$TRL_{In} = 3$ $TRL_{PI\text{-}Asserted} = 4$ $TRL_{Target} = 5$

Athena WFI / US Contributions

PI: David Burrows/PSU

Objectives and Key Challenges:
1. Develop and test algorithm for on-board detection of transient sources
2. Develop and test algorithm for on-board background rejection
3. Develop improved front-end processing ASIC

Significance of Work:
1. Offers much faster transient source response compared to ground analysis
2. Offers better background rejection than standard pattern-matching algorithms
3. Lower noise and faster readout

Preliminary association of unvetoed events with distance from nearest particle track in raw Chanda/ACIS images. The WFI on-board rejection only eliminates events within about 5 pixels, missing a substantial number of more distant events.

distance from nearest particle track (pixels)

Approach:
1. Developing transient algorithm based on ground analysis software techniques. Will transfer to flight code when details are complete.
2. More sophisticated pattern matching over >> 3x3 pixels.
3. Development of drain readout mode, fixing design errors.

Key Collaborators:
- David Burrows, Abe Falcone, Jamie Kennea, Pragati Pradhan (PSU)
- Mark Bautz, Catherine Grant, Eric Miller (MIT) / Ralph Kraft, Esra Bulbul (SAO)
- Sven Herrmann (Brookhaven Natl. Lab.)

Current Funded Period of Performance:
- 10/16 – 9/19

Recent Accomplishments:
1. Preliminary algorithm development, estimates of transient source rates, presentation of results at SPIE
2. Investigation of associations between events and particle tracks in Chandra, Swift, and XMM data sets
3. Development of V2.2 of VERITAS ASIC

Next Milestones:
- SPM Requirements Review: March 2019

Application:
- Athena Wide Field Imager

$TRL_{In} = 1$ $TRL_{PI-Asserted} = 2$ $TRL_{Target} = 3$

Superconducting Antenna-Coupled Detectors for CMB Polarimetry with the Inflation Probe

PI: James Bock / JPL

Objectives and Key Challenges:

- Advance antenna-coupled superconducting detector technologies for space requirements
- RF-propagation properties
- Beam control and polarized matching
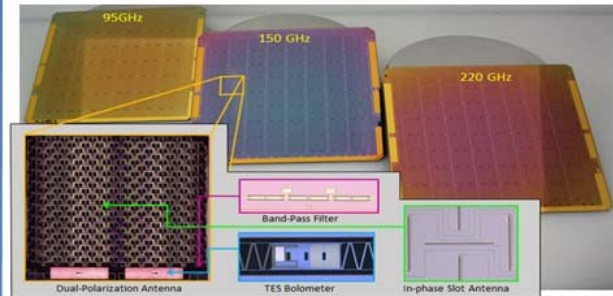- Extended-frequency antennas, detector stability, and cosmic-ray response
- Readout-noise stability, large-format, modular-focal-plane units

Significance of Work:

- Antenna designs for bands required by the Inflation Probe
- Detector sensitivity, stability, and minimized particle susceptibility appropriate for space-borne observations

95GHz   150 GHz   220 GHz

Band-Pass Filter

Dual-Polarization Antenna   TES Bolometer   In-phase Slot Antenna

Arrays of planar antennas for three frequency bands

Approach:

- Planar antennas for entirely lithographed fabrication with no coupling optics
- Detectors provide photon-limited sensitivities in space
- Antennas provide excellent polarization and beam-matching properties
- Modular focal-plane unit for large focal-plane arrays

Key Collaborators:

- Koko Megerian, Hien Nguyen, Roger O'Brient, Anthony Turner, and Alexis Weber (JPL)
- Jon Hunacek, Howard Hui, Sinan Kefeli, and Bryan Steinbach (Caltech)
- Jeff Filippini (UIUC)

Current Funded Period of Performance:

Jan 2018 – Dec 2019

Recent Accomplishments:

- ✓ Assembled and tested prototype 150-mm module
- ✓ Designed and fabricated science-ready 40-GHz sub-array
- ✓ Completed dual-band 30- and 40-GHz antenna design
- ✓ Completed 30-GHz antenna design

Next Milestones:

- Assemble and test 40 GHz sub-array in 150 mm module (8/2018)
- Fabricate dual-band 30 & 40 GHz antennas (9/2018)
- Fabricate 30 GHz antennas (10/2018)

Applications:

- NASA Inflation Probe mission
- Probe-class and international CMB missions
- Technology commonalities with Far-IR and X-ray missions

$TRL_{In} = 3$ $TRL_{Current} = 3$ $TRL_{Target} = 5$

High-Efficiency Feedhorn-Coupled TES-based Detectors for CMB Polarization Measurements

PI: Edward J. Wollack / GSFC

Objectives and Key Challenges:

- Development of focal planes for characterization of CMB polarization with the following detector properties:
  - Background-limited millimeter-wave polarimetric sensor with high coupling efficiency and systematic error control
  - Inherently broadband design, scalable to large-format arrays over multiple frequencies of astrophysical interest

Significance of Work:

- Sub-orbital and space-borne operation of detectors, including:
  - Improved rejection of stray light by detector architecture
  - Improved broadband performance and coupling efficiency
  - Mitigation of space environmental concerns (surface/deep dielectric charging and cosmic rays)
  - Extend architecture to multiple frequencies

90-GHz Sensor Module   Detector Wafer

Approach:

- Multiple fabrication runs to integrate the new technologies into the detector architectures. Specifically, improved:
  - Stray-light mitigation and package thermalization
  - Implementation of air-bridge crossovers and ground-plane contacts for large-bandwidth/low-loss signal routing at higher frequencies

Key Collaborators:

- K. Denis, K. U-Yen, B. Bulcha, and S.H. Moseley (GSFC)
- K. Rostem (GSFC/JHU)
- D. Chuss (Villanova)
- T. Marriage and C. Bennett (JHU)

Current Funded Period of Performance:

Jan 2016 – June 2018
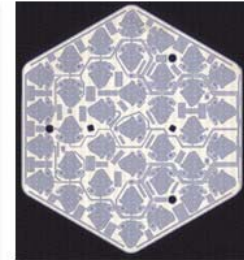
Recent Accomplishments:

- ✓ Air bridge design and fabrication development
- ✓ Device bilayer development and validation
- ✓ CE7 package heat sink / plating validation
- ✓ 150/220-GHz dual-frequency design completed
- ✓ 90-GHz arrays delivered and deployed
- ✓ Test facility commissioning
- ✓ High-frequency package validation
- ✓ Fabrication of 150/220 GHz detector modules

Application:

- CMB Polarimetry, suborbital

$TRL_{In} = 3$ $TRL_{Current} = 3$ $TRL_{Target} = 5$

Program Technology Development Status

X Rays

Cosmic Microwave Background

Directly Deposited Optical-Blocking Filters for Imaging X-ray Detectors

Prepared by: Mark Bautz (PI; MIT Kavli Institute for Astrophysics and Space Research, MKI); S. Kissel, C. Thayer (MKI); K. Ryu and V. Suntharalingam (MIT Lincoln Laboratory); and M. Chodas, S. Megerssa and R Masterson (MIT Space Sciences Laboratory, SSL); with special thanks to the SSL's REXIS team.

Summary

We present a final report on our program to raise the Technology Readiness Level (TRL) of enhanced charge-coupled-device (CCD) detectors capable of meeting the requirements of X-ray grating spectrometers (XGS) and wide-field X-ray imaging instruments for small, medium, and large missions. Because they are made of silicon, all X-ray CCDs require blocking filters to prevent corruption of the X-ray signal by out-of-band, mainly optical and near-infrared (near-IR) radiation. Our primary objective is to demonstrate technology that can replace the fragile, extremely thin, free-standing blocking filter that has been standard practice with a much more robust filter deposited directly on the detector surface.

High-performance, back-illuminated CCDs have flown with free-standing filters (e.g., one of our detectors on Suzaku), and other relatively low-performance CCDs with directly deposited filters have flown (e.g., on the X-ray Multi-mirror Mission-Newton, XMM-Newton Reflection Grating Spectrometer, RGS). At the inception of our program, a high-performance, back-illuminated CCD with a directly deposited filter has not been demonstrated. Our effort will be the first to show such a filter can be deposited on an X-ray CCD that meets the requirements of a variety of contemplated future instruments.

Our principal results are as follows: i) we have demonstrated a process for direct deposition of aluminum optical blocking filters on back-illuminated MIT Lincoln Laboratory CCDs. Filters ranging in thickness from 70 nm to 220 nm exhibit expected bulk visible-band and X-ray transmission properties except in a small number (affecting ≲ 1% of detector area) of isolated detector pixels ("pinholes"), which show higher-than-expected visible-band transmission; ii) these filters produce no measurable degradation in soft-X-ray spectral resolution, demonstrating that direct filter deposition is compatible with the MIT Lincoln Laboratory back-illumination process; iii) we have shown that under sufficiently intense visible and near-IR illumination, out-of-band light can enter the detector through its sidewalls and mounting surfaces, compromising detector performance. This 'sidewall leakage' has been observed, for example, by a previous experiment on the International Space Station during its orbit-day operations. We have developed effective countermeasures for this sidewall leakage; iv) we developed an exceptionally productive collaboration with the Regolith X-ray Imaging Spectrometer (REXIS) team. REXIS is a student instrument now flying on the Origins Spectral Interpretation Resource Identification Security – Regolith Explorer (OSIRIS-REx) mission. REXIS students participated in our filter development program, adopted our technology for their flight instrument, and raised the TRL of this technology beyond our initial goals.

This Strategic Astrophysics Technology (SAT) project, a collaboration between the MKI and MIT Lincoln Laboratory, began July 1, 2012, and ended on June 30, 2018.

Background

The past two decades have brought extraordinary progress in X-ray astronomy, in large measure as a result of unprecedented improvements in X-ray imaging and grating spectroscopy. Beginning with the launch of the Advanced Satellite for Cosmology and Astrophysics (ASCA) in 1993, and continuing to the present, concurrent operation of Chandra, XMM-Newton, and Swift, much of this success has been enabled by X-ray photon-counting CCDs. Advanced CCDs and emerging silicon detectors such as active

pixel sensors (APS) will likely remain essential to X-ray astronomy for decades. In the relatively near term, the extended ROentgen Survey with an Imaging Telescope Array (e-ROSITA) and the X-ray Astronomy Recovery Mission (XARM), will feature silicon CCDs. Instruments using CCDs or APS X-ray detectors are also baselined for both Athena and Lynx, the only two strategic high-energy astrophysics missions now in development or under study by NASA. These instruments address a broad range of important scientific objectives. For example, as noted in the X-ray Mission Concepts Study Report commissioned by NASA's Program Office for the Physics of the Cosmos (PCOS) [1], several high-priority scientific questions identified by the 2010 Decadal Survey, "*New Worlds, New Horizons in Astronomy and Astrophysics*" (NWNH) [2] are best addressed by an XGS, which requires large-format X-ray imaging detectors. Specific science goals for XGS and wide-field imaging instruments are also identified in NASA's Astrophysics Roadmap "*Enduring Quests, Daring Visions*" [3], with examples listed in Table 1. As a result, both an XGS and a silicon-based, high-definition X-ray imager (HDXI) are key instruments for Lynx[1] [4]. For these reasons, technology development for XGS (in 2012) and HDXI (in 2016) has been ranked as a Priority 1 (highest priority) need in recent PCOS Program Annual Technology Reports (PATRs) [5].

Science Question	Measurement	Instrument
How did the first supermassive black holes form?	Find and characterize the seeds of supermassive black holes at very high redshift, and trace their growth	HDXI
How did large-scale structure and baryons co-evolve in the local universe?	Find and characterize the missing baryons in hot galaxy halos and the Warm-Hot Intergalactic Medium (WHIM) via absorption spectroscopy	XGS
	Characterize the diffuse baryons in the first virialized galaxy groups	HDXI
How do black hole feedback processes affect galaxy structure and evolution?	Understand black hole accretion physics and quantify energy and mass content in Active Galactic Nuclei (AGN) outflows	XGS

Table 1. High-priority science drivers for future instruments featuring large-format, imaging X-ray detectors (adapted from the PCOS X-ray Mission Concepts Study Report [1] and the Astrophysics Roadmap [3]). Directly deposited optical blocking filters (OBF) will improve detection efficiency, especially in the soft-X-ray band, while reducing cost and risk of instruments addressing these questions.

Large-format, X-ray imaging detectors are also required for many missions envisaged for the Explorer program, which NWNH deemed "*a crown jewel of NASA space science.*" For example, an Explorer XGS has been proposed for a focused study of the cycles of baryons in and out of galaxies, and their role in galaxy evolution [6]. Other future Explorers will exploit the power of rapid-response X-ray imaging, so clearly demonstrated by Swift, but with much wider fields of view. As noted in [7], a wide-field X-ray imaging instrument on an agile spacecraft can address with unprecedented sensitivity a variety of important science objectives ranging from the nature of the first galaxies to high-energy, time-domain astrophysics. An especially exciting prospect is identification of sources that may be detected by ground-based gravitational-wave observatories later in this decade [8, 9].

Our program aims to raise the TRL of advanced OBF technology required for these instruments. If successful, our effort will improve instrument sensitivity, robustness, and reliability. At the same time, it will reduce mass, complexity, risk, and cost. Our approach is to replace the fragile, free-standing, optical-blocking membrane of current practice with a filter deposited directly on the detector surface.

---

[1] Lynx scientific objectives in particular require maximum detection efficiency in the soft-X-ray band (E < 0.5 keV) and, as explained below, directly deposited optical blocking filter technology offers substantial improvements in this critical instrument capability.

A directly deposited filter can be thinner than a free-standing one, improving instrument sensitivity. Moreover, directly deposited filters do not require the heavy, complex, and expensive vacuum housings used in current instruments, and are of course much more robust than free-standing filters. The key challenge for our program is to demonstrate that blocking filters can be applied directly to the sensitive entrance surfaces of modern CCD detectors without compromising spectroscopic resolution.

To minimize cost, our program uses existing stocks of engineering-grade detectors produced for past programs at MIT Lincoln Laboratory. We apply so-called 'back-illumination' (BI) processing to these detectors, and then use coating facilities at Lincoln Lab to apply blocking filters. X-ray and optical performance-testing is then conducted at MKI. We have also joined forces with REXIS, an MIT student instrument for NASA's OSIRIS-REx mission, to incorporate directly deposited blocking-filter technology into a flight program.

Objectives and Milestones

Silicon X-ray imaging detectors require blocking filters to prevent ambient visible and ultraviolet (UV) background light from adding noise and degrading X-ray spectral resolution. As noted above, most such detectors flown to date have used fragile, free-standing filters comprised of thin plastic substrates coated with aluminum. Free-standing filters usually must be protected from ground-handling and launch acoustic loads using heavy vacuum enclosures equipped with complex door mechanisms. This project aims to show that adequate OBFs can be deposited directly on a detector, eliminating the need for fragile, freestanding filters. To the extent that they eliminate plastic films, such filters could also improve soft-X-ray (E < 1 keV) detection efficiency.

A key challenge in this project is to demonstrate that directly deposited OBFs provide the requisite optical blocking performance without compromising the spectral resolution of the detectors in the soft-X-ray band. The latter depends critically on the electric fields present just inside the entrance surface of the detector, and these fields in turn require precisely controlled implant-density profiles. Our aim is to deposit blocking filters in such a way that the surface fields are unaffected by the deposition process or the filter itself. A secondary objective is to demonstrate that such filters are sufficiently robust to survive the repeated thermal cycling any such detector is likely to experience.

Originally, we planned to complete the following four tasks:

Task 1: Select and thin existing CCID41 wafers and apply backside treatment

The target detectors for this project (Lincoln Laboratory model CCID41, now in use in Suzaku) were stored in wafer form as front-illuminated (FI) devices (typically four to a wafer). We identify functional devices using wafer-probe equipment. We then subject selected wafers to a custom, backside treatment process, involving wafer thinning and molecular-beam-epitaxy (MBE) passivation, which has already been shown to provide good X-ray results. Selected BI devices are packaged (removed from the wafer and installed in suitable test packages) for subsequent test at MKI.

Task 2: Establish baseline X-ray performance

We use established X-ray characterization facilities and procedures at MKI to verify suitable X-ray performance of the BI (but uncoated) devices.

Task 3: Apply filters and characterize filter-equipped devices

We deposit aluminum blocking layers using established thin-film deposition facilities at MIT Lincoln Laboratory, and then package and test the filter-equipped devices. Filters are applied at the wafer level, with control areas masked to allow direct comparison of filtered and unfiltered areas of each device. We carry out three cycles of filter deposition and test (one wafer per cycle), applying a relatively thick filter in the first cycle, and then continuing, after successful test, to progressively

thinner filters. In so doing, we span the range of filter thicknesses required by future instruments. All filters are capped with a 10-nm Al_2O_3 layer to improve robustness and provide UV blocking. Both optical rejection and X-ray spectral resolution are measured in the characterization protocol.

Task 4: Test robustness and stability

To verify coating temporal stability and robustness to the repeated thermal cycling experienced by CCD detectors during instrument development and test, we perform thermal cycling and long-term (6-8 months) stability measurements.

Soon after program start, we decided to alter the sequence of the program for two reasons. First, we discovered that a number of BI devices were already available at MIT Lincoln. To make best use of these, we needed to develop a filter deposition process that would accommodate individual chips as well as full wafers. Second, we learned that the MIT team developing REXIS wished to fly X-ray CCDs with directly deposited blocking filters. We decided to collaborate with REXIS because by doing so we gain the opportunity to demonstrate much higher TRL for our process than we could achieve in our original program. Indeed, as discussed below, through this collaboration, and with the support of the PCOS Program Office, we have defined a clear path to demonstrating that this technology has achieved TRL 6.

Major milestones and our progress in achieving them are summarized in Table 2. We describe our progress in more detail in the following section.

Milestone at Completion of:	Success Criteria	Status as of June 2018
1. BI processing	Wafer-probe testing of BI wafers shows: ≥3 wafers with functional devices ≥ 10 functional devices total	• Twelve FI wafers processed, yielding 33 devices with at least some functionality, of which eight are allocated to REXIS • Ten other functional BI devices identified as single chips
2. X-ray test of baseline BI device	X-ray performance demonstrated per protocol specified in proposal	• Complete; X-ray performance supports program objectives
3. 1st device with thickest directly deposited filter	Packaged device delivered to MKI	• Complete (220-nm-Al OBF)
4. X-ray and optical testing of device with thickest filter	X-ray and optical tests done per protocol specified in proposal	• Complete; three devices with 220-nm OBF characterized
5. X-ray and optical testing of device with thinnest filter	X-ray and optical tests done per protocol specified in proposal	• Complete; one device with 100-nm OBF and two with 70-nm OBF characterized
6. Long-term stability test	X-ray and optical tests done per protocol specified in proposal	• Eight-month test completed
7. Thermal cycle test	X-ray and optical tests done per protocol specified in proposal	• Thermal vacuum (TVAC) X-ray testing of REXIS flight unit completed; X-ray performance of OBF unaffected; optical performance of OBF not measured • Thermal cycle (10 cycles to -70°C) and vibration (per GEVS, 14.1 g RMS) testing completed on REXIS flight spare detector. No measurable change in optical performance of OBF. See Section 6.

***Table 2.** Project milestones and status (GEVS, General Environmental Verification Standard).*

Progress and Accomplishments

We have developed an OBF deposition process and thoroughly characterized X-ray and optical performance of BI CCDs with OBFs of a range of thicknesses (220-, 100-, and 70-nm Al) as specified in Milestones 1-7 in Table 2. Details of our process and principal results have been presented in the literature [10, 11] and may be summarized as follows.

1. We demonstrated that it is feasible to deposit effective aluminum OBFs directly on high-performance BI CCDs with, at most, modest effect on X-ray spectral resolution.
2. The measured X-ray transmission of these OBFs is consistent with theoretical expectations.
3. The measured visible/near-IR transmission of these OBFs is consistent with the expected level of attenuation over most of the filter area, but higher than expected transmission is observed in a small fraction of pixels. The pixels exhibiting these so-called "pinholes" can have sensitivity to visible light that is 10× to 1000× theoretical expectations. We find evidence that these pinholes are produced by irregularities on the detector surface. These irregularities, each extending over at most a few hundredths of a square micron of detector surface, seem to cause small breaks in the aluminum blocking layer. The irregularities may be caused either by intrinsic roughness of the CCD surface or by sub-micron particulate contamination. The fraction of pixels exhibiting pinholes can be reduced to 1% or less by (i) minimizing the density of sub-micron particles on the detector surface before aluminization, and (ii) suitably orienting the detectors relative to the aluminum source during OBF deposition.
4. For very demanding optical-blocking applications, requiring visible/IR-band attenuation factors greater than 10^6, we found that it may be necessary to take additional steps to prevent light from entering the detector through its sidewalls and through the adhesive layer that affixes the detector to its package. We developed methods for doing this for the REXIS instrument.
5. Results from our long-term stability tests show no change in visible/IR blocking performance of a directly deposited OBF after eight months of storage in a laboratory environment.
6. In collaboration with the OSIRIS-REx/REXIS instrument team, and with the support of the PCOS Program Office, we have extended our project goals from the originally proposed thermal testing (Milestone 7 in Table 2 above) to include a demonstration that our OBF technology achieved TRL 6. Although REXIS is now aboard OSIRIS-REx and cruising toward its asteroid rendezvous, the flight instrument's OBF will not be tested until early 2019, when the REXIS door is to be opened. Before launch, the flight instrument completed environmental testing with successful X-ray performance, but it was not possible to verify the post-test visible-band performance of its OBFs. Therefore, in an effort to demonstrate TRL 6, we engaged MIT graduate and undergraduate students to plan, develop facilities for, and execute an environmental test program with the REXIS flight spare detector assembly mount (DAM). This plan was presented to and approved by PCOS technology managers as acceptable for a TRL-6 demonstration. As detailed below, vibration and thermal cycling tests were completed, with no measurable change optical performance of the OBF. For various reasons unrelated to the OBFs, and described in detail below, it proved necessary to modify the approved TRL-6 demonstration plan during execution. At this writing, the current TRL of this technology has not been formally determined by the PCOS program office. It is certain, however, that this effort has provided invaluable educational experience for young researchers and engineers at MIT.

We discuss each of these results in turn.

1. Soft-X-ray spectral resolution with directly deposited blocking filters

Soft X rays (with energies below 1 keV) are photo-electrically absorbed within ~1 µm of the entrance surface of a silicon detector, so good X-ray spectral resolution requires efficient collection of photoelectrons generated in this region. Precise doping of the entrance ('back') surface of the detector is necessary to produce the internal electric fields required to achieve this. We aimed to

determine whether a metal OBF layer deposited directly on this surface would affect the spectral resolution of an X-ray CCD detector. Figure 1 shows a broadband, multi-line pulse-height spectrum obtained from a BI CCD with a directly deposited, 220-nm-thick OBF. The spectrum shows that such a detector (similar to those installed on REXIS) can readily resolve characteristic lines of elements ranging from oxygen to iron.
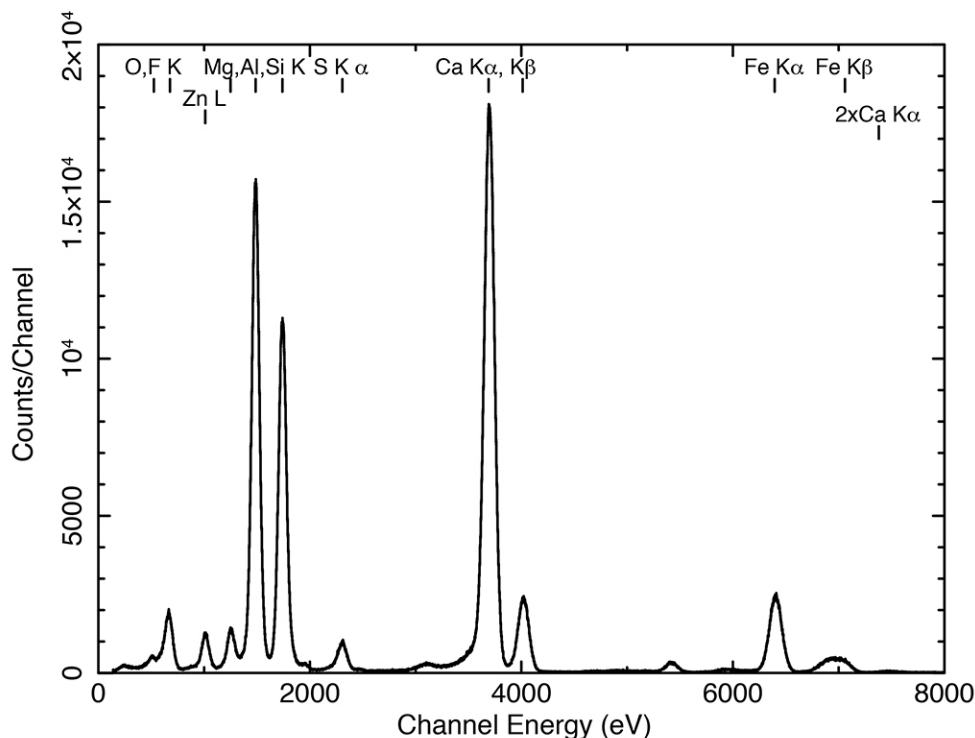
Fig. 1. Broadband, composite pulse-height spectrum from a BI CCD equipped with a directly deposited 220-nm-thick aluminum OBF [device 53-1-7-1]. Characteristic lines of elements ranging from oxygen to iron are readily resolved.

How does a directly deposited OBF affect CCD spectral resolution at very soft (E < 1 keV) energies? Figure 2 addresses this question by comparing pulse-height spectra from three representative devices. The back surfaces of all of these detectors were treated with MIT Lincoln Laboratory's MBE process. One device has no OBF, and the other two have directly deposited aluminum OBFs with thicknesses of 70 nm and 220 nm, respectively. Identical exposure times to the same radioactive X-ray source were used to obtain the spectra. The source produces characteristic lines of C-K, V-L, O-K, and F-K, with energies ranging from 277 eV to 677 eV. As expected, X-ray absorption in the filters reduces the amplitudes of the lower-energy peaks. Figure 3 compares peak widths (full-width at half-maximum, or FWHM) measured for different spatial regions, called quadrants, on each device. Each device quadrant has a dedicated on-chip amplifier. These are engineering-grade devices, so the noise levels, and thus the expected peak widths, differ from quadrant to quadrant. The points in Fig. 3 for the unfiltered ('No-OBF') and '220-nm-OBF' cases show the mean, minimum, and maximum of three device quadrants in each configuration. The 70-nm-OBF points show results for a single quadrant. The means of the unfiltered and 220-nm configurations are closer than the quadrant-to-quadrant scatter within each configuration, and the single-quadrant measurements available from the device with the 70-nm OBF are marginally better than any of the quadrants on the other two devices at all three energies. Thus, we find no evidence that the directly deposited OBF compromises the soft-X-ray FWHM of these detectors.
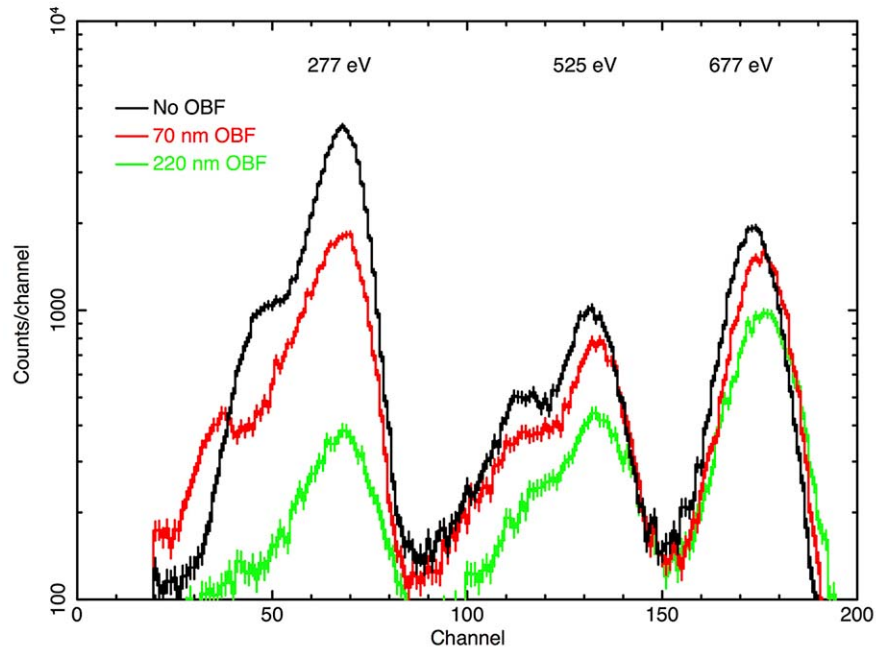
Fig. 2. *Soft-X-ray response of a device with no OBF (black) and with 70-nm- and 200-nm-thick directly deposited aluminum filters (red and green, respectively). The filters have very little effect on spectral resolution.*
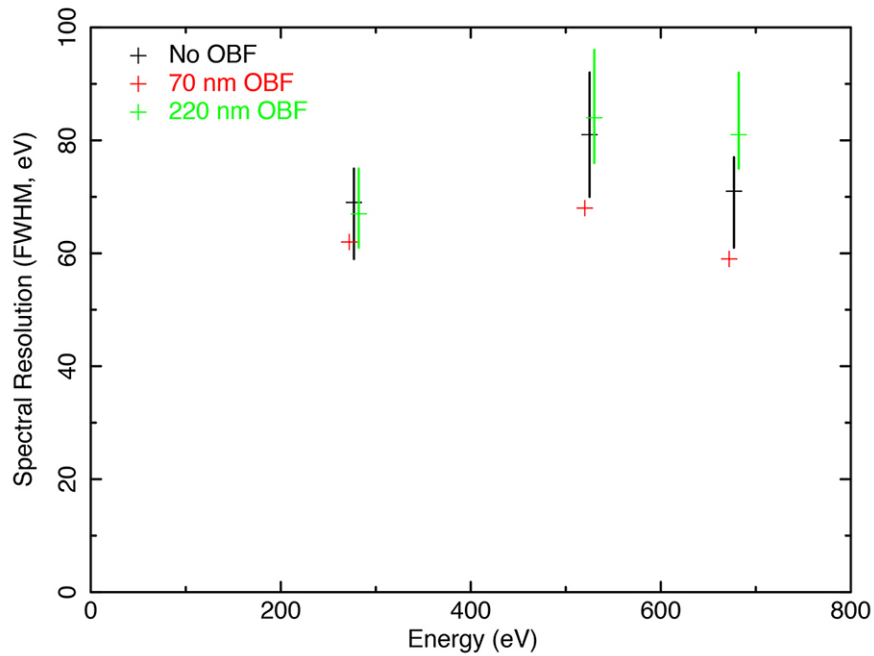
Fig. 3. *Spectral resolution (FWHM) of devices with no OBF (black), 70-nm-aluminum OBF (red), and 220-nm-aluminum OBF (green). "No-OBF" and "220-nm-OBF" points show mean, minimum, and maximum FWHM measured for three independent CCD quadrants in each configuration; 70-nm points show measurements for a single CCD quadrant. The OBFs have no clear effect on spectral resolution. Energy coordinates have been displaced slightly to show the ranges in FWHM clearly.*

Returning to Fig. 2, it is clear that the shape of the spectral redistribution function of all devices degrades to some extent at the lowest energies. At 677 eV, the response function is quite symmetrical

18

for all three devices. Near 500 eV, the blend of vanadium-L and oxygen-K lines produced by the source is evident, and this blend makes it difficult to assess the shape of the response function there. The responses of all three devices at 277 eV show a clear low-energy shoulder. The ratio of main-peak to shoulder amplitudes (about 5:1) is about the same for all devices, suggesting that the shoulder is due neither to the source spectrum nor to the presence of the OBF. We hypothesize the tail is a consequence of the relatively thick (20 nm) p^+ MBE layer applied in fabricating these devices. About 15% of the incident photons at this energy will be absorbed in the MBE layer. A thinner MBE layer might thus be expected to provide better charge collection for very-soft-X-ray photons. We find no evidence that the shape of the response function is affected by the presence of the OBF.

2. X-ray transmission of directly deposited OBFs

Measured X-ray transmission of a 70-nm-thick OBF is compared to expectations in Fig. 4, with generally good agreement. The data were obtained from a device (53-1-4-2) on which only part of the detector was covered by the OBF. Both covered and uncovered regions were exposed to a multi-line source like the one used to produce the spectra in Fig. 1, and transmission was determined from the line fluxes measured in the two regions. The red circles show measurements obtained by fitting Gaussian profiles to the data. Green crosses show fluxes obtained by summing over a spectral region within ± 3 standard deviations of line centers. The two methods agree reasonably well, except at the very lowest energy measured (183 eV) where the line profiles are distinctly non-Gaussian. Similarly, good agreement between measurements and expectations is obtained with 200-nm OBFs (see [10] for details).
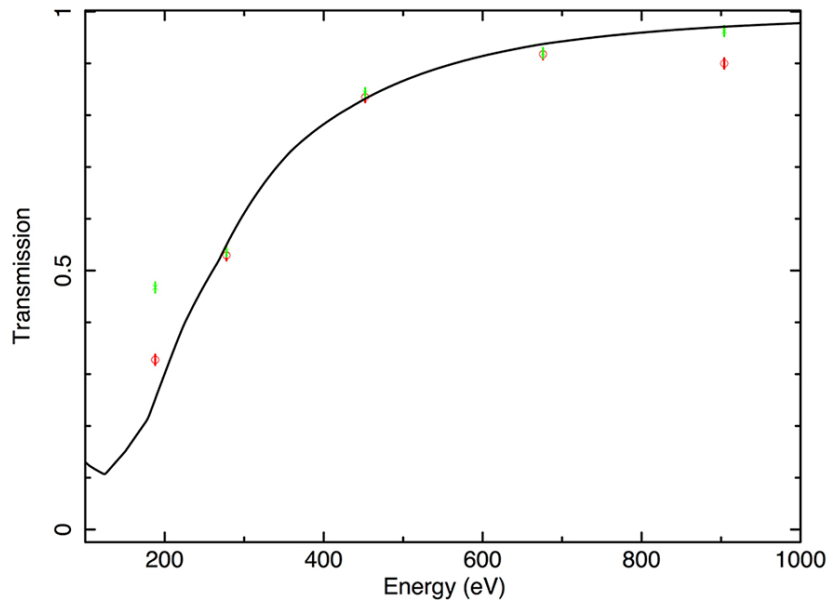
Fig. 4. *Measured (points) and modeled (curve) X-ray transmission of 70-nm-thick aluminum OBF. Red and green points obtained with different X-ray measurement methods discussed in the text.*

3. Visible/near-IR transmission of directly deposited OBFs

Figure 5 shows the measured visible-band quantum efficiency (QE) of a device with a directly deposited blocking filter with a nominal thickness of 70 nm. The measurements agree reasonably well with a simple model of an aluminum layer over a thick silicon substrate. The aluminum thickness in the model has been adjusted to 63 nm to fit the data. The model assumes perfect internal CCD QE, which is certainly an overestimate redward of 600 nm, as the (thinned) detector's sensitive volume (depletion region) is nominally 45 microns thick. A more sophisticated model, incorporating an accurate treatment of the internal detector efficiency, is clearly required to represent the data in the

near-IR spectral band. The present results may indicate the OBF is somewhat more transparent in this spectral band than the simple model predicts.
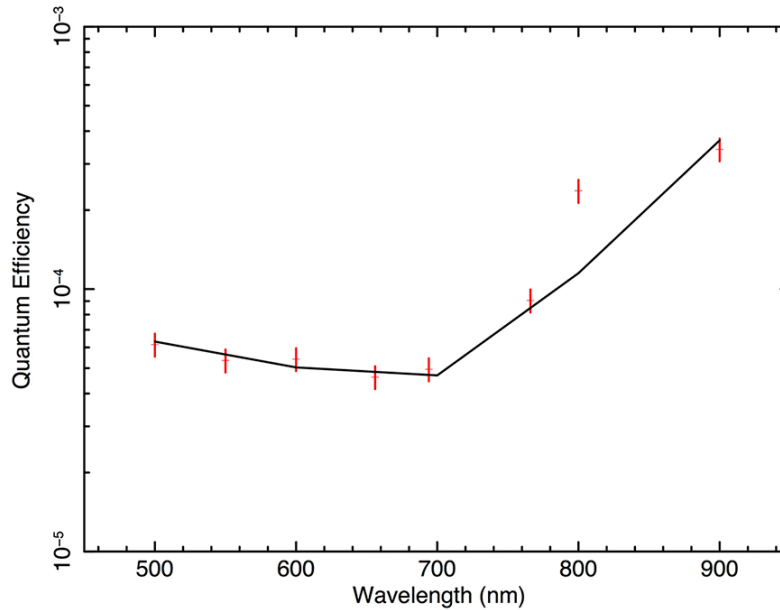
Fig. 5. Visible/near-IR QE of a CCD with a directly deposited blocking filter. Nominal filter thickness is 70 nm. The points are measured values; the line is a simple model of a 63-nm-thick OBF. Note: data from device 53-1-4-2.

Visible-band, flat-field exposures with both 220-nm-thick and 70-nm-thick OBFs show "pinhole-like" regions of relatively high transmission, as shown in Fig. 6. The image on the left shows pinholes in a 220-nm-thick OBF. The device was exposed to a fluence of 1.3×10^6 photons/pixel at 800 nm. A histogram of the 440,000 pixel amplitudes in the image is shown in the right panel. The theoretically expected transmission of this OBF at this wavelength is less than 10^{-9}, so if the OBF was perfect, all pixels would have zero amplitude, modulo the readout noise with root-mean-square (rms) width of a few electrons. The histogram shows that 99% of pixels are in fact consistent with zero amplitude, and about 1% of pixels are affected by pinholes with transmission ranging from about 10^{-6} to as high as 5×10^{-4}.

20
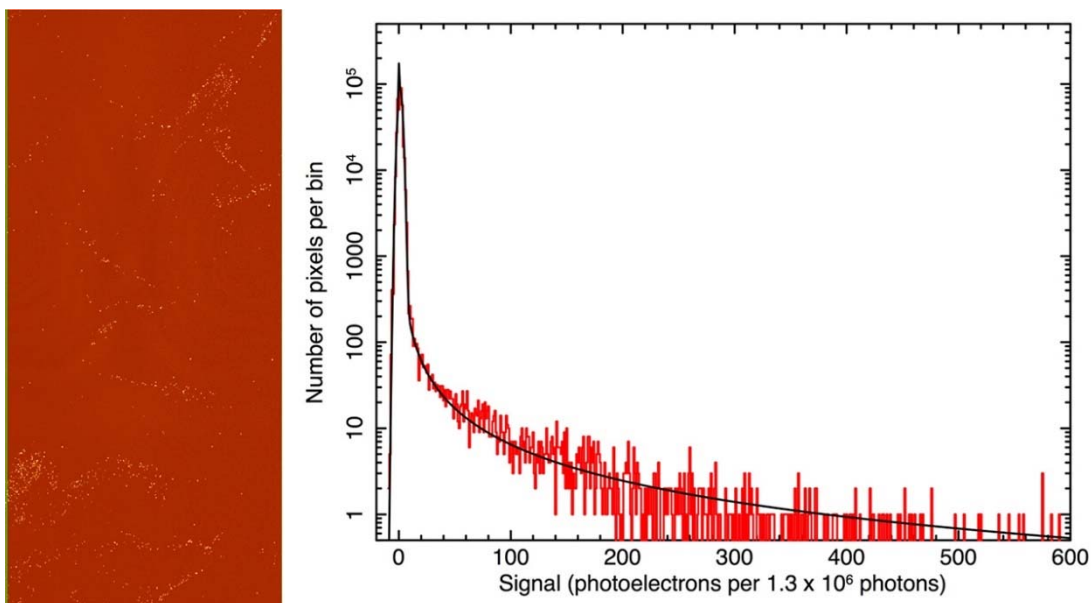
Fig. 6. Left: *Image obtained using CCD with a 220-nm-thick OBF illuminated with 1.3×10^6 photons/pixel of 800-nm light. Pinholes (white spots) are evident.* Right: *Histogram of amplitudes of the 440,000 pixels in the image on the left. While 99% of pixels are in the peak, consistent with zero amplitude, about 1% show transmission greater than 10^{-6}.*

Wafer-level measurements at MIT Lincoln Laboratory of other devices equipped with 220-nm-thick OBFs show an extinction ratio of 10^{13} at 633 nm, except in the small fraction of pixels affected by pinholes [11]. The inferred absorption coefficient is 1.3×10^6 cm^{-1}, close to the expected value of 1.5×10^6 cm^{-1} [12], confirming the high quality of the OBF film as a whole.

As discussed in detail in [10] and [11], we believe the pinholes are caused by surface irregularities present on the detector surface before the OBF is deposited. Several lines of evidence support this explanation. First, test coatings on quartz substrates do not show pinholes. Second, as shown in Fig. 7, scanning electron micrographs of deposited OBFs show texture with sizes (< 100 nm) and spatial density consistent with the observed number and transmission of pinholes. Third, the number of pinholes is dramatically reduced if an optically transparent, 1-μm-thick layer of photoresist is deposited on the detector surface before the aluminum OBF layer is deposited. Although such an interlayer is opaque to soft X rays and so could not be used on an X-ray sensor, this result does suggest there are no fundamental limitations to fabrication of a pinhole-free, directly deposited OBF.
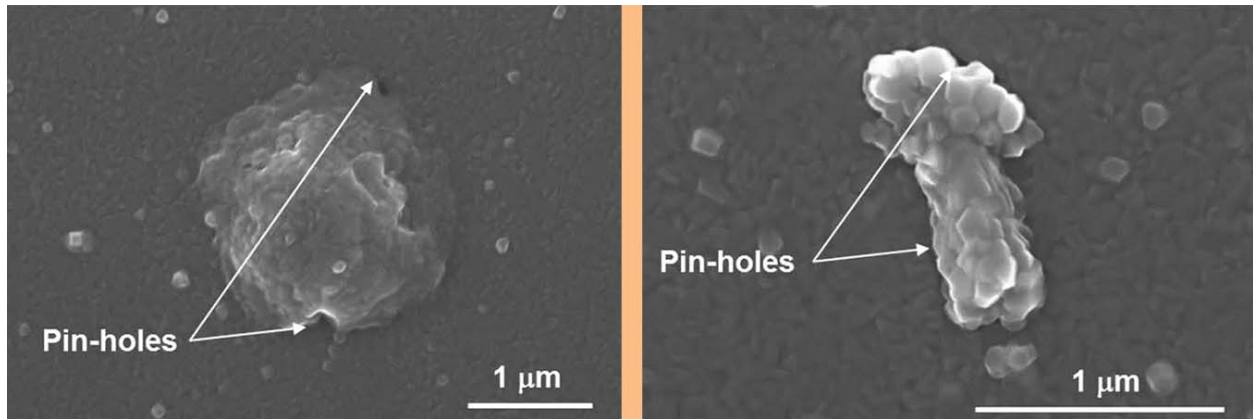
Fig. 7. *Scanning electron micrograph images of an OBF directly deposited on the surface of a CCD.*

Indeed, our success in reducing the pinhole fraction to less than 1%[2] for REXIS OBFs is further evidence in favor of this explanation for the origin of pinholes. Two measures in particular have proven effective. First, the interior surfaces of the coating chamber were aluminized after cleaning, to minimize particulate contamination originating in the chamber walls. Second, the deposition geometry was changed so that the incident aluminum atoms approach the detector surface at about 45° to the surface normal. The detector rotates about its surface normal during this process. This 'angled-deposition' allows the aluminum to cover the vertical sides as well as the tops of residual surface irregularities, and thus reduces the number of pinholes.

4. Detector sidewall and bond-line leakage paths

The thickest OBF layers we tested, with 220 nm of aluminum, have a theoretical attenuation well in excess of a factor of 10^9. The REXIS instrument, which will map fluorescent X-ray emission from the

---

[2] Specifically, the mean fraction of pixels with optical density less than 7 (i.e., with pinholes) in 220-nm-thick OBFs in the 12 best REXIS flight devices is 0.76%; the rms pinhole fraction in this sample is 0.45%. An anomalous 13th device showed a pinhole fraction of 4.1%. See [11] for details.

sunlit surface of asteroid RQ36, requires substantial optical blocking and is equipped with filters of this thickness. Our evaluation of directly deposited OBFs of this thickness revealed that to achieve very large attenuation (greater than a factor of $\sim 10^6$), one must block not only the light entering the entrance surface of the detector, but also light entering its thin side walls and even its mounting surface.

The effect and location of these leakage paths are illustrated in Fig. 8. The left panel shows a grayscale image obtained by illuminating a CCD with a 220-nm-thick OBF. The white areas around the edges of the device have an attenuation factor of 10^7 or less. The right panel shows two leakage paths responsible for this effect. Light can enter the photosensitive regions of the device through its thin (45-µm-thick) sidewalls. Light can also penetrate the thin ($\sim$10-µm-thick) epoxy bond-line that attaches the CCD to the (photo-insensitive) silicon support wafer. A third leakage path, similar to the second but not shown in the figure, runs through a second, thicker epoxy bond-line that attaches the support wafer to the detector package, through the support wafer and into the detector from below. This third leakage path transmits mainly near-IR radiation to which the support wafer is relatively transparent.
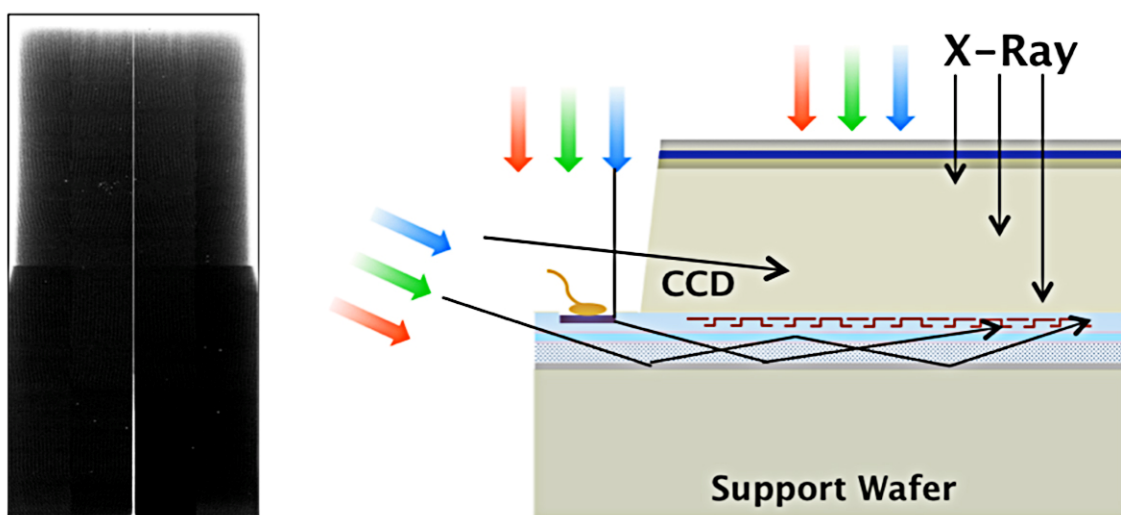
Fig. 8. *Edge and 'bond-line' leakage.* Left: *A CCID-41 with a directly deposited blocking filter under flood illumination. White areas around edges have attenuation* $< 10^7$*, and are due to light entering the sides and back of the detector.* Right: *Illustration of two leakage paths.*

Leakage through the two paths shown in Fig. 8 was reduced to levels acceptable to REXIS by depositing an additional 100 nm of aluminum using the angled-deposition geometry described in the previous section. This coating covers the detector sidewalls and the bond-line between the detector and the support wafer. In addition, the REXIS team qualified two effective countermeasures against bond-line leakage at the bottom of the support wafer. One method was to coat the bottom of the support wafer with black paint, using a suitable adhesion promoter. The other method was to deposit a 300-nm-thick aluminum layer on the bottom surface of the support wafer. REXIS has adopted the latter approach because it permits a flatter surface coating that can be applied more quickly.

5. Long-term stability of directly deposited OBFs

The final task in our original program was to evaluate the long-term stability of directly deposited OBFs. We began this process in September 2014 with a baseline evaluation of device 53-1-17-2, which is equipped with a 100-nm-thick OBF. We monitored this device over a period of eight months and did not detect any significant change in OBF performance. In particular, Fig. 9 compares pinhole maps obtained for this device before and after eight months of laboratory storage. The images have been scaled to correct for light-source-intensity differences so that the mean of the amplitudes of a set of

randomly selected pinhole pixels is the same in both images. To date, we find no evidence for change over time in the optical blocking properties of this OBF.
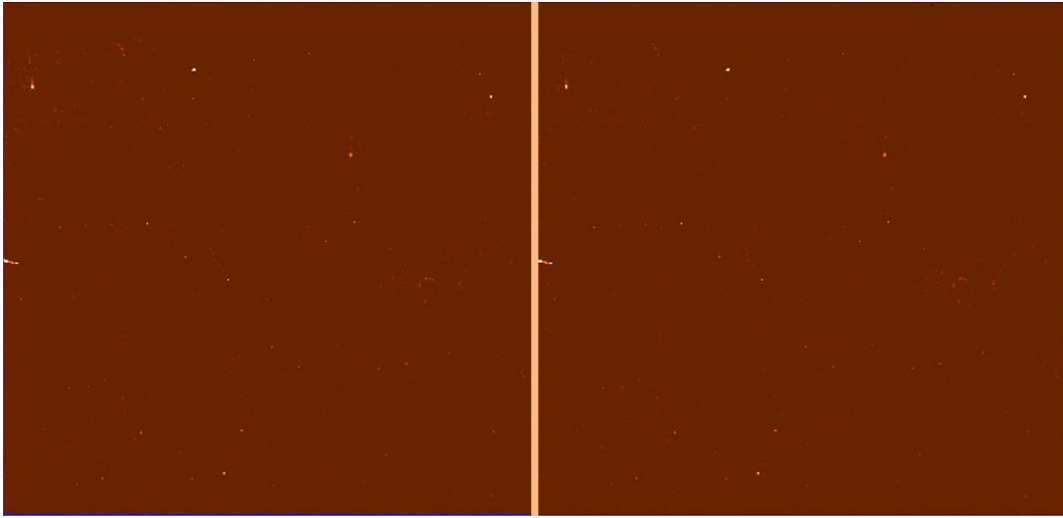
Fig. 9. Pinhole maps of a randomly chosen 400×400-pixel section of CCD 53-1-17-2 equipped with a 100-nm-thick directly deposited aluminum OBF, obtained in September 2014 (left) and June 2015 (right). These images demonstrate the stability of the OBF over an eight-month period of laboratory storage.

6. Toward TRL-6 demonstration with the REXIS flight spare DAM

Graduate and undergraduate students in MIT's Department of Aeronautics and Astronautics on the REXIS team, supervised by the REXIS project manager, developed a plan to demonstrate that our OBF technology is at TRL 6. The students presented this plan to PCOS Program Office technology managers who judged it suitable, after some modification, for this purpose.

The principal goal of the demonstration was to characterize the effect of environmental stresses on the performance of directly deposited OBFs in the REXIS flight spare DAM (Fig. 10), with particular emphasis on environmental effects on the number and characteristics of pinholes in the OBFs. Given our finding that these pinholes are caused by surface irregularities on the detector surface, the team decided that thermal cycling and vibration tests are relevant, but that electromagnetic environments are not. The relevance of atomic oxygen was discussed with PCOS technologists, and it was concluded that for sufficiently high-altitude ("interplanetary") mission trajectories like that of OSIRIS-REx, atomic oxygen is not relevant. The effects of atomic oxygen on directly deposited OBFs may be relevant for low-Earth-orbit missions.
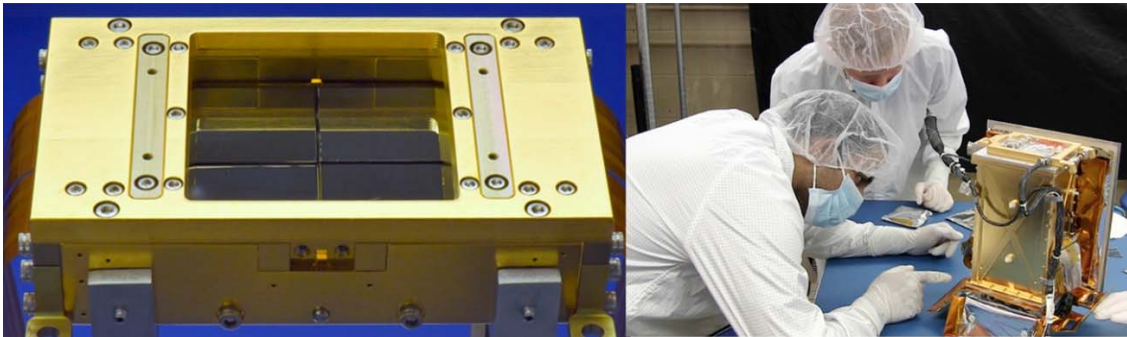
Fig. 10. Left: *The REXIS DAM features four MIT/Lincoln CCDs, each with a directly deposited OBF. The total active area of the detectors is about 5 cm × 5 cm.* Right: *Students preparing the REXIS instrument for environmental testing. A student project was formulated and executed with the goal of using the REXIS engineering-model hardware to*

demonstrate that directly deposited OBF technology is at TRL 6. Images courtesy of MIT Lincoln Laboratory and MIT Space Sciences Laboratory.

A group of students and young researchers at MIT set out to execute this plan during the final reporting period of our program. A comprehensive summary of the plan and the test results has been prepared by the test team and attached as an appendix to this report. Although it proved necessary to modify the test plan during execution, the team reports that after exposure to REXIS-level vibration and thermal cycling environments, they find no measurable change in the optical blocking performance of REXIS OBFs.

Several challenges encountered during the test program required deviations from the approved TRL-6 demonstration plan. For completeness, these are summarized here.

Stability/reproducibility*:* The test success criteria are based on the number of observed pinholes in the OBFs. Pinholes are identified as pixels producing signal above a prescribed threshold under a prescribed illumination level. The success criteria in the approved plan placed stringent limits on changes in the observed pinhole count. In practice, pre-environmental tests showed small test-to-test variations in the observed pinhole count under nominally identical test conditions. These variations are probably the result of variations in the illumination level and/or temperature of the focal plane. The latter can cause changes in the dark current in so-called hot pixels that can be mistaken for defects in the OBF.

To account for this phenomenon, the team made multiple measurements before and after exposure to each environment to determine the reproducibility of the pinhole count measurement. The test success criteria were modified to require that any observed change in pinhole count be within the expected reproducibility of the measurements. These modified success criteria were in all cases sufficiently stringent that post-environmental performance easily met REXIS science requirements.

Thermal cycling: The approved TRL-6 test plan called for eight thermal cycles between -50°C and -100°C with a dwell time of 30 minutes. A number of anomalies during the test program, unrelated to the OBFs and described in the appendix, severely curtailed the time available for testing. As a result, the accumulated thermal cycling exposure of the OBFs over the test program was adopted for the thermal cycling test. This consisted of eight cycles between room temperature and -70°C and two additional cycles between room temperature and -90°C.

Summary

We have demonstrated that directly deposited aluminum OBFs are compatible with high-performance BI X-ray CCD detectors. The techniques we developed may be used to deposit OBFs directly on other BI silicon X-ray detectors as well. We have developed deposition methods that minimize the number of pinholes in such filters, and demonstrated high-quality filters ranging from 70 nm to 220 nm in thickness. We have also developed effective countermeasures against light leakage through the sidewalls and packages of such detectors, having found these to be necessary for applications requiring filters with optical density greater than ~6. We have published our findings in the refereed literature [11].

The OBF technology we developed has been incorporated in the flight model of the REXIS instrument on OSIRIS-REx. In collaboration with the REXIS team and the PCOS Program Office, we have extended our program goals to include a demonstration that directly deposited OBFs have achieved TRL 6. MIT engineering students and other young researchers have completed an extensive test program that has made significant progress toward this objective.

References

[1]   X-ray Community Science Team, X-ray Science Support Team, and X-ray Engineering Support Team, "*X-ray Mission Concepts Study Report*" (2012)

[2]   National Academy of Science, Board on Physics and Astronomy, "*New Worlds, New Horizons in Astronomy and Astrophysics*" (2010)

[3]   NASA Astrophysics Roadmap Team, C. Kouveliutou, Chair, "*Enduring Quests, Daring Visions: NASA Astrophysics in the Next Three Decades*" (2013)

[4]   M. Weisskopf et al., "*Beyond Chandra – The X-ray Surveyor*," Proc. SPIE 1505.00814 (2015)

[5]   NASA Physics of the Cosmos Program Office, "*NASA Physics of the Cosmos Program Annual Technology Report*" (2012, 2016)

[6]   R. Smith et al., "*Arcus: an ISS-attached high-resolution X-ray grating spectrometer*," Proc. SPIE **9144**, id. 9144Y, (2014)

[7]   N. Gehrels, S. Barthelmy, and J. Cannizzo, "*Time-Domain Astronomy with Swift, Fermi and Lobster*," Proc. IAU, **285**, 41-46, (2012)

[8]   Laser Interferometer Gravitational-wave Observatory (LIGO) Scientific Collaboration, "*Predictions for the rates of compact binary coalescences observable by ground-based gravitational-wave detectors*," Classical and Quantum Gravity, **27**, 173001, (2010)

[9]   B.D. Metzger and E. Berger, "*What is the Most Promising Electromagnetic Counterpart of a Neutron Star Binary Merger?*" Astrophysical Journal, **746**, 48, (2012)

[10] K. Ryu et al., "*Development of CCDs for REXIS on OSIRIS-REx*," Proc. SPIE **9144**, 91444O-1 (2014)

[11] K. Ryu, M. Bautz, S. Kissel, P. O'Brien, and V. Suntharalingam, "*Directly Deposited Optical-Blocking Filters for Single-Photon X-ray Imaging Spectroscopy*," JATIS (2017, in press)

[12] A. Rakic, A. Djurvic, J. Elazar, and M. Majewski, "*Optical Properties of Metallic Films for Vertical-Cavity Optoelectronic Devices*," Applied Optics **37**, 5271 (1998)

For additional information, contact Mark Bautz: *mwb@space.mit.edu*

Appendix: Environmental Testing of the REXIS Optical Blocking Filter

Prepared by Carolyn Thayer and Solan Megerssa on behalf of the REXIS Team

Summary

The REgolith X-ray Imaging Spectrometer (REXIS) [1] is the student collaboration instrument aboard NASA's OSIRIS-REx asteroid sample return mission. OSIRIS-REx is a NASA New Frontiers mission that will travel to the near-Earth asteroid Bennu and return a sample of the asteroid's regolith. REXIS features charge-coupled device (CCD) X-ray detectors equipped with directly deposited optical blocking filters (OBFs). The OBFs prevent reflected, visible-band sunlight from the asteroid from affecting the quality of REXIS X-ray spectroscopy.

This document describes results of environmental (vibration and thermal cycling) tests of REXIS OBFs. OBF performance was characterized by two figures of merit derived from the number of OBF 'pinholes.' Although the test protocol was complicated by hardware failures unrelated to the OBFs, testing showed no measurable degradation of the OBF performance as a result of vibration and thermal cycling.

Introduction

REXIS is a coded-aperture X-ray spectrometer that measures soft X rays in the range 0.5 - 7.5 keV to map the elemental composition of Bennu in order to categorize it among the major meteorite groups and to contribute to the sample site selection. The imaging array is a two-by-two array of silicon wafer CCDs. Figure 1 shows the instrument fully assembled.

Fig. 1. *Fully Assembled REXIS.*

REXIS will measure the fluoresced X rays from Bennu caused by solar X rays. However, the visible spectrum of solar radiation reflecting off the asteroid is a source of noise for the X-ray imaging operation. The presence of visible photons necessitates the use of an OBF to reduce the intensity of visible light on the CCDs. The OBF is a 220-nm thick aluminum film directly deposited onto the CCD wafers.

Initial testing of the filter by Ryu et al. [2] showed visible-light leak through the OBF. To characterize the light-blocking properties of the OBF, Ryu flooded the detectors with uniform light at a fluence of $\sim 10^{15}$ photons cm^{-2} (the expected optical loading per 4-sec REXIS frame during operation). About 5%

of the pixels detected visible light above the noise floor, indicating that visible light was penetrating the OBF. The results are shown in Fig. 2a. Further testing of the optical performance of the OBF showed no significant departures from its expected X-ray performance based on the literature. For example, the absorption coefficient of the film, a measure of how easily light passes through the film, was estimated to be 1.3×10^6 cm^{-1}, which is close to the published value of 1.5×10^6 cm^{-1} [3]. This result indicates that the light leak was a physical phenomenon. It was determined that microscopic pinholes in the surface of the film likely caused by roughness in the silicon substrate on which the OBF is deposited were letting extra light through. Figure 2b shows a Scanning Electron Microscope (SEM) image of the pinholes.

Fig. 2a. *White areas show where light is visible above the noise floor on the flight CCDs pre-environmental testing.*
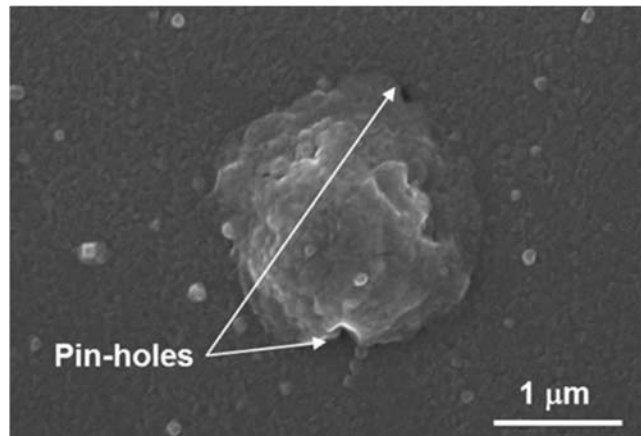
Fig. 2b. *SEM images of pinholes in the OBF.*

Initial testing showed that the OBF did not meet all of the REXIS science requirements. The requirements that are most affected by the pinholes are those concerned with the Large Area Pixel Performance (LAOP) and the Pixel Optical Density (POD). LAOP is calculated by counting the number of pixels where optical-light bleed-through above the noise floor is observed in areas that are directly illuminated with visible light. POD is calculated for all illuminated pixels by dividing the number of expected incident photons (accounting for the Gaussian beam intensity) by the number of detected photons for each pixel. Here we adopt the conventional definition of optical density as the common logarithm of the ratio of incident to detected photon flux. The lower the POD value for a pixel the

larger the fraction of incident light that made it through the OBF. In order for REXIS to meet its science requirements, LAOP must be less than 1% of the illuminated area and the fraction of pixels with POD < 7 must be less than 1% of the illuminated area. Ryu's testing showed that the LAOP was approximately 5% so the team at Lincoln Laboratory altered their process and significantly reduced the number of pinholes observed in the REXIS CCDs.

REXIS is the first MIT/NASA X-ray spectrometer to fly with a directly deposited optical blocking coating [4]. Because REXIS was developed as a risk-Class-D student instrument with limited budget, the performance of the OBF was not characterized before and after environmental testing. Therefore, it is not known how the number of pinholes will change in response to environmental stress. The goal of this study is to characterize the response of pinholes in the OBF to environmental stress as defined in NASA's General Environmental Verification Standard (GEVS). To do so, we conducted random-vibration and thermal cycling survival tests on the REXIS flight spare Detector Assembly Mount (DAM) to mature the OBF technology to NASA Technology Readiness Level (TRL) 6. This designation indicates that a system has been tested in relevant operational environments. The REXIS flight detector was launched on-board OSIRIS-REx in September 2016 and will not be exposed to optical light until the instrument cover is open in September 2018.

Methods

This section details the suite of testing performed to fully characterize how OBF performance is affected by environmental stress. The pinholes in the OBF are characterized by measuring the amount of optical light that leaked through the OBF and was detected by the CCDs. This light-leak test was performed before and after each environmental test, allowing quantification of OBF performance at each phase. The post-test OBF performance is compared to the pre-test baseline to determine if there is any change due to environmental stress. The intended test plan was to do an initial light-leak test to acquire a baseline of the OBF performance followed by a vibration test at Lincoln Laboratory and then the post-vibration light-leak test. The DAM was then to be thermally cycled eight times at the MIT Space System Laboratory with a final post-test light-leak test. The flow is shown in Fig. 3.
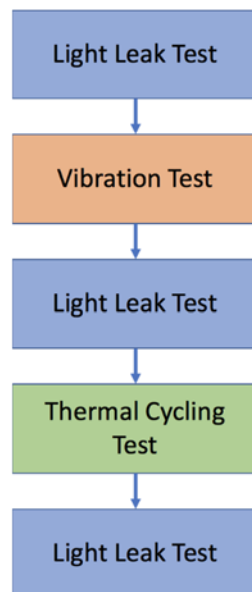
Fig. 3. Flow of intended OBF testing plan.

An Electromagnetic Compatibility (EMC) test was considered and the electrical properties of the OBF were examined during REXIS focal-plane testing (discussed in [2]). Since pinholes are thought to be

caused primarily by physical processes, we don't expect the number of pinholes to be affected by EMC testing, so this study did not pursue those tests.

OBF Performance Assessment

The first task in assessing the performance of the OBF was to verify that the OBF met the science requirements of the mission:

- LAOP should be less than 1% of the illuminated area; and
- The fraction of pixels with a POD < 7 must be less than 1% of the illuminated area.

In addition, it is necessary to ensure that the OBF does not deteriorate due to environmental testing even if it still meets the science requirements. If the performance gets worse by small amounts there is concern for the durability over the course of a long-term mission. As part of our initial light-leak testing, we developed the following requirements for baseline comparison between test environments.

- Post-environmental testing, LAOP per CCD should not increase by more than 2σ, where σ is the observed standard deviation derived from multiple measurements; and
- Post-environmental testing, the fraction of illuminated pixels with POD < 7 per CCD should not increase by more than 2σ, where σ is again the observed standard deviation derived from multiple measurements.

Light-Leak Test

For the light-leak test, the REXIS spare DAM was installed in a thermal vacuum chamber with an optical fiber suspended a few inches above the CCDs, positioned so that it directly illuminated portions of all four CCDs. The optical fiber was fed out of the chamber and attached to a 633-nm laser source. The fiber mount also held two ^{55}Fe sources that were always present whether or not the optical light was on. This configuration is shown in Fig. 4.

Fig. 4. Right: *Tower that supports the Laser and X-ray sources; flexprints from the CCDs come out of each side.* Left: *A) End of the laser positioned above the CCDs; B) ^{55}Fe sources; C) Four CCDs in the DAM with their numbering convention.*

The laser and fiber setup was calibrated before testing to determine the flux of the optical light on the detectors, given that losses accrue throughout the fiber-optic cabling, especially at connector junctions. To calibrate the output of the fiber, we placed a photodiode where the CCDs sit and measured the light

intensity at that location at increasing laser power levels. There is a 56.5% loss across the external and internal fibers. The laser settings and corresponding power output levels are listed in Table 1.

Laser Source Setting	Power Out of Fiber
0 mW	0 mW
2.8 mW	1.2 mW
4.8 mW	2.1 mW
10.5 mW	4.6 mW
24.5 mW	11.0 mW
58.6 mW	25.5 mW

Table 1. Illumination levels at the laser source and the power coming out of the end of the optical fiber for the light-leak test.

The calibration determines the total power of the laser beam out of the end of the fiber. The fiber is unterminated at the end, so the spread of the output light has a Gaussian intensity distribution. A basic geometrical approximation that accounts for the Gaussian nature of the output beam is used as the intensity scaling function for incident light on the detectors. The intensity scaling function I/I_0 is a function of distance from the beam axis (r) and is governed by Equation (1). The Gaussian beam radius, w_0, is the radius at which the intensity drops to $1/e^2$ of its peak value and is computed using Equation (2), where z is the distance from the detector to the end of the fiber optic cable, and α is the numerical aperture of the fiber.

$$I/I_0 (r) = e^{-\frac{2r^2}{w_0^2}} \quad (1)$$

$$w_0 = \tan(\arcsin(\alpha)) * z \quad (2)$$

The fiber manufacturer specified the numerical aperture of the fiber as 0.12. Adopting a value of $z \approx 47$ mm, we find $w_0 \approx 5.7$ mm. Given the measured fiber losses, for a laser power of 25.4 mW and the REXIS frame time of 4 s and pixel size of 24 μm, we find that the peak intensity $I_0 = 1.5 \times 10^{12}$ photons/pixel/frame.

The light-leak test is performed with the REXIS detector electronics and a commercial frame-grabber, allowing for faster acquisition of full frames of data. For each light-leak test, 100 frames were collected at each of the illumination levels specified in Table 1. The 10.5-mW and 25.4-mW levels bracket the optical light levels expected by REXIS at the asteroid and are the levels used to determine OBF performance.

In order to identify areas of light leak, it is necessary to remove the effects of both X-ray events and hot pixels from the data. Twenty-five (25) frames are taken with no illumination. The bias map is created from the clipped mean of these dark frames. A clipped mean removes any values that are above or below 3σ of the median value for each pixel, and calculates a mean with the remaining values. Calculating the mean in this manner removes any X-ray events from the bias frame given the low X-ray flux, while retaining any hot (high dark current) pixels that are present in all the frames. For each of the optical light levels, a clipped mean of 25 frames was also computed to remove X-ray events. The dark bias map is subtracted from each clipped mean illuminated frame, correcting for hot pixels. Figure 5 lays out the processing flow for a light-leak test.
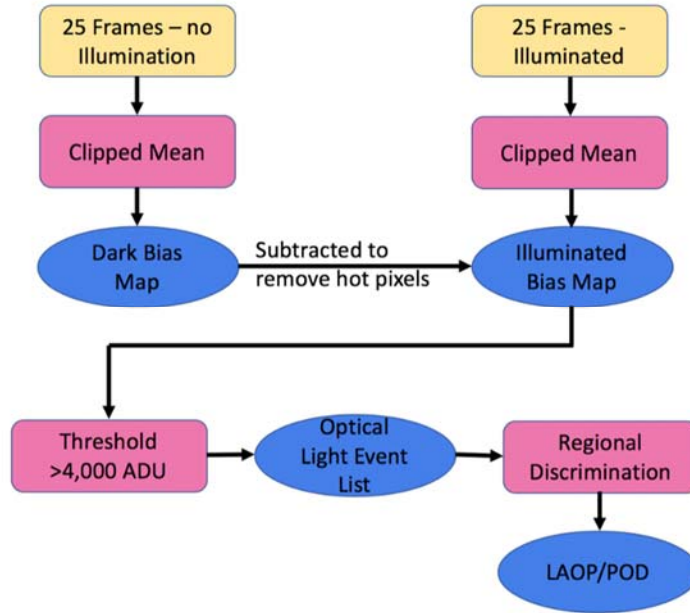
Fig. 5. *Light Leak data processing flow chart. A clipped mean is made from both 25 dark frames and 25 illuminated frames, the dark is subtracted from the illuminated mean. The 4000 ADU threshold is then applied to find all optical light events, those within the illuminated region are LAOP and POD pixels.*

The threshold used to determine whether or not a pixel had optical light in it was 4000 ADU. This is equivalent to approximately 30% higher than single-pixel [55]Fe events, so if any X-ray influence made it through into the bias image, they would not be included in the pinhole count.

From the position of the end of the optical fiber, sections of each CCD were defined as the illuminated regions and the pixels in those areas that were above the light-leak threshold are the ones that went into the count for LAOP. To determine the POD of each pixel in those regions, the intensity scaling function, Equation (1), was used to determine what the incident light falling on that pixel was vs. how much light was measured in that pixel.

After performing the initial light-leak tests, we realized that there is an inherent variability in our test setup, and perhaps in the detectors themselves, that resulted in small shifts in the number of measured pinholes between nominally identical tests. Therefore, each light-leak test was performed twice to characterize the test to test variability. Further discussion on test variability and the determination of the characterization criteria can be found below in the **Results** section, under "***Pre-Environmental Test Light-Leak Levels***".

From the initial light-leak testing, it was decided to use only two of the four CCDs (CCD0 and CCD2) in the spare DAM. CCD1 and CCD3 both had cosmetic defects that were unrelated to the OBF, but that made it difficult to firmly evaluate the pinholes in the OBF for those detectors. Figure 6 shows the detected pinholes in all four CCDs. CCD1 has an intermittent hot column near x=600. The noise intensity is variable and cannot be reliably subtracted out. Note that CCD3 allows light in through the side at the top edge of the detector. This large light leak scales with the intensity of the laser and dominates the data in such a way that makes it difficult to identify pinholes.
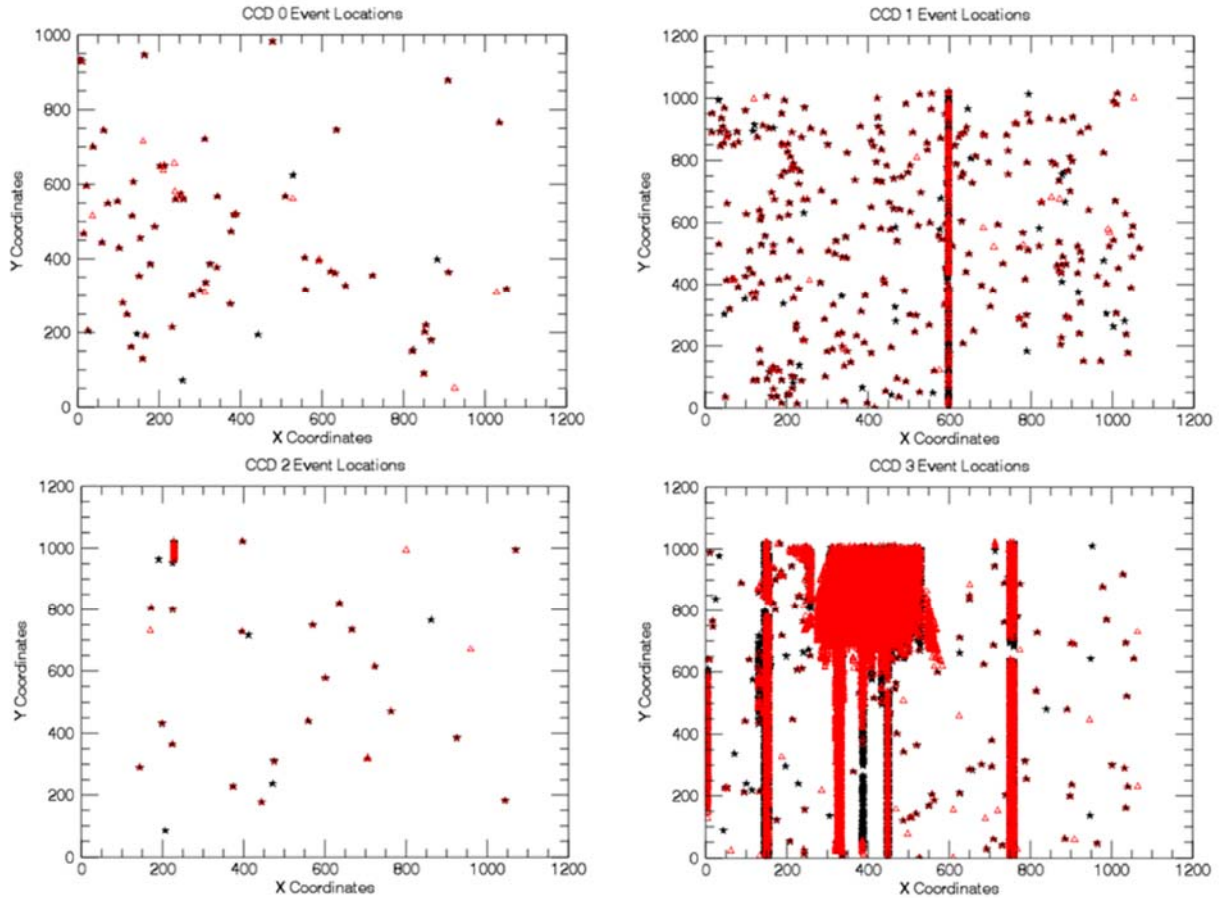
Fig. 6. *Pinhole Locations for all CCDs from the initial light-leak testing at 10.5 mW. The black stars are pinholes from the light-leak test on 11/15/17 and the red triangles are from the test on 12/14/17. CCD1 (upper right) and CCD3 (lower right) were disqualified from the OBF testing due to poor cosmetics.*

Vibration Test

The random vibration test is designed to expose the OBF to a vibration environment that envelopes that felt during launch. The DAM was tested at 14.1g random vibration at 20-2000 Hz. This test level and test spectrum comes from Table 2.4-3 in GEVS [1]. A low-level, white-noise, random vibe was performed before and after the full-level test to identify the natural frequencies of the system and check for frequency shifts. Tests were conducted on each of the three axes separately. The detector was not powered during vibration testing. Each axis started with a test at -18 dB relative to the full level, then -12dB, then -6dB, and finally the full level test.

The DAM was mounted to an adaptor plate, and the adaptor plate was mounted to a shake cube in the environmental test facility at Lincoln Laboratory. In order to accommodate the flexprints safely, the DAM was mounted at a 45° angle about the Z-axis of the cube, as shown in Fig. 7. The Z-axis for the cube and the DAM are the same, while the Y_{cube} /Y_{DAM} and X_{cube}/X_{DAM} are each 45° off from each other. This means that when the cube shakes in the Y-direction the DAM experiences vibrations in both the Y and X directions.
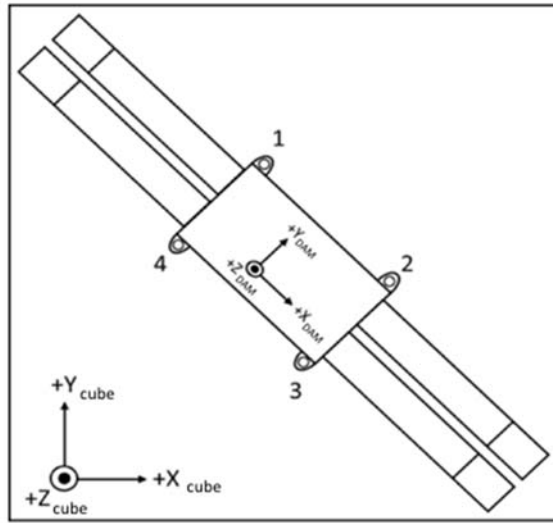
Fig. 7. *DAM mounted diagonally on adaptor Plate. Note that X and Y test axes (lower left) do not line up with X and Y DAM axes.*

Thermal Cycling

The proposed thermal cycling test was designed to expose the OBF to the range of temperatures it could experience during flight. During REXIS operation, the DAM is expected to see temperatures ranging from -90°C to -60°C so during this test the DAM was to be cycled eight times from -100°C to -50°C with a ramp rate of 3°C/min. The required stability was 1°C/hr for 15 minutes. The DAM does not have a large thermal mass, so once stability was achieved, the DAM would soak for 30 minutes at each temperature. The DAM was to be powered on and collecting event lists during cycling with the X-ray sources in place and the laser source turned off. The full REXIS electronics stack was to be used during cycling so that housekeeping channels could be monitored to ensure that the DAM was operating properly. One raw frame would be taken during each soak.

Test No.	Test Performed	Date	Min. Temp.	Max. Temp.
1	Initial light-leak test 1, part 1	11/15/17	-70 °C	-15 °C
2	Initial light-leak test 1, part 2	11/16/17	-70 °C	Room temp
3	Initial light-leak test, fiber problems – did not use data	12/1/17	-70 °C	Room temp
4	Initial light-leak test 2	12/14/17	-70 °C	Room temp
5	Post-vibration light-leak test 1	2/1/18	-70 °C	0 °C
6	Post-vibration light-leak test 2	2/2/18	-70 °C	Room temp
7	Light-leak test 1, 20°C colder ***not used for evaluation	2/26/18	-90 °C	-20 °C
8	Light-leak test 2, 20°C colder ***not used for evaluation	2/27/18	-90 °C	Room temp
9	Flipped DAM light-leak test	3/1/18	-70 °C	Room temp
10	Light-leak test after eight thermal cycles	6/12/18	-70 °C	Room temp

Table 2. *All light-leak tests performed with the spaceflight REXIS DAM. Not all tests were used for OBF evaluation.*

Due to time constraints and technical issues with one of the electronics boards, we were not able to complete an isolated thermal cycling test as initially planned. However, over the course of the initial

33

light-leak tests and the post-vibration light-leak tests, the DAM was thermal-cycled eight times between the first and last light-leak tests (Table 2). Six of the tests (2, 3, 4, 5, 6, and 9) saw the DAM stable at -70°C for over an hour and the other two tests (7 and 8) saw it at -90°C for over an hour. Although these temperatures are higher than the proposed low temperature, the DAM soaked at those temperatures longer than originally proposed. The DAM was never brought to a stable plateau at -50°C after each test. Instead, it was allowed to warm up to room temperature freely on its own after each test. For six of the tests (2, 3, 4, 6, 8, and 9) the DAM came up to room temperature and stabilized before it was cooled again. For the other two tests (5 and 7), the DAM was cooled again before it reached room temperature, having been between -20°C and 0°C. Given the thermal stress the detectors did see, we believe that the DAM underwent sufficient cycling to assess the effects of thermal cycling on the OBF.

Results

The light-leak test was performed at the start of testing and then again after vibration testing and thermal cycling. The results from all subsequent tests are presented in comparison to the initial light-leak test.

Pre-Environmental Test Light-Leak Levels

The initial light-leak tests confirm that the OBF on the spare CCDs did have some pinholes that allowed optical light through before environmental testing began. Figure 8 shows the location and spread of the pinholes in the OBF for CCD0 and CCD2. For CCD0 the illuminated area was 527 pixels by 314 pixels and for CCD2 it was 300 pixels by 514 pixels. For reference, each CCD is 1024×1024 pixels. Pinholes were detected outside of the defined illuminated area. These are likely due to the scattering of the uncollimated light from the fiber. These pinholes are not included when calculating LAOP.
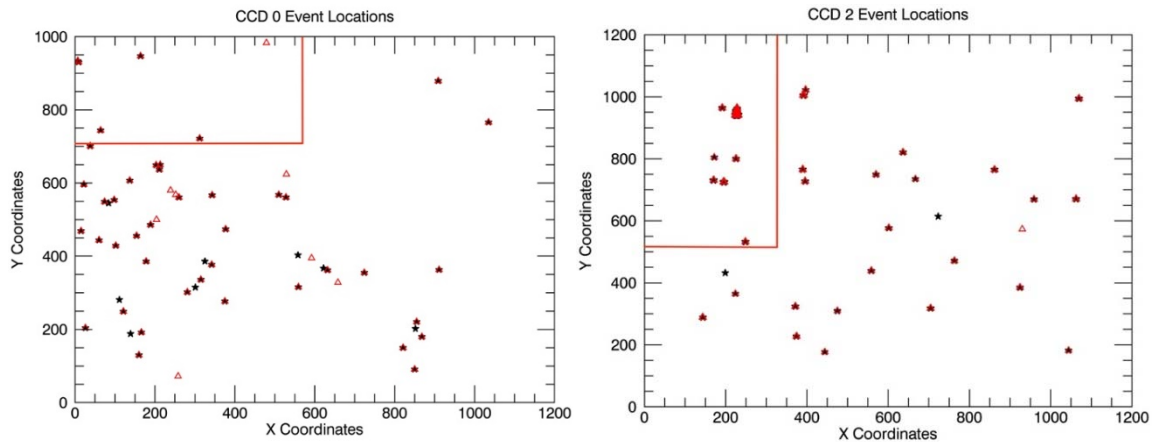
Fig. 4. *Locations of pinholes in CCD0 and CCD2 during the pre-environmental tests at 25.4 mW. Black stars are pinholes from the light-leak test on 11/15/17 and 11/16/17 and red triangles are pinholes from the light-leak test on 12/14/18 .The red lines define the illuminated portion of each CCD. Note that each CCD spans 1024 pixels in X and Y, so regions with X or Y > 1024 on these figures are outside the detectors.*

The aim of the initial light-leak test was to establish the baseline performance of the OBF for each of the CCDs. Since we wanted a solid baseline to start from, we did more than one test, which led us to the realization that there was some variability in our results due to our test setup. Originally, the requirement for acceptable variability was that the LAOP could not change by more than 10%, and we were not meeting that due to the relatively small values of LAOP for CCD0 and CCD2. When LAOP is 9 pixels (Table 3), 10% is 0.9 so having a shift of a single pixel was enough to mark a test as a fail for OBF performance. Given the small number of pixels affected, we modified the criteria on OBF stability for LAOP and POD < 7 to use σ values relative to the initial values.

Initial Tests 10.5 mW	11/15/17, 11/16/17 Test LAOP	11/15/17, 11/16/17 LAOP fraction of total pixels	12/14/17 LAOP	12/14/17 LAOP fraction of total pixels	2σ	Change in LAOP
CCD0	9	0.01%	8	0.01%	1.4	1
CCD2	75	0.05%	72	0.05%	4.2	3
25.4 mW						
CCD0	16	0.01%	14	0.01%	2.8	2
CCD2	120	0.08%	124	0.08%	5.6	4

Table 3. *Initial light-leak levels. LAOP for CCD0 and CCD2 at 10.5 mW and 25.4 mW. The fraction of LAOP pixels is in relation to the total number of pixels in the illuminated region (2σ of LAOP calculated from average LAOP).*

The baseline pre-environmental LAOP for both CCDs was found to be well below 1% of the illuminated area as required for REXIS science operations, and the change in LAOP between runs was less than 2σ for 10.5 mW and 25.4 mW (Table 3). The number of pixels with POD < 7 was also below 1% of the illuminated area, and this number did not vary by more than 2σ between runs (Fig. 9). These results gave us confidence that we could detect any change in LAOP or POD that indicated OBF deterioration.
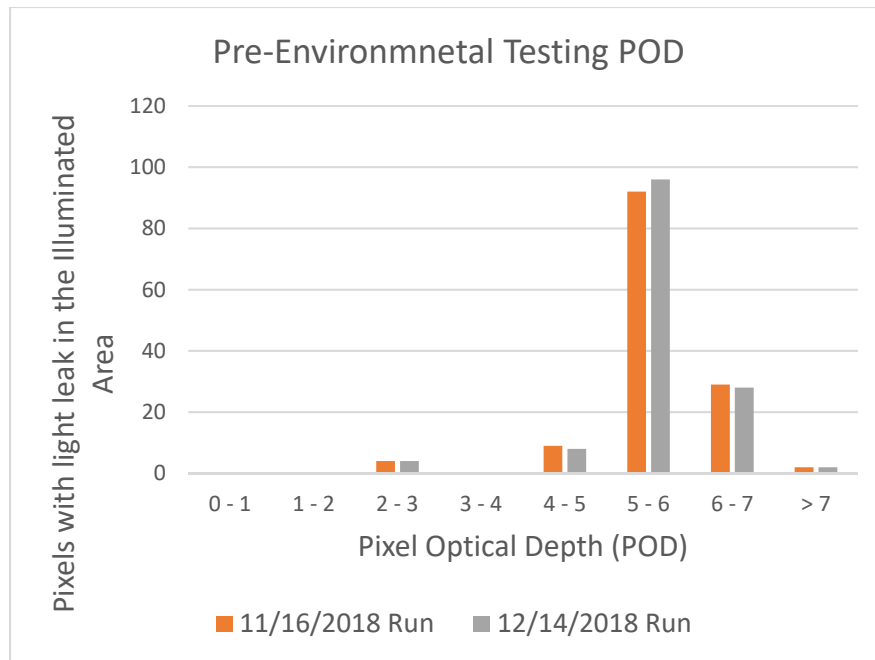
Fig. 5. *Pre-environmental POD distribution of the pixels with light leak in the illuminated area at 25.4mW. Each run shows the combined count from CCD0 and CCD2. The 11/16/17 run had 134 pixels with POD < 7 which is 0.04% of the illuminated area. The 12/14/17 run had 136 pixels with POD < 7 which is 0.04% of the illuminated area.*

Vibration Test Results

The vibration test was conducted at Lincoln Lab on January 16, 2018. For all three axes, there was no significant change in the natural frequencies of the DAM system on the adaptor plate before and after the random vibration test. Figure 10 below shows the overlaid frequency curves from the accelerometers located on the X, Y, and Z axes from the corresponding axis vibration test.
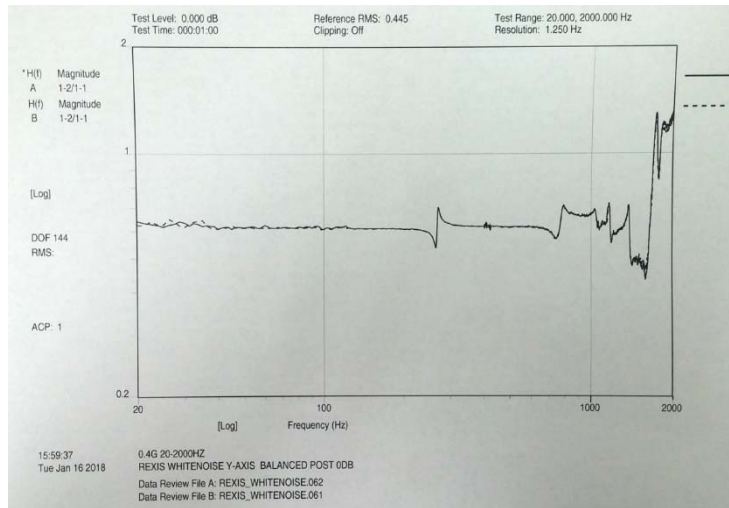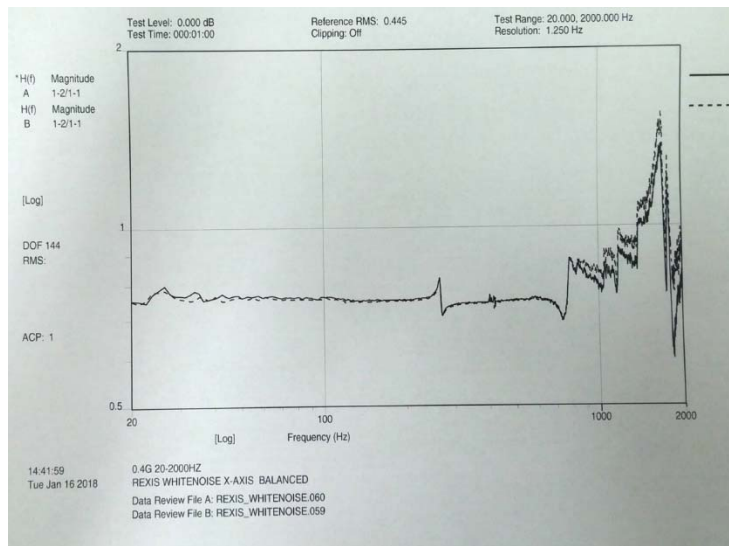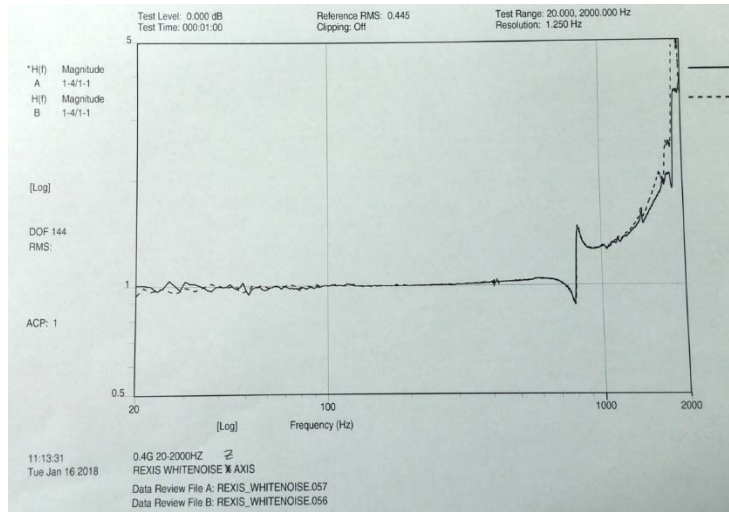
Fig. 10. The natural frequencies from the initial low-level white noise overlaid with the post-random-vibe low-level white-noise frequencies for the Z_{cube} axis (top), X_{cube} axis (middle) and Y_{cube} axis (bottom).

At some point during the vibration tests, two of the CCDs became unbonded from their mounts in the DAM and were free to move within the DAM. Continuing the test with two loose CCDS resulted in some scratches to the CCD surfaces, some bent bond wires and damage to the corner of one detector, making these two detectors unusable. Fortunately, the two CCDs that were damaged were the two that had already been ruled out for OBF performance determination due to poor cosmetics. These CCDs were removed from the DAM at Lincoln Labs before coming back to MIT, to remove the risk that the loose CCDs could damage the other two detectors.

Post-Vibration-Test Light-Leak Levels

The light-leak tests performed after the vibration test show minimal change in OBF performance. The pinhole locations before and after the vibration test are shown in Fig. 11. Some individual pixels show up in one test but not in others, but it should be remembered that with two of the four CCDs removed from the DAM, the environment for scattered light is different. Note that on CCD2 at location (~850, ~50) there is a clump of pinholes that did not appear in the pre-vibration tests. These were not in the defined illumination area so they do not affect the LAOP for CCD2. However, they do seem to be a real light leak in the OBF. A supplemental light-leak test was done with the DAM installed 180° from its nominal position, and the clump of pinhole pixels was still present, meaning that those pixels are the result of pinholes. It is possible that in the initial light-leak test those pinholes already existed but were not illuminated, or they could be new after the vibration test.
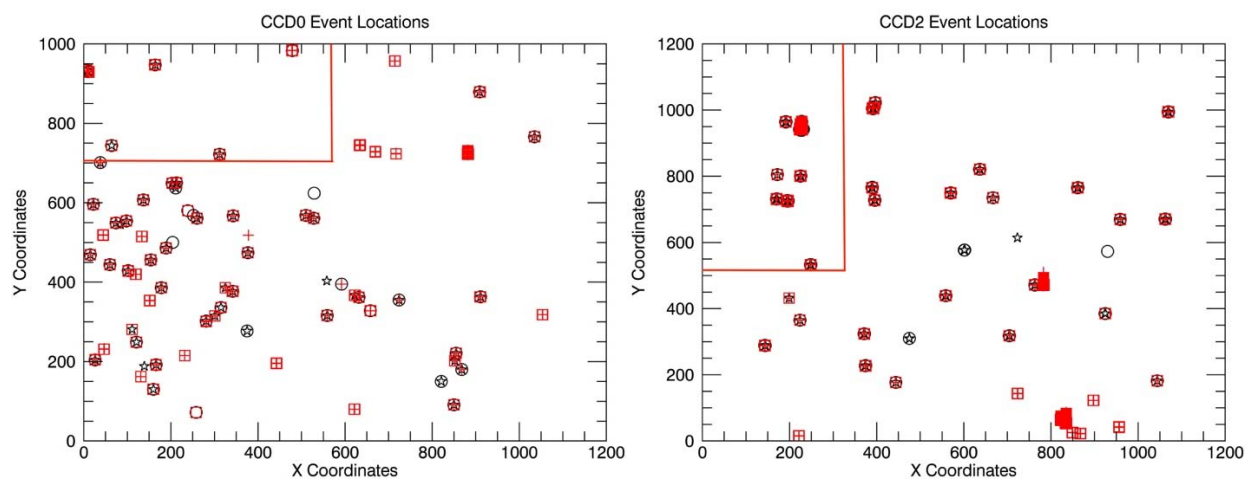
Fig. 11. *Locations of pinholes in CCD0 and CCD2 during the post-vibration tests at 25.4 mW in comparison with the pinholes from the initial light-leak test. Black stars and circles are pinholes from the two pre-vibration tests and red squares and crosses are pinholes from the two post-vibrations tests. The red lines define the illuminated portion of each CCD. Note that each CCD spans 1024 pixels in X and Y, so regions with X or Y > 1024 on these figures are outside the detectors.*

Approximately two months passed between the initial light-leak test and the two post-vibration tests, and the test setup maintained the stability that it had before the vibration test. The LAOP values between runs were within a few pixels of each other as presented in the "Change in LAOP" column of Table 4. The LAOP for CCD0 stayed nearly identical to the LAOP pre-vibration test while the LAOP values for CCD2 decreased marginally (Table 5). This slight variation is well below the tolerated change in LAOP between environmental tests and the final LAOP is still well below 1% of the total illuminated region. The fraction of pixels with POD < 7 after vibration testing was significantly below 1% (Fig. 12). The average total number of pixels with POD < 7 before vibration test was 135, and after the vibration test it was 130.5 showing consistency across tests.

Post-Vibe 10.5 mW	2/1/18 LAOP	2/1/18 LAOP fraction of total pixels	2/2/18 LAOP	2/2/18 LAOP fraction of total pixels	2σ	Change in LAOP
CCD0	9	0.01%	10	0.01%	1.4	1
CCD2	66	0.04%	64	0.04%	2.8	2
25.4 mW						
CCD0	15	0.01%	16	0.01%	1.4	1
CCD2	115	0.08%	118	0.08%	4.2	3

Table 4. *Light-leak level after vibration test. LAOP for CCD0 and CCD2 at 10.5 mW and 25. 4mW. The fraction of LAOP pixels is in relation to the total number of pixels in the illuminated region (2σ of LAOP calculated from average LAOP).*

10.5 mW	Average LAOP Initial Light-leak testing	Maximum Acceptable Post-Vibe LAOP	Average LAOP Post-Vibe	Pass/Fail
CCD0	8.5	10.5	9.5	Pass
CCD2	73.5	78.5	65	Pass
25.4 mW				
CCD0	15	18.2	15.5	Pass
CCD2	122	129	116.5	Pass

Table 5. *Change in LAOP between initial light-leak tests and post-vibration light-leak tests at 10.5 mW and 25.4 mW. OBF performance for each CCD met the requirements.*
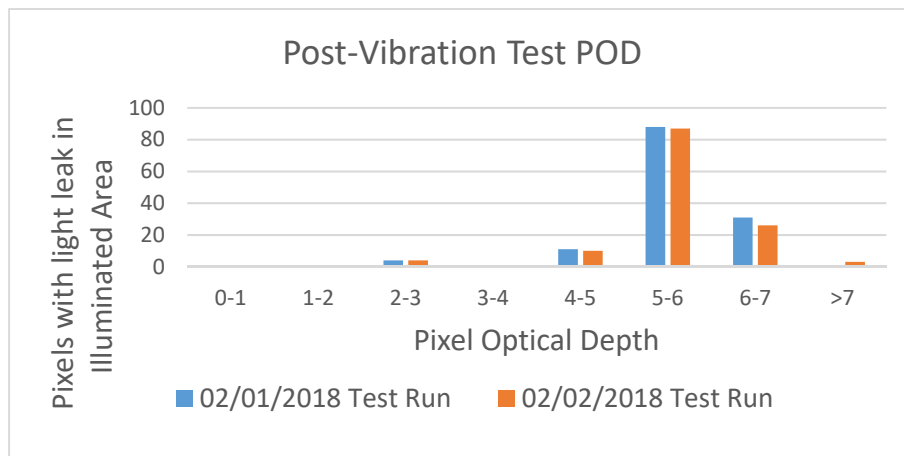
Fig. 12. *Post-vibration-test POD distribution of pixels with light leak in the illuminated area at 25.4 mW. Each run shows the combined count from CCD0 and CCD2. The 2/1/18 run had 127 pixels with POD < 7, which is 0.04% of the illuminated area. The 2/2/18 run had 134 pixels with POD < 7, which is 0.04% of the illuminated area.*

Post-Thermal-Cycling Light-Leak Levels

After the DAM had seen eight thermal cycles, another light-leak test was performed. This test was four months after the post-vibration light-leak test, but the DAM had not undergone any other testing in that time. Due to time constraints and the repeated stability in previous tests only one light-leak test was done to evaluate OBF performance after thermal cycling.

The results of the light-leak test after thermal cycling show that thermal cycling the CCDs does not deteriorate the performance of the OBF. Figure 13 shows the location of the detected pinholes in both CCDs, and they still map to their locations in the initial light-leak tests. LAOP remained significantly

below 1% of the illuminated area. Table 6 lists the total number of pixels that make up LAOP for each CCD and the LAOP fraction of the total potential pixels. Since there was only one test, we used the single values from that test instead of an average to compare to the number from the initial light-leak test. Both CCDs in both illumination levels had LAOP numbers less than 1σ lower than the initial light-leak LAOP (Table 7). The total combined number of pixels with POD < 7 was 117 compared to 135 from the initial light-leak test (see distribution and count of POD in Fig. 14). Since both the values for LAOP and POD < 7 decreased instead of increased, we are confident that any variation that was present between tests is due to variability of the system and not from a physical change in the OBF.
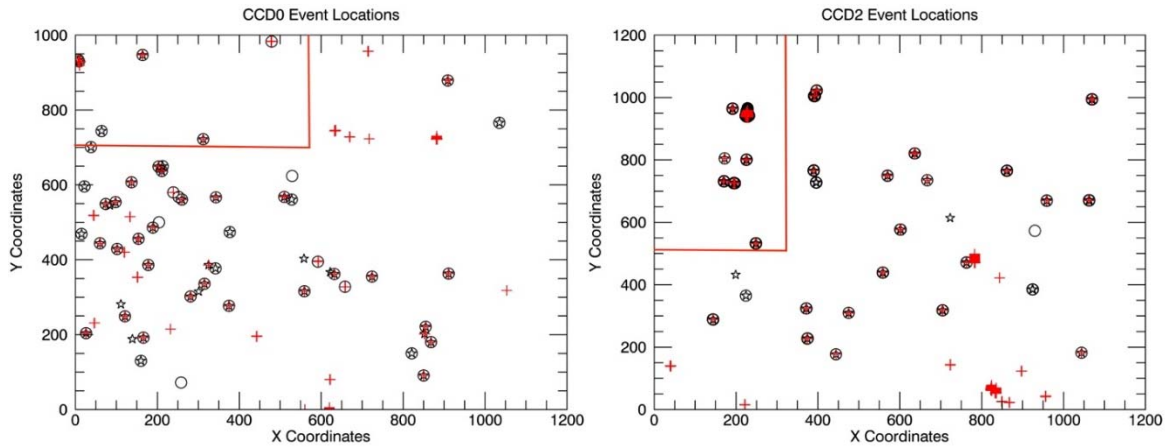
Fig. 6. *Locations of the pinholes in CCD0 and CCD2 during post-vibration tests at 25.4 mW in comparison with the pinholes from the initial light-leak test. Black stars and circles are pinholes from the two initial light-leak tests and red crosses are pinholes from the post-thermal cycling test. The red lines define the illuminated portion of each CCD. Note that each CCD spans 1024 pixels in X and Y, so regions with X or Y > 1024 on these figures are outside the detectors.*

Initial Tests 10.5 mW	6/12/18 Test LAOP	6/12/18 LAOP fraction of total pixels
CCD0	6	0.01%
CCD2	60	0.05%
25.4 mW		
CCD0	13	0.01%
CCD2	107	0.08%

Table 6. *Light-leak level after thermal cycling. LAOP for CCD0 and CCD2 at 10.5 mW and 25.4 mW. The fraction of LAOP pixels is in relation to the total number of pixels in the illuminated region. Only one test was done for this light-leak test.*

10.5 mW	Average LAOP Initial Light-leak testing	Maximum Acceptable Post-Thermal Cycling LAOP	Average LAOP Post-Thermal Cycling	Pass/Fail
CCD0	8.5	10.5	6	Pass
CCD2	73.5	78.5	60	Pass
25.4 mW				
CCD0	15	18.2	13	Pass
CCD2	122	129	107	Pass

Table 7. *Change in LAOP between initial light-leak tests and the post-thermal cycling light-leak test at 10.5mW and 25.4mW. The OBF performance for each CCD met the requirements*
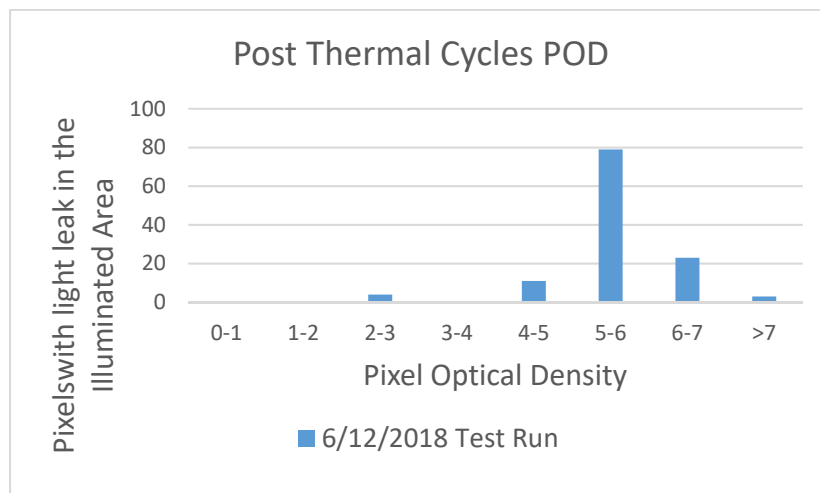

Fig.14. *Post-thermal-cycling POD distribution of pixels with light leak in the illuminated area at 25.4 mW. Shown is the combined count from CCD0 and CCD2.There are 117 pixels with POD < 7, which is 0.04% of the illuminated area.*

Conclusions

The aim of this testing was to determine whether the performance of the OBF on the REXIS CCDs was affected by the environmental stresses of launch and the thermal environment in space. We were able to establish that the vibrations experienced during a launch would not cause a deterioration of the OBF, and that the amount of optical light that leaked through to the CCDs did not change above the noise floor of our setup after a vibration test. The results also showed that thermal-cycling the CCDs with OBF through the REXIS operating temperatures did not degrade OBF performance. The REXIS science requirements stipulate that the LAOP but be less than 1% of the science-gathering area and that the pixels with a POD < 7 must be less than 1% of all pixels. We proved that the OBF technology designed by Lincoln Laboratory can meet the REXIS requirements both before and after environmental stress. Given this characterization of the OBF behavior under stress, we believe that the OBF technology can be matured to NASA TRL 6.

The detectors currently in flight on REXIS were evaluated for pinholes in their OBF before any environmental testing and they met the requirements, so we expect that when the REXIS cover opens and optical light shines on the detectors, the OBF performance will still be acceptable. There are plans to evaluate the flight OBF using the asteroid before REXIS begins science observation, and to mask out the pinholes so they do not get counted as X rays from Bennu.

References

[1] B. Allen et al., "*The REgolith X-Ray Imaging Spectrometer (REXIS) for OSIRIS-REx: identifying regional elemental enrichment on asteroids,*" in SPIE Optical Engineering+ Applications (2013)

[2] K.K. Ryu, B.E. Burke, H.R. Clark, R.D. Lambert, P. O'Brien, V. Suntharalingam, C.M. Ward et al., "*Development of CCDs for REXIS on OSIRIS-Rex,*" In SPIE Astronomical Telescopes+ Instrumentation, pp. 91444O-91444O, International Society for Optics and Photonics (2014)

[3] A.D. Rakic, A.B. Djurivic, J.M. Elazar and M.L. Majewski, "*Optical Properties of Metallic Films for VerticalCavity Optoelectronic Devices,*" Appl. Opt., **Vol. 37**, no. 22, pp. 5271-5283 (Aug 1998)

[4] M. Jones, M. Chodas, M.J. Smith, and R.A. Masterson, "*Engineering design of the REgolith X-ray Imaging Spectrometer (REXIS) instrument: An OSIRIS-REx student collaboration,*" In SPIE Astronomical Telescopes+ Instrumentation, pp. 914453-914453. International Society for Optics and Photonics (2014)

Providing Enabling and Enhancing Technologies for a Demonstration Model of the Athena X-IFU

Prepared by: Caroline Kilbourne (PI; NASA/GSFC); Simon Bandler, James Chervenak, Stephen Smith and Nicholas Wakeham (NASA/GSFC); Joel Ullom and W. Bertrand Doriese (NIST); Kent Irwin (Stanford University)

Summary

The Advanced Telescope for High ENergy Astrophysics (Athena) has been selected by the European space agency for launch in 2028. The purpose of the mission is to observe X rays emitted from the hot and energetic universe to address questions about the formation of large structures in the universe, study the evolution of black holes, and in general to observe many high-energy astrophysical targets of interest [1]. The X-ray integral field unit (X-IFU) is one of two baselined instruments on Athena. This instrument will be capable of high-resolution spectroscopy with 2.5 eV energy resolution for 7 keV X rays, and high spatial resolution over a wide field of view of 5 arcmin [2]. To achieve this unprecedented capability, X-IFU will use transition edge sensor (TES) microcalorimeter pixels developed in a long-standing collaboration between NASA, NIST, and Stanford University. While the required energy resolution has been routinely achieved on the scale of one to tens of pixels, the collaboration is now focusing on optimizations to allow the required performance simultaneously on the kilo-pixel scale required for X-IFU.

We recently demonstrated that by altering the TES design we are able to improve the reproducibility and uniformity of large, uniform arrays of detectors. We also made adjustments to key TES parameters to improve the spectral resolution when pixels are read out using the baselined alternating current (AC) technique led by Space Research Organization Netherlands (SRON). This allowed, for the first time, the spectral resolution achieved under AC bias to be comparable to that using the direct current (DC) bias technique traditionally used in our collaboration. While this improvement in performance under AC bias continues, we also completed a study and report formally presenting a DC-biased method, as a backup readout for X-IFU.

Background

The baseline design for X-IFU uses TES microcalorimeters fabricated at NASA Goddard Space Flight Center (GSFC) and developed by our collaboration. These microcalorimeters consist of a Mo/Au bilayer superconducting TES cooled to 55 mK and held in the transition by an applied electrical bias. An incident X ray is absorbed in a Bi/Au absorber that is thermally connected to the TES. The change in temperature caused by the absorption of an X ray causes a change in resistance and hence current through the TES, which is measured using a Superconducting Quantum Interference Device (SQUID).

X-IFU will have ~4000 pixels. Each pixel will not be read out individually, but instead will be multiplexed so that many pixels can be read out in a single chain. The currently baselined technology for this multiplexed readout uses a frequency domain multiplexing (FDM) technology lead by SRON, whereby the TESs are AC-biased, with a set of frequencies where one frequency corresponds to one TES in the chain. Until recently, the resolution achieved with this AC readout was consistently degraded relative to the DC readout traditionally used for these devices. This degradation was shown to be highly dependent on the bias frequency, severely limiting the useable bandwidth. However, a great deal of work has been done over the last year to improve pixel performance when using FDM, and recent results showed multiplexing of 9 pixels with a spectral resolution of 2.6 eV.

In Time Division Multiplexing (TDM), pixels are DC-biased and multiplexed by reading out each pixel in a chain only a fraction of the total time, sequentially and cyclically. This readout scheme is quite mature and was utilized in a number of ground-based applications already. The TDM readout is seen as a possible backup readout system for the X-IFU. In parallel to the optimization of pixels using FDM, the collaboration has also continued to strive for the optimum performance using TDM, while also demonstrating this technology is a viable backup for X-IFU. This involved improving the readout architecture and noise mitigation, as well as making changes to the TES design to further improve on the excellent spectral resolution already achieved. Last year, we reported on TDM readout of 144 pixels with a median energy resolution of 2.75 eV. We have continued working on improving on this result to read out more pixels with even better spectral resolution.

Progress and Accomplishments

Array Uniformity

The 4096 pixels on X-IFU must all meet the very high spectral performance required for success of the Athena mission. Because of the multiplexed readout and common biasing of the detectors, extremely high uniformity of behavior of each pixel is required, so that every pixel in a given chain has a similar dependence on external parameters. One aspect of achieving this uniformity is device fabrication. Inevitably, there will be some variation in, for example, the thickness of the superconducting bilayer of the TES across the array, which can lead to variations in performance. Hence, we recently fabricated device wafers using a new physical vapor deposition system that has shown a potential improvement in uniformity of these bilayers. However, even if each pixel were fabricated to be identical, there may still be variations in performance because of gradients in external magnetic field, temperature, etc. Therefore, it is important to minimize pixel sensitivity to external parameters and non-ideal fabrication.

The traditional design of TESs produced at GSFC were 140 μm square with gold stripes across the TES, perpendicular to the current direction as shown in the inset to Fig. 1. These designs routinely show an energy resolution better than 2 eV and have been used in demonstrations of multiplexed readout of up to 190 pixels using TDM. However, these devices typically have a region of resistive transition that is not smooth, but rather with a 'kink' in the TES resistance vs. temperature curve, as shown in Fig. 1. Excellent energy resolution can only be achieved by using a region of the transition sufficiently far from this dramatic feature. This 'kink' is also sensitive to temperature, magnetic field, and small variations in fabrication, and so has a potentially large impact on performance uniformity

of large pixel arrays. Our recent work has shown that the presence of these kinks in the transition is highly dependent on the presence and spacing of the gold stripes that were added to the TES [3]. By removing these stripes, we were able to consistently produce devices that do not show kinks in the resistive transition, as shown in Fig. 1.
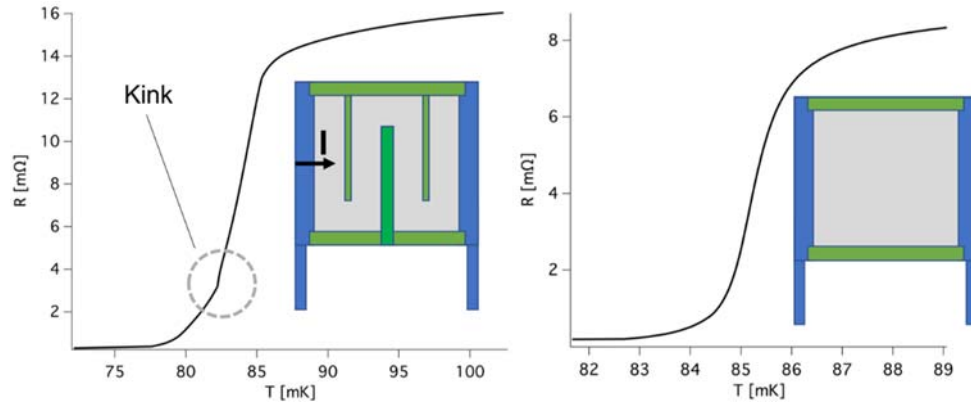
Fig. 7. *Resistance (R) as a function of temperature (T) of TES. Inset shows schematic diagram of TES design. Mo electrical leads (blue) are shown connected to a Mo/Au superconducting bilayer (gray). Gold metal (green) is added on top of the bilayer.* Left: *TES with gold metal 'stripes' added onto bilayer perpendicular to current flow (I). R shows the characteristic 'kink' highlighted with dashed circle.* Right: *Device without stripes shows no kink in the transition.*

This allowed a great improvement in the reproducibility of pixel performance across an array, and between different arrays with the same design. Stripes were originally added to the TES design because they were shown to improve pixel performance in larger devices by reducing electrical noise. However, in 50–140 μm square TESs, we were able to achieve excellent spectral performance in single-pixel readout, and have begun demonstrations of multiplexed readout of kilo-pixel arrays of these no-stripe designs.

Improved AC-Bias Performance

The reproducibility and uniformity of the kilo-pixel arrays of TESs is greatly improved in the new no-stripe designs, as tested under DC bias at GSFC. However, the baseline readout technology for X-IFU is using FDM, where pixels are AC-biased. The behavior of the TES under AC bias has been shown to be significantly different than under DC bias, and the spectral performance of pixels under AC bias has always been degraded compared to performance under DC bias. Our extensive study has shown that there are at least two reasons for this. The first is that the alternating electrical current in the TES and connecting leads induces dissipative currents in the surrounding metal of the detector pixel. In particular, this mostly occurs in the gold of the X-ray absorber, which is directly above the TES. This dissipative loss causes a loss in sensitivity of the TES to the temperature change from an incident X ray when measured with high-frequency AC [4]. We have implemented two strategies to mitigate this effect. The first is to increase the distance between the gold of the X-ray absorber and the TES. This reduces the induced current in the gold. The second is to significantly increase the resistance of the TES so that the energy loss of the dissipative currents is relatively small. The second effect of the AC current is to produce a small oscillatory component in the TES resistance vs. temperature curve. This arises because of an interaction between the TES and the superconducting leads. Work is still ongoing to fully understand this behavior, but these oscillations are minimized by the increase in the resistance of the TES and the removal of the metal stripes on top of the TES [5].

With these improvements to the TES design, we have now produced pixels that have a full-width half-maximum (FWHM) energy resolution of under 2 eV under AC bias, as shown in Fig. 2, and can be multiplexed up to high frequencies without significant degradation of energy resolution.
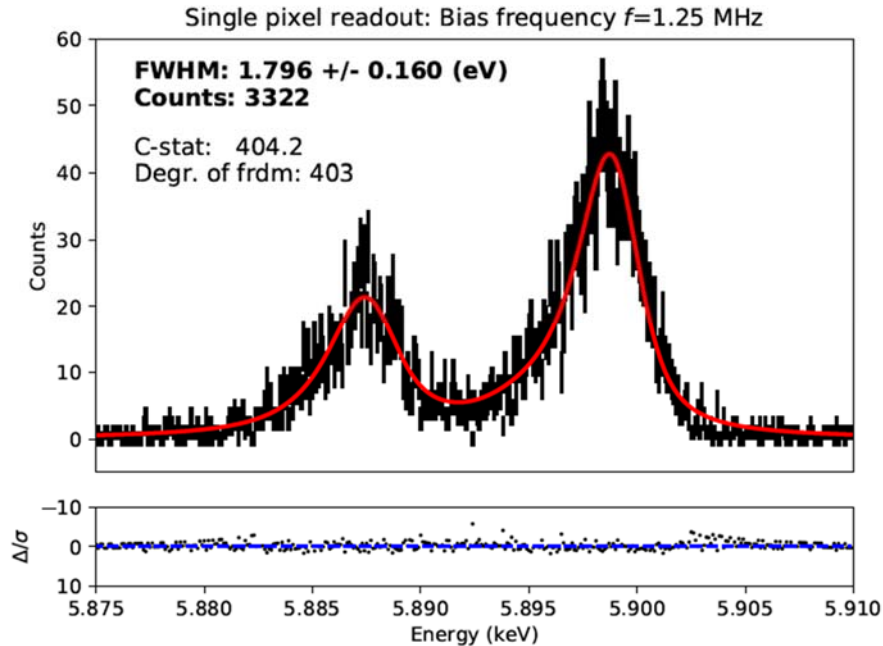
Fig. 8. *Measured energy spectrum of Mn-Kα (black) using alternating current bias of the TES at 1.25 MHz on a no-stripe device. Solid line (red) shows predicted spectrum with fitted Gaussian broadening.*

As a major milestone towards the X-IFU, GSFC recently sent a kilo-pixel array of these improved pixels for use as a demonstration model at SRON. We are continuing to study, understand, and improve these devices to ensure the best possible spectral performance.

TDM Backup

FDM readout is the baseline technology for the X-IFU, and, as shown above, great progress has been made in developing the pixels and readout. Nevertheless, to mitigate risk, we simultaneously considered TDM, and its related variant, Code-Division Multiplexing (CDM), as a backup readout in the event that the required performance cannot be achieved with FDM. This backup TDM readout scheme is well established, but as has not yet been demonstrated in a flight-like project. Therefore, this year a formal study began to consider all the implications of switching from an FDM to a TDM readout scheme in Athena, should it be determined that this switch is necessary. This study involved collaboration between NIST, GSFC, Stanford University, Centre National d'Etudes Spatiales (CNES), Research Institute in Astrophysics and Planetology (IRAP), and the Astroparticle and Cosmology (APC) laboratory in Paris. The report produced from this study will be completed in August 2018. It will be part of the package of material to be considered in the upcoming Instrument Preliminary Requirements Review for the X-IFU, which will take place in December 2018.

As part of the work to develop the readiness of TDM readout for X-IFU, we recently began a demonstration of the readout of 256 pixels of the new no-stripe TES design, showing improved transition-shape uniformity. Design improvements and testing have also continued on TDM and CDM components to improve performance by maximizing dynamic slew ratio while minimizing cross-talk, power, and space. Specific steps forward include:

- Development of TDM chips with input mutual inductance optimized for Athena TESs;
- Development of CDM chips with row count and input mutual inductance optimized for the X-IFU Focal Plane Assembly (FPA);
- Study and improvement of capacitive crosstalk in signal lines between FPA and 300K electronics;
- Progress towards SQUID series arrays optimized for 2K operation;

- Development of Nyquist chips with inductances optimized for Athena TESs; and
- Development of Nyquist chips with integrated cryotron switches and demonstration of configurable error correction in 16-row CDM measurements.

Production and Testing of Athena-Like Arrays

Detector arrays that have tested to date have had at most 1032 pixels, with only 256 pixels wired out. These arrays allowed us to test many different TES designs and improve both design and fabrication through a deeper understanding of the physics involved. However, we are now looking toward production of an engineering model that will simulate the array design to be used in the Athena mission. This array will have 4096 pixels in the center of a hexagonal wafer. The first of these arrays has now been produced. and we are building the test setup for this unique array design. Figure 3 shows one of these Athena-like arrays on the newly completed test platform. This test platform is the same design as the X-IFU FPA, and will soon be placed inside a cryostat already running at GSFC.
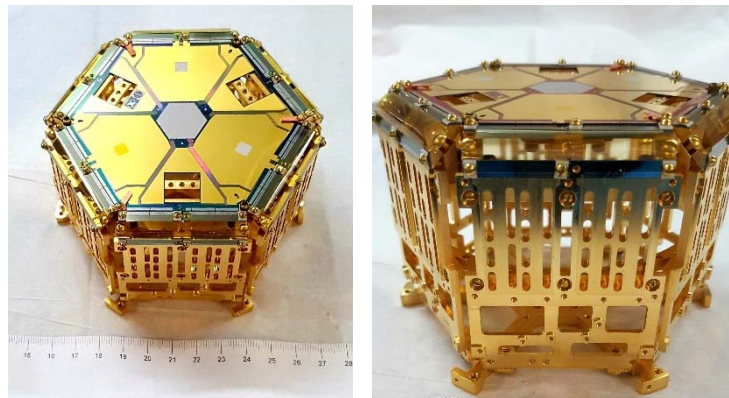
Fig. 9. Athena-like hexagonal detector array in the center of a hexagonal wafer, mounted on top of a new test setup designed to match the X-IFU FPA. Scale shown in centime*ers*.

Path Forward

In the coming year, we will continue to optimize the TES design to improve performance, uniformity, and reproducibility. In particular, recent measurements were performed on TES designs that are rectangular rather than square. These designs allow even higher resistances without compromising other performance aspects, and have shown promising results. In the near future, we will produce large arrays of these rectangular TES devices to more fully characterize their properties and suitability for X-IFU.

With the development of the new test cryostat and FPA infrastructure, we will begin testing the flight-like arrays, as well as beginning to routinely test hundreds of pixels in a single run on smaller kilo-pixel arrays. This will provide more information on array uniformity and robustness of our designs, which will feed back into further improvements.

As the testing of the demonstration model begins at SRON, we will gain more information on the performance of our latest designs using FDM, and where we can continue to make improvements.

References

[1] X. Barcons et al., "*Athena: the X-ray observatory to study the hot and energetic Universe,*" J. Phys.: Conf. Ser. **610** 012008 (2015), DOI: 10.1088/1742-6596/610/1/012008 (2015)

[2] L. Ravera et al., "*The X-ray Integral Field Unit (X-IFU) for Athena,*" Proc. SPIE, **9144**, 13, DOI:10.1117/12.2055884 (2014)

[3] N.A. Wakeham et al., "*Effects of Normal Metal Features on Superconducting Transition-Edge Sensors*," J. Low Temp Phys, DOI:10.1007/s10909-018-1898-z (2018)

[4] K. Sakai et al., "*Study of Dissipative Losses in AC-Biased Mo/Au Bilayer Transition-Edge Sensors*," J. Low Temp Phys DOI: 10.1007/s10909-018-2002-4 (2018)

[5] L. Gottardi et al., "*Josephson Effects in Frequency-Domain Multiplexed TES Microcalorimeters and Bolometers*," Journal of Low Temperature Physics, https://doi.org/10.1007/s10909-018-2006-0 (2018)

For additional information, contact Caroline Kilbourne: *caroline.a.kilbourne@nasa.gov*

Hybrid Lightweight X-ray Optics for Half-Arcsecond Imaging

Prepared by: Paul B. Reid (PI; Smithsonian Astrophysical Observatory, SAO) and Eric Schwartz (SAO)

Summary

"*Hybrid Lightweight X-ray Optics for Half Arcsecond Imaging*," NASA Contract NNX17AG77G, is a Strategic Astrophysics Technology (SAT) program that began 21 February 2017 and is scheduled to run through 20 February 2019. Initial funding was provided by NASA on 10 May 2017. This program follows separate earlier Astrophysics Research and Analysis (APRA) and SAT projects on the development of adjustable X-ray optics and differential deposition. The program seeks to develop modular, grazing-incidence, X-ray-mirror technology to achieve 0.5-arcsec imaging while also achieving extremely lightweight mirror assembly mass per unit effective area (e.g. < 500 kg/m² effective area, compared to ~ 16,000 kg/m² for Chandra). Our technology will enable large-area, high-resolution imaging-X-ray telescope mission concepts such as Lynx (formerly X-ray Surveyor, recommended by the 2013 NASA Astrophysics Roadmap [1]). Lynx will study the early universe (growth of structure, merger history of black holes), as well as feedback and evolution of matter and energy.

The hybrid mirror concept couples the two mirror technologies of thin-film adjustable optics and differential deposition. This hybrid approach can eliminate the figure errors and unwanted distortions usually inherent in thin lightweight mirrors. The adjustable optic technology employs a thin (nominally 1.5 μm) film of the piezoelectric material lead zirconate titanate (PZT), sputtered as a continuous film on the back of thin (0.4 mm) thermally formed glass Wolter-I mirror segments. (A continuous ground electrode is first applied to the back surface). A pattern of independently addressable platinum (Pt) electrodes is deposited on top of the PZT layer forming individual piezo cells. Applying a low (< 10 V) DC voltage between a cell's top electrode and the ground electrode creates an electric field that produces a local strain in the piezo material parallel to the mirror surface. This strain causes localized bending in the mirror, called an influence function. By supplying an optimally chosen voltage to each of the individual cells, one can change the amplitude of each influence function to minimize figure errors in the mirror, thereby improving imaging performance. This allows us to correct mirror figure errors from fabrication, distortions introduced during mounting, along with any gravity release errors. Figure correction is made once on the ground during a calibration step post-mirror alignment and mounting. The ability to adjust and correct the figure of thin mirror segments increases their performance from a 10-arcsec resolution level to 0.5 arcsec. We have shown through simulations improvements from ~7 arcsec half-power diameter (HPD) to < 0.5 arcsec HPD using exemplar mirror figure data and modeled influence functions [2]). Corrections with adjustable mirrors are limited in spatial error bandwidth to those frequencies smaller than approximately the inverse of twice the adjuster size. Given adjuster sizes of ~5 mm, this limits corrections to errors with periods longer than 10 mm (or frequencies < 0.1 cycles/mm).

Differential deposition is an optical coating technology that functions as the inverse of computer-controlled polishing. Rather than a computer-controlled figuring lap that locally removes mirror material at high points on the surface, a metal (such as nickel) is computer-controlled sputtered locally onto the mirror surface so as to fill in the valleys in the mirror surface, resulting in an improvement in mirror figure and performance. While not physically limited to avoid correcting low spatial frequency errors, the fact that low frequency errors have significantly larger amplitudes does result in a practical low frequency bandwidth limit to differential deposition. This is because the

larger-amplitude low-frequency errors would require long sputtering times to deposit sufficiently thick material to correct the figure, making the process inefficient. In addition, as thin-film induced deformations scale with the product of film stress and film thickness, increasing the thickness makes the correction more likely to produce deformations, resulting in decreased figure correction convergence. Thus, for practical reasons, differential deposition is better limited to a mid-frequency bandwidth of errors that does not require thick coatings.

We seek to combine these two technologies because they seem to be natural partners in terms of correcting a broader mirror-figure-error bandwidth: adjustable optics for low-spatial-frequency errors, and differential deposition for mid-spatial-frequency errors. In the hybrid mirror approach, the thin film piezoelectric adjusters are applied on the back surface of the mirror, and the differential deposition film is applied on the front (X-ray-reflecting) side of the mirror. The purpose of this development is to coordinate the application of these two technologies to a conical mirror segment, extend their respective correction bandwidths such that they meet or even overlap in spatial error frequency space, thereby broadening the ability to make high-performance, lightweight, X-ray optics for Lynx.

Besides the adjustable optics and Lynx teams at SAO, significant contributors to the adjustable optics team are our colleagues at The Pennsylvania State University (PSU) Materials Research Institute. Dr. Susan Trolier-McKinstry at PSU, supported by Dr. Justin Walker, develops the PZT processes. Dr. Tom Jackson, supported by graduate students Tianning Liu and Mohit Tandulkar, develops the piezoelectric control processes. Differential deposition development is led by the Marshall Space Flight Center (MSFC) team of Dr. Brian Ramsey and Dr. Kiranmayee (Kiran) Kilaru, with the support of David Broadway of MSFC.

Project highlight:

Our most significant accomplishment over the past year is the demonstration of deterministic figure control on a cylindrical mirror segment to better (less) than 0.5 arcsec HPD effective performance with 1 keV X-rays. Measured figure correction via simultaneous control of 112 piezoelectric cells matched the simulated correction to ~0.46 arcsec HPD, a significant improvement over last year's ~1.2-arcsec performance. Significantly, we identified metrology noise as a problem last year, and this improvement was the result of reduction and filtering of that metrology noise.

Background

The development of large area sub-arcsec-resolution X-ray telescopes is not only consistent and relevant to NASA's strategic goals, but is virtually a requirement to successfully achieve NASA's Strategic Goal 1, "Expand the frontiers of knowledge, capability, and opportunity in space," [3] and in particular Objective 1.6 for Goal 1, "Discover how the Universe works, explore how it began and evolved…" [4] As described in 2013 NASA Astrophysics Roadmap "Enduring Quests Daring Visions," X-ray observations with several-square-meter area and 0.5-arcsec resolution are critical to understanding the structure, evolution, and energy flow within clusters of galaxies; to exploring fine features of filaments, knots, and jets associated with stellar and super-massive black holes; and to studying the early universe and the growth of structure. The Astrophysics Roadmap recommends an X-ray telescope with sub-arcsec imaging and several-square-meter area as necessary to achieve NASA's strategic goals [1]. That mission concept, X-ray Surveyor, is now the Lynx mission concept. Thin, lightweight sub-arcsec-resolution X-ray optics will provide us with the capability to advance our understanding of the early universe, energy feedback mechanisms, dark energy, and the

structure and evolution of objects ranging from among the largest and most massive to the most dense and energetic. Our proposed study will help lead to the development of the telescopes necessary to answer the NASA Astrophysics Science Questions "How does the universe work?" by responding to the goals to "Probe the origin and destiny of our universe, including the nature of black holes, dark energy, dark matter and gravity," and "Explore the origin and evolution of the galaxies, stars and planets…" [5].

To date, only the heavy, full-shell X-ray mirrors of Chandra have achieved 0.5 arcsec imaging. XMM-Newton's thin "electro-less" Ni shells are still too thick and heavy to achieve the Lynx collecting area requirements, and the XMM-Newton imaging resolution is 15 arcsec (although the mirror assemblies are ~ 10 arcsec). NuStar carries the best thin glass mirrors yet to fly, with ~1-arcmin imaging resolution. ESA's planned Athena mission, scheduled for launch in 2028, will employ silicon pore optic technology, but planned Athena resolution is only 5-arcsec HPD, ten times coarser than Lynx's requirement. The most advanced technology competing with adjustable optics is monocrystalline silicon optics being pursued by W. Zhang's team at NASA GSFC. They are at present making mirrors with several-arcsec HPD performance [6]. But their results as published are employing mirrors approximately twice as thick as consistent with their optical design and the mass budget – thus, they require development both in terms of absolute imaging performance, and achieving that performance with thinner, less stiff, mirrors. The GSFC group continues to develop their process, as does SAO. Our approach competes with the silicon mirror approach, and will surpass the electroplating replica and slumped glass approaches which cannot achieve sub-arcsec resolution.

Our approach mitigates critical risks to thin mirror performance: mounting-induced distortions of the mirror at assembly; epoxy shrinkage at mounting which also distorts thin mirrors; potential epoxy creep during the period between assembly and through launch; and distortions due to changes in the thermal environment on-orbit relative to the assembly and calibration environment. Only adjustable optics offers the possibility to correct these errors once introduced. Differential deposition enables the correction of higher spatial frequency errors than can be done with the thin-film adjusters. This error bandwidth is above that of the errors introduced due to the risks described above, and so complements the correctability afforded by the adjusters.

The development plan is to attempt to marry the differential deposition and adjustable optics technologies. At a top level, this will entail attempting to use differential deposition to correct mid-spatial frequency errors (10-mm to 1-mm axial periods) after the application of the piezoelectric film and associated electronics, and to explore the overlap in spatial frequency bandwidth between the two correction approaches.

Objectives and Milestones

At the top level, the objective of this program is to examine the feasibility of merging the two thin X-ray mirror technologies of thin film adjustable optics and differential deposition. At a slightly higher level of detail, this objective flows down to:

1. Improve low-frequency bandwidth correction with thin-film adjustable optics, and better define (figure) error correction as a function of error spatial frequency (or equivalently, better define the practical meaning of "low" spatial frequencies).

2. Determine realistic mid-spatial frequency correction bandwidths for differential deposition.

3. Combine, on a single mirror segment, both technologies of thin-film adjusters (on the back, or concave side) and differential deposition (on the front, convex side). Determine feasibility and usefulness of this approach in terms of the total mirror-figure-correction efficiency vs. frequency, and mirror performance pre- and post-correction.

Key project milestones and their status are described below.

- MSFC facilitization for differential deposition on segments – est. completion approx. 10/1/18 – This milestone was originally scheduled for Nov 2017 completion and has been delayed due to personnel shortages at MSFC resulting from (1) the untimely death from illness of one of our co-investigators, Misha Gubarev; (2) time required for MSFC to get approval to hire additional personnel; and (3) resource conflicts with both IXPE (an Explorer mission) and the NASA Lynx study;
- Reduction of mirror processing stresses – Complete 6/18;
- Stress compensation coatings development – est. completion 9/1/2018;
- Improve correction and better define bandwidth of thin-film adjusters – Complete 4/18;
- Develop process for physically combining both technologies on a single mirror segment – originally scheduled for 8/1/2018;
- Apply differential deposition on segments – est. facilitization completion 12/1/18, segment – est. completion 2/1/19 (originally scheduled 7/1/18, delay due to differential deposition facilitization delays);
- Determine combined technology correction efficiency and performance improvements – est. completion 5/1/2019; and
- Improve mirror segment mount design – This is a new, revised milestone resulting from our initial testing of the thin-film adjustable-optics technology. Our previous mirror mount – used to support the mirror during optical testing in a flight-like manner, was found to introduce large figure errors into the mounted mirror. These errors significantly complicate the determination of figure correction bandwidths and correction efficiency as a function of error spatial frequency. We felt it was necessary to improve the fidelity of the mounting process. Est. completion 9/1/2018.

Progress and Accomplishments

Significant progress has been made with respect to piezoelectric film processing stresses. In particular, we made several major advances. Piezoelectric processing stress – stresses introduced during the deposition and crystallization/annealing of the various thin films required – introduces distortions in the mirror. Uniform stress distortions should be cancelable via introduction of an equal stress on the opposite side of the mirror. Stress matching, or compensation, is not required to be perfect for adjustable optics (as it would need to be for non-adjustable optics) – it just is required to be good enough to fall within the adjustment range of the piezo actuators. In our switch from flat to cylindrical mirror segments we observed a change from uniform to non-uniform film stress, which was unexpected. First, we determined that a significant fraction ($\sim \frac{3}{4}$) of our stress non-uniformity was due to a coincident change in the methodology used to anneal the films. This change, from a box furnace to a rapid thermal annealer (RTA) was made to improve piezoelectric fabrication efficiency as the box furnace cycles took ~10 hours and the RTA cycles take ~5 min. Via experiments with flat mirrors we determined there was a failure in the RTA resulting in very non-uniform anneal temperatures. This is seen in Figs. 1a and 1b, which show measured figure change as a result of piezoelectric material deposition and then annealing in the RTA and box furnace, respectively. For a flat round disk, the expected change due to uniform film stress is a spherical deformation of the surface, producing a circularly uniform (i.e., purely radial) deformation. In Fig. 1a we see this expected spherical deformation due to the first two processing steps – deposition of the ground electrode and then the PZT. After annealing in the RTA, however, the figure change is decidedly non-circularly symmetric, indicating non-uniform film stress post-annealing. In Fig. 1b, we see the same three processing steps with a different sample, but this time using the box furnace to anneal. In this case, the film stress remains circularly symmetric, indicative of uniform stress. Subsequent temperature measurements in the RTA revealed the presence of large thermal gradients which are believed to have produced non-uniform annealing.
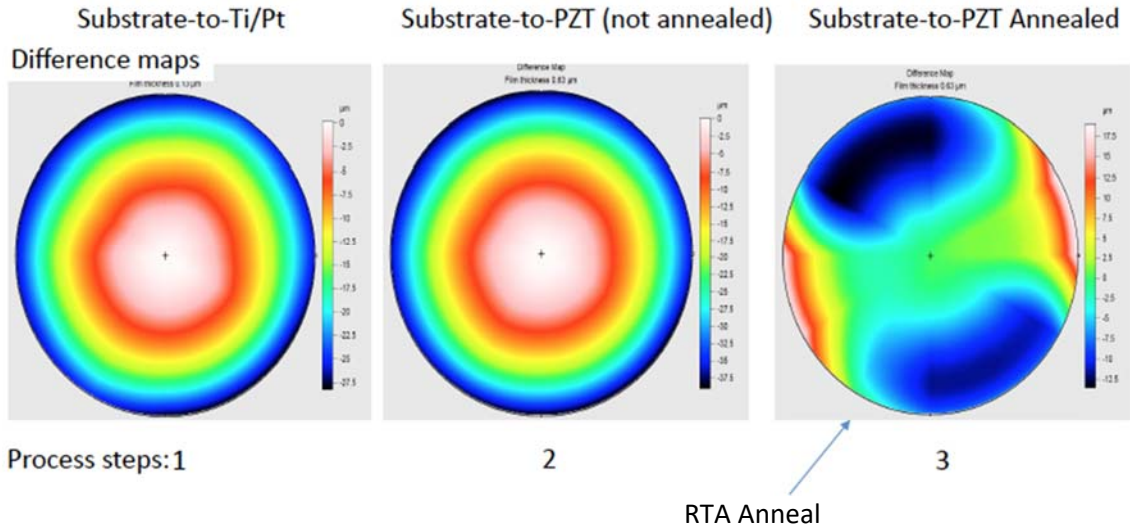
Fig. 1a. Figure change for three processing steps. Uniform stress results in the spherical figure changes seen in steps (1) and (2). The effect of non-uniform stress is evident in step (3) using the RTA.
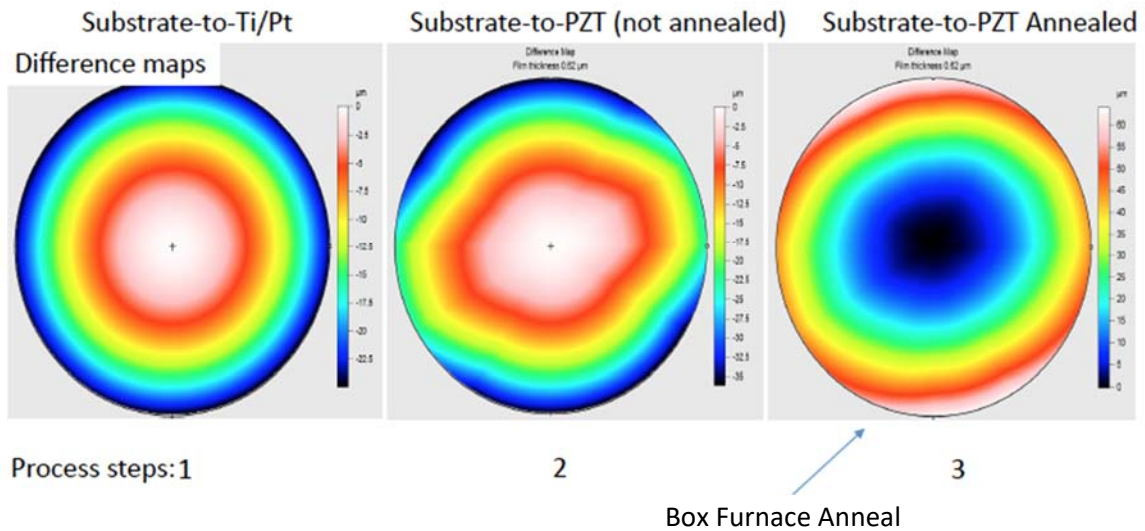
Fig. 1b. Figure change for three processing steps. Uniform stress results in the spherical figure changes seen in steps (1) and (2). The stresses remain essentially uniform in step (3) using the box furnace to anneal.

We subsequently made a cylindrical test mirror annealed in the box furnace and attempted to compensate for piezo stresses via a front-surface Cr/Ir film. In a cylindrical or conical mirror, the most sensitive parameter to film stress is the cylindrical radius of curvature. This is because the segment architecture results in significant increased axial stiffness relative to the azimuthal direction. Measurements of the cylindrical radius of curvature before piezoelectric processing, after annealing, and after applying the stress compensating film showed that we corrected the radius of curvature change back to nominal, to within our radius of curvature metrology error. This implied correcting the average piezoelectric stresses to within approximately 10% of the initial value. This 10% is also our target correction, as it gets us to the point where the residual stress-related distortions can be corrected by the piezoelectric adjusters during the figure-correction operation.

As part of this correction, though, we noticed still-higher-than-desired non-uniform stress-related deformations. We hypothesized that these deformations were due to uniform film stress in a film with non-uniform thickness. Using ellipsometry, film thicknesses (of both the piezoelectric film and the

stress compensating film) were measured, revealing an approximately systematic thickness variation of ~15% peak. The coating geometry was modeled and produced a predicted film-thickness-uniformity map, and excellent agreement was obtained between the modeled thickness variations and the measured thickness variations. This result is shown in Fig. 2. We thus ascribe thickness non-uniformity to coating geometry – too small a sputter target for the size substrate, and basically coating geometry for coating a flat mirror rather than a cylindrical mirror (with a long axial sputter source). Unfortunately, funding levels limit our ability to incorporate improvements here as a new, larger, sputter chamber is required, with an estimated cost of $500k to $1M. Finite element modeling was used to estimate the effects of both concave and convex surface-film-thickness non-uniformity to understand what limits, if any, this would place on our ability to achieve sub-arcsec mirror performance. We determined that if the films are applied with uniform stress but with modeled (or measured) thickness variation, the resulting compensated stress and deformation, before correction by the adjusters, can be reduced to a performance residual of ~0.1-arcsec image diameter.
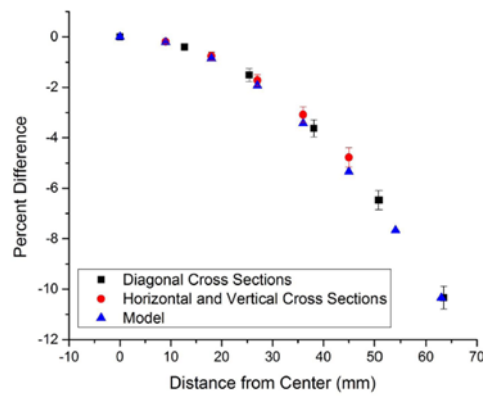
Fig. 2. Comparison of measured and modeled film thickness variation. Note the excellent agreement.

Significant progress was also made with respect to improving figure correction with the thin-film adjusters. We applied a figure change of ~0.8 μm peak-to-valley (P/V) to a cylindrical mirror via 112 simultaneously controlled thin-film piezoelectric adjusters. Because of the large mirror-mount distortion (described in the "Objectives and Milestones" section) and the large mirror deformations introduced by non-uniform stresses resulting from both PZT thickness variations due to coating geometry and thermal gradients during PZT annealing, we could not make an absolute correction to all the mirror figure error. However, we were able to make a relative figure change to "correct" for the post-thermal forming figure error of the mirror segment. We measured the commanded change in mirror figure and compared that to the desired figure change. That difference is the limit to which we could correct mirror figure. Last year, we applied a figure change – a figure correction – that had an equivalent X-ray performance (single reflection, 1 keV) of ~7 arcsec HPD. Our measured performance – based on optical metrology before and after applying the figure change to the mirror – matched the desired change to ~1.2 arcsec HPD. In addition, our prediction of the measured change – a simulation of what we expected to achieve – resulted in a match to the desired change of ~1.3 arcsec HPD [7]. The agreement between the prediction and the measurement tells us the system is behaving deterministically.

Based on our test results, we hypothesized that performance was being limited by the effects of metrology noise. Influence functions (I/Fs) – the change in mirror shape in response to energizing a particular piezoelectric cell – are obtained experimentally during calibration. The I/Fs thus are affected by metrology noise. Each I/F, though mostly quite localized to the extent of the piezo cell, is still measured over the entire mirror surface, and there are low-amplitude broad wings to the I/F. The entire I/F for each piezo cell is used in optimizing the mirror correction, thus the noise from all the adjuster calibrations adds randomly over the surface, degrading the accuracy of the solution. We first tested this hypothesis by trying a simulated solution using noise-free I/Fs obtained from finite element modeling. Use of those I/Fs

gave a simulated correction accurate to ~0.3 arcsec HPD (we don't use modeled I/Fs at this point in time due to potential differences between the model and reality – effects of mirror bonds, registration of the modeled cells to the real cells on the mirror, etc.). With the apparent success of the simulation, we explored several approaches to low-pass filtering of the I/Fs to reduce metrology noise – the best approaches using filters that basically do minimal filtering near the I/F peak where signal to noise is greatest and the I/F has high frequency content we don't want to remove, and do their maximum filtering on the I/F wings where signal to noise is lowest and any high frequency content is just noise. We repeated the same test as before but with filtered influence functions, on the same adjustable mirror making the same correction, and found we were able to improve the correction accuracy to ~ 0.54 arcsec HPD (as-measured) from ~ 1.2 arcsec HPD (as measured in the prior experiment). This result is shown in Fig. 3.
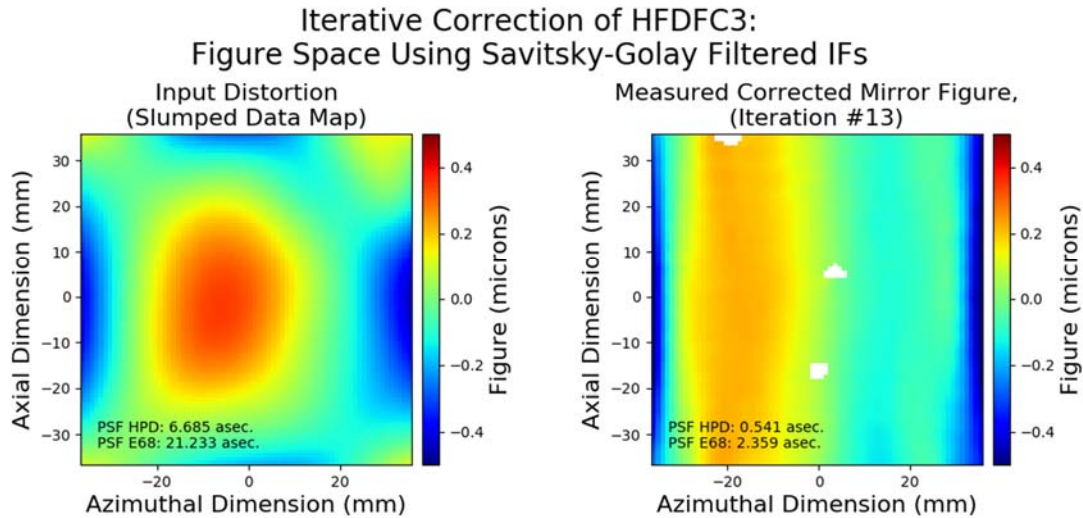
Fig. 3. Deterministic control of mirror figure by simultaneous application of 112 piezoelectric cells on a cylindrical test mirror. On the left is the input distortion map representing the post-thermal-forming figure error of the mirror segment. The best-fit conic has been removed from the data, leaving only the radial displacement figure error. On the right is the correction residual, as measured optically using our wavefront sensor. Correction accuracy, including the contribution of 0.29 arcsec HPD of diffraction, is 0.54 arcsec HPD. Note the apparent "large" azimuthal figure error – low at the left- and right-hand edges with hill running vertically at azimuth about -20 mm and a small valley on the left at azimuthal coordinate of about +15 mm. These features are included in the performance estimate, and are a result of the greatly reduced sensitivity of grazing incidence performance to figure errors in the azimuthal direction. Our optimizer is set up to take advantage of this, resulting in solutions that are very smooth axially (up and down in the figure), and more tolerant of errors in the azimuthal direction (left-right).

In addition, because of how the effective performance is calculated as equivalent X-ray performance, the computation automatically includes the effects of diffraction in the result. A perfect correction would result in a post-correction performance of 0.29-arcsec HPD, that residual being due entirely to diffraction. When we account for diffraction, the accuracy of our correction improves to ~0.46-arcsec HPD (single reflection, 1 keV). This accuracy is still about a factor of two higher than where it needs to be to enable us to meet Lynx requirements (assuming the pre-adjustment mirror performance is within the actuators' range of correction). But we still have metrology noise on the I/Fs, as evidenced by the 0.3-arcsec-HPD residual from the simulation with completely noise-free simulated I/Fs. Clearly, there is room for more work to be done here, in terms of filtering of the I/Fs, reducing metrology noise, and possibly modifying the optimization algorithm to "discount" the influence of distant piezo cells. In addition, development is required to modify the PZT deposition geometry and the PZT annealing. Unfortunately, modifying coating geometry via a new chamber is expensive we continue to try to improve anneal oven thermal uniformity, which is time consuming." We will continue this investigation.

As mentioned in the "Milestones" section, we determined our methodology for mounting the mirror in a flight-like way was seriously flawed, introducing large distortions in a single process step [7]. Difficulties in this step – bonding flexures that support the mirror on its axial ends to a housing – led us to abandon that approach as too difficult/technically risky. An alternative design is being developed, in which the mirror is supported on its azimuthal sides. This offers several potential advantages, including being more likely to introduce distortions in the less-sensitive azimuthal direction, and potentially obstructing less of the mirror aperture. A photograph of a test mirror (a non-adjustable conical mirror with a thin gold coating for metrology purposes) being test-fit is shown in Fig. 4. We hope to have initial results from this mounting approach in late summer. Development of this mount is necessary for a number of reasons. Obviously, any mirror system requires a mount. An adequately stiff mount is important to determining the high-frequency bandwidth limit of mirror figure correction efficiency. Reducing the mirror figure error (by eliminating mounting-induced distortions) will enable us to use higher-accuracy, lower-noise metrology – interferometry – for testing, rather than wavefront sensing.

Fig. 4. Fit-check of test conical segment in new mount.

Path Forward

Moving forward, the major remaining activities will be the development of the mirror mount, facilitation for differential deposition on mirror segments, and fabrication and optical test of a hybrid mirror segment.

References

[1] "*Enduring Quests, Daring Visions*," NASA Astrophysics Roadmap (2013)
[2] T. Aldcroft et al., "*Simulating correction of adjustable optics for an X-ray telescope*," SPIE Proc. **8503**, 85030F (2012)
[3] "*2014 NASA Strategic Plan*," NP-2014-01-964-HQ, p. 7 (2014)
[4] op. cit., p. 21
[5] "*2014 NASA Science Plan*," p. 74 (2014)
[6] R.E. Riveros et al., "*Progress on the fabrication of lightweight single-crystal silicon X-ray mirrors*," SPIE Proc. **10399** 103990T (2017)
[7] C. DeRoo et al., J. Astronomical Telescopes Instruments Systems, "*Deterministic figure correction of piezoelectrically adjustable slumped glass optics*," **4** (1) 019004 (2018)

For additional information, contact Paul B. Reid: *preid@cfa.harvard.edu*

Development of a Critical-Angle Transmission Grating Spectrometer

Prepared by: Ralf K. Heilmann (MIT Kavli Institute, MKI), Alex R. Bruccoleri (Izentis, LLC), and Mark L. Schattenburg (PI, MKI)

Summary

Critical-Angle Transmission (CAT) gratings combine the advantages of traditional phase-shifting transmission gratings – e.g., relaxed alignment and figure tolerances, low mass, and transparency at high energies; with the advantages of blazed reflection gratings – e.g., high diffraction efficiency and high resolving power due to utilization of higher diffraction orders. In combination with grazing-incidence X-ray mirrors and CCD detectors, they promise a five- to 10-fold increase in efficiency and a three- to 10-fold improvement in resolving power over existing X-ray grating spectrographs [1]. Development of CAT-grating fabrication technology has been supported by NASA under the Strategic Astrophysics Technology (SAT) program since January 2012.

Under a previous award, we achieved three major breakthroughs: the fabrication of several CAT gratings with record absolute diffraction efficiency, > 30%; the extension of the CAT-grating bandpass through metal-coating the silicon grating bars; and experimental demonstration of a CAT-grating spectrometer with a spectral resolving power $R = \lambda/\Delta\lambda > 10,000$, exceeding requirements for all currently posed mission concepts [2]. As a result, CAT-grating technology has been vetted at Technology Readiness Level (TRL) 4 in June of 2016. Due to our progress, CAT gratings were selected as an enabling technology for the Arcus Grating Spectrometer Explorer mission proposal led by the Smithsonian Astrophysical Observatory (SAO)[3]. We successfully performed environmental testing on frame-mounted gratings, and scaled up grating size by a factor of three. Subsequently, Arcus was one of three proposals selected for a Phase A concept study.

We are in the second year of our current award. In the first year, we developed an improved laser-based alignment technique for multiple gratings. X-ray tests with simultaneous illumination of two large gratings confirmed alignment within goal tolerances. In the second year, we extended alignment to an array of four large gratings. Simultaneous X-ray illumination of the array with two co-aligned mirror modules produced a source spectrum with R > 3,500. In collaboration with SAO, we have developed an alignment and bonding station for the production of Arcus flight-like grating facets [4]. Our CAT grating spectrometer ray-tracing models have been refined and provide a solid basis for mission design and performance predictions [5].

> **Project Highlights:**
>
> - Demonstrated R > 3500 with X rays for an array of four co-aligned large gratings.
> - Developed an alignment and bonding station for fabrication of flight-like grating facets.

Background

Absorption- and emission-line spectroscopy, with the performance made possible by a well-designed CAT X-ray grating spectrometer (CATXGS), will target science objectives concerning the large-scale structure of the universe, cosmic feedback, interstellar and intergalactic media, and stellar accretion. A CATXGS-carrying mission can address the kinematics of galactic outflows, hot gas in galactic halos, black-hole growth, the missing baryons in galaxies and the Warm-Hot Intergalactic Medium, and the

effect of X-ray radiation on protoplanetary disks. All of these are high-priority International X-ray Observatory (IXO) science questions described in the 2010 Decadal Survey, "*New Worlds, New Horizons in Astronomy and Astrophysics*" (NWNH) [6], and are addressed further in the NASA "*X-ray Mission Concepts Study Report*" [7]. A number of mission concepts submitted in response to NASA Request for Information (RFI) NNH11ZDA018L could be enabled by a CATXGS [7, 8]. Lynx (formerly known as X-ray Surveyor)[9], a mission described in the 2013 "*Enduring Quests, Daring Visions*" Astrophysics Roadmap [10], is on a short list of strategic mission concepts being studied in preparation for the 2020 Decadal Survey [11]. A core instrument for Lynx would be a soft-X-ray grating spectrometer with R > 5,000 and effective area A_{eff} > 4,000 cm^2, achieved with a mirror effective area of about 2 m^2 at 0.6 keV and a mirror Point-Spread-Function (PSF) of 0.5 arcsec. These ambitious requirements go beyond previous performance goals assumed for a Probe-class mission and require detailed ray-trace studies and a reevaluation of our technology development roadmap.

The soft-X-ray band contains many important diagnostic lines (C, N, O, Ne, and Fe ions). Imaging spectroscopy with spectral resolution better than 2 eV has been demonstrated with small transition-edge-sensor-based microcalorimeter arrays, providing resolving power over 3000 above 6 keV. However, toward longer wavelengths, energy-dispersive detectors cannot provide the spectral resolution required to address several important NWNH high-priority science objectives. The only known technology providing high spectral-resolving power in this band is wavelength-dispersive, diffraction-grating-based spectroscopy.

The technology currently used in orbit for grating-based soft-X-ray spectroscopy was developed in the 1980s. The Chandra High-Energy Transmission-Grating Spectrometer (HETGS) carries polyimide-supported gold gratings with no more than 10% diffraction efficiency in the 1-5-nm band, but the whole moveable grating array only weighs about 10 kg. The X-ray Multi-mirror Mission – Newton (XMM-Newton) Reflection Grating Spectrometer (RGS) has more efficient grazing-incidence reflection gratings, but its mass is high (> 100 kg) and it has low spectral-resolving power (~300). CAT gratings combine the advantages of the HETGS and RGS gratings, and promise higher diffraction efficiency over a broad band, with a resolving power greater than 3000 for a 10-arcsec PSF telescope, and greater than 10,000 for a 0.5-arcsec-PSF telescope. These gratings also offer near-ideal synergy with a calorimeter-based imager, since CAT gratings become increasingly transparent at higher energies. Thus, high-resolution spectroscopy could be performed with a CATXGS in tandem with a calorimeter over the range of ~0.2 to tens of keV on a larger mission such as Lynx. Figures-of-merit for many types of observations, such as the accuracy of line-centroid measurement in absorption-line spectroscopy, could be improved by more than an order of magnitude over Chandra and XMM-Newton. The new, patented CAT-grating design relies on the reflection (blazing) of X-rays from the sidewalls of free-standing, ultra-high-aspect-ratio, sub-micron-period grating bars at grazing angles below the critical angle for total external reflection. Fabrication combines advanced novel methods and tools from the semiconductor and Micro-Electro-Mechanical Systems (MEMS) industries with patterning and fabrication methods developed at MIT over several decades.

We plan to bring CAT-grating technology to TRL 5 by 2021 to reduce technology risk and cost for a CATXGS that can meet Lynx requirements before the mission enters Phase A. We therefore want to demonstrate efficient, large-area (~ 50 mm × 50 mm) CAT-grating facets with minimal blockage from support structures. Facets will be mounted onto thin and stiff frames, which can then be assembled into grating arrays sized on the order of 1 m^2.

Objectives and Milestones

The objective of this project is to demonstrate an aligned array of large-area, high-efficiency CAT gratings with minimal support-structure blockage, providing resolution higher than 5000 in the soft-X-ray band, and maintaining its performance after appropriate vibration, shock, and thermal testing.

The array will consist of so-called grating facets mounted to a Grating-Array Structure (GAS). Facets are comprised of a grating membrane, etched from a silicon-on-insulator (SOI) wafer, and a facet frame that holds the membrane. The increasing performance requirements for the gratings lead to more demanding precision and repeatability in grating fabrication. At the same time, large arrays require more gratings than can be reasonably produced with our one-grating-at-a-time "beaker and tweezer" approach. It is therefore essential that we begin to transfer our key process steps to a more precise and repeatable tool set that is also conducive to volume production on the order of 1,000 gratings.

Key project milestones:

1. Develop silicon lattice-independent anisotropic etch capable of achieving the required aspect ratios for 200-nm-period gratings (Deep Reactive Ion Etch, DRIE, with a University of Michigan tool, completed in 2011).

2. Develop process for free-standing, large-area gratings with hierarchy of low-blockage supports (completed in 2012).

3. Combine (completed in 2013) and optimize (ongoing) dry- and wet-etch processes to obtain smooth grating-bar sidewalls; produce free-standing, large-area gratings with hierarchy of low-blockage supports (demonstrated, yield improvements ongoing); and test X-ray efficiency (ongoing).

4. Select, acquire, install, and test advanced DRIE tool at MIT (completed in 2014).

5. Demonstrate CAT-grating resolving power in an X-ray imaging system (completed in 2016); repeat with more than one grating (completed in 2017) or small array (completed in 2018).

6. Develop grating facet/frame design, process for integration of CAT grating membrane and frame, and alignment of facets on a breadboard GAS (ongoing, first prototype facet completed).

7. Optimize/reduce footprint of support structures and produce deeper gratings (ongoing).

8. Produce high-fidelity ray-trace model for an optimized Lynx CATXGS (2019).

9. Transfer front- and back-side patterning steps to industrial-scale tools (2019/2020).

10. Environmental and X-ray tests (using large-area, high angular-resolution optics) of aligned array of grating facets mounted to GAS (2020/2021).

Progress and Accomplishments

The key challenges in the fabrication of CAT gratings lie in their structure – small grating period (200 nm), small grating duty cycle (~40-nm-wide grating bars with 160-nm spaces between), and large depth (4-6 µm) result in ultra-high aspect ratios (100-150), with nm-smooth sidewalls. In addition, the gratings should be freestanding rather than supported by a membrane. Structures with such an extreme combination of geometrical parameters, or anything similar, have never been made before.

Prior to SAT support, we fabricated small KOH-wet-etched CAT-grating prototypes that met all these requirements, and measured their efficiency at a synchrotron source, demonstrating good agreement with theoretical predictions [12, 13]. Due to their extreme dimensions and the requirement to be freestanding, CAT gratings must be supported by slightly "bulkier" structures. We use a so-called L1 cross-support mesh (period ~5-20 µm), integrated into the SOI device layer, and etched at the same time as the CAT gratings. Unfortunately, the wet-etch that provides the nm-smooth CAT grating sidewalls leads to widening L1 supports with trapezoidal cross sections and unacceptable X-ray blockage.

DRIE is an alternate process that can provide the required etch anisotropy for CAT grating bars and L1 supports simultaneously. To make large-area, freestanding gratings, we also use this process to

fabricate a high-throughput hexagonal Level 2 (L2) mesh, etched out of the much thicker (~0.5 mm) SOI handle layer (Fig. 1). We developed a process that allows us to DRIE the CAT grating bars and the L1 supports out of the thin SOI device layer (front-side), stopping on the buried-oxide (BOX) layer; and to subsequently etch the L2 mesh with a high-power DRIE into the back-side, again stopping on the BOX layer. The BOX layer is removed with a hydrofluoric acid etch, and the whole structure is critical-point-dried in liquid CO_2. We fabricated several 31 mm × 31 mm samples with acceptable yield [14].
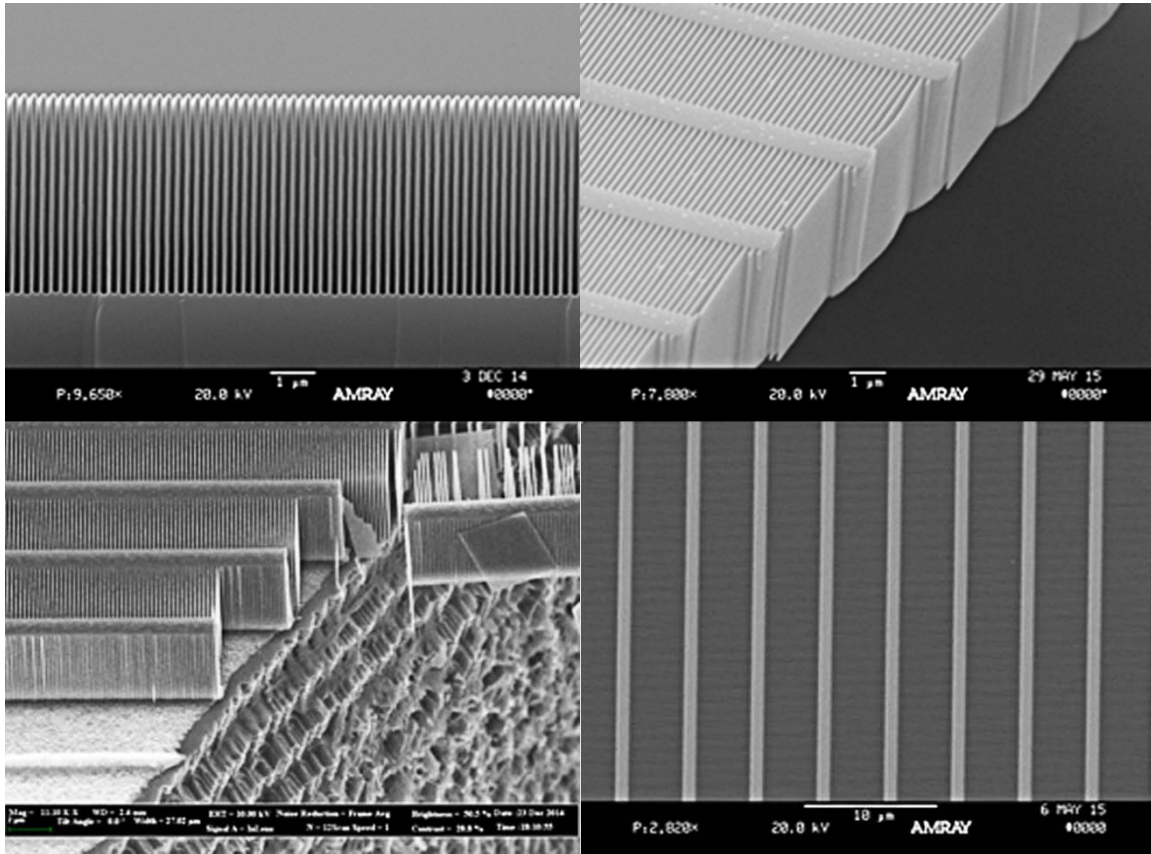
Fig. 1. Top left: *Cross-sectional scanning electron micrographs (SEMs) of CAT-grating DRIE, showing a high-quality, straight grating-bar profile before KOH etch.* Top right: *Cleaved free-standing CAT-grating membrane.* Bottom left: *Detail of cleaved CAT-grating membrane where back-side (very rough L2 mesh sidewalls from back-side DRIE) and front-side (much finer L1 and CAT grating structures) etches meet at the BOX layer.* Bottom right: *Top view of free-standing CAT-grating membrane, showing defect-free CAT grating bars suspended between L1 support mesh bars.*

Unfortunately, DRIE leaves the sidewalls of etched structures with several nm of roughness, detrimental to CAT grating efficiency. In 2012-2013, we developed a combined DRIE/KOH approach on bulk silicon that follows DRIE with a relatively short KOH "polishing" step that reduces sidewall roughness and straightens and thins the grating bar profile [15]. In 2014, we transferred and modified our new process to be compatible with the more delicate double-sided processing on SOI wafers for large-area, freestanding gratings (Fig. 1).

During 2014-2015, our process development accelerated significantly, thanks to a newly acquired dedicated DRIE tool in our lab at MIT, funded through a previous SAT award. We greatly improved DRIE grating-bar profile control, and we now routinely achieve constant-thickness or slightly retrograde bar profiles (Fig. 1). These improved grating bars survive vastly longer wet-etch (sidewall polishing) times in concentrated KOH, presumably leading to smoother sidewalls and thus higher reflectivity and

diffraction efficiency. In 2015, we produced several ~ 10 mm $\times 30$ mm gratings with very similar record-high X-ray performance, a tribute to our improved and matured fabrication process [2, 16-18].

The resolving power of an X-ray-objective transmission-grating spectrometer is usually limited by the optical design, the focusing optics PSF, and the angle of diffraction, but not by the alignment-insensitive transmission gratings. To verify the last point, in 2016 we performed a measurement of resolving power at the NASA MSFC Stray Light Facility (SLF), using the Al K$\alpha_{1,2}$ lines from an electron bombardment source, and a segmented slumped-glass mirror pair from the Zhang X-ray optics group at NASA/GSFC as the focusing optic. In order to resolve the line shape of the Al K$\alpha_{1,2}$ pair, we coated a 32-mm-wide CAT grating with a thin layer of platinum, using Atomic Layer Deposition (ALD). The metal coating increased the critical angle and allowed us to measure the Al K$\alpha_{1,2}$ line shape in 18th order, where the lines are much broader than the optic PSF. Data analysis demonstrated that our CAT gratings are compatible with a resolving power significantly in excess of R = 10,000. Thus, CAT gratings will not degrade the resolving power of spectrometers designed for R on the order of 5000, such as a CATXGS for Lynx [2].

Furthermore, the demonstrated ability to conformal-coat the ultra-high-aspect-ratio CAT grating bars with high-electron-density materials using ALD opens up a new design space for CAT gratings, extending their utility to shorter wavelengths and/or larger blaze angles and thus higher spectrometer resolving power.

At the start of our current grant, we measured the resolving power of an uncoated CAT grating, bonded to a frame and illuminated by an SPO at the SLF, and found R = 3000 in 9th order (Al K$_\alpha$), which was limited by the optic/source PSF and not by the grating. This performance exceeds the requirements of the proposed Arcus Explorer mission [3]. The frame-mounted grating was measured again after vibration testing and thermal cycling and showed no degradation in resolving power or diffraction efficiency. As a result, CAT gratings in combination with SPOs were chosen as the core technologies for the Arcus Explorer proposal submitted in December 2016. We have since made important breakthroughs in the grating filling and chip-bonding steps that enabled us to fabricate six significantly larger gratings (~ 32 mm $\times 32$ mm), with narrower L1 supports and slightly improved efficiency compared to our previous record. As a first step towards a larger grating array, we have aligned two of these large, frame-mounted gratings to each other in the roll degree of freedom, which has the most stringent requirements, using an improved ultraviolet (UV) laser alignment technique in air. Illuminating both aligned gratings simultaneously with a single SPO at the Panter X-ray facility in Germany, we confirmed that we exceeded our alignment requirements [19].

In the past year, we performed UV alignment of an array of four large gratings, and X-ray tested them under illumination by a co-aligned pair of SPO units, demonstrating R > 3500 (Figs. 2 and 3). In collaboration with SAO, we integrated our scanning laser reflection alignment tool into a facet alignment and bonding station (FABS) and produced a first flight-like Arcus grating facet (Fig. 4) [4]. We also improved the fidelity of our ray-tracing tools that guide the creation of realistic alignment error budgets [5]. Using small-angle X-ray scattering we discovered that our older-generation DRIE tool creates a narrow, but systematic distribution of grating bar angles relative to the surface normal, which is a known effect for all but the newest tools. We developed metrology that can quickly characterize this distribution for each grating [20]. The result is used to align grating membrane and facet in optimal fashion in the FABS before bonding. This effect is benign for Arcus but may be a complication for larger gratings for Lynx. With the help of the group under Herman Marshall (MIT), we developed an in-house capability to measure grating X-ray diffraction efficiency, using the former Chandra X-ray grating evaluation facility. This resource allows for more frequent characterization between trips to a synchrotron.
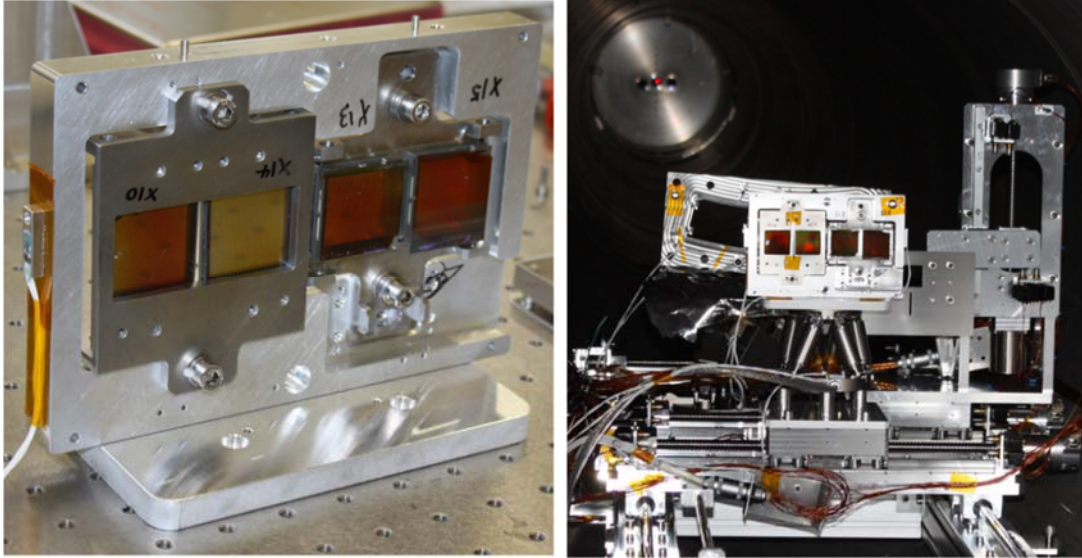
Fig. 2. Left: *Grating petal holding four co-aligned 32 mm x 32 mm CAT gratings.* Right: *Setup at the PANTER X-ray facility. All four gratings are illuminated simultaneously via a pair of silicon pore optic (SPO) units (not visible, behind the gratings).*
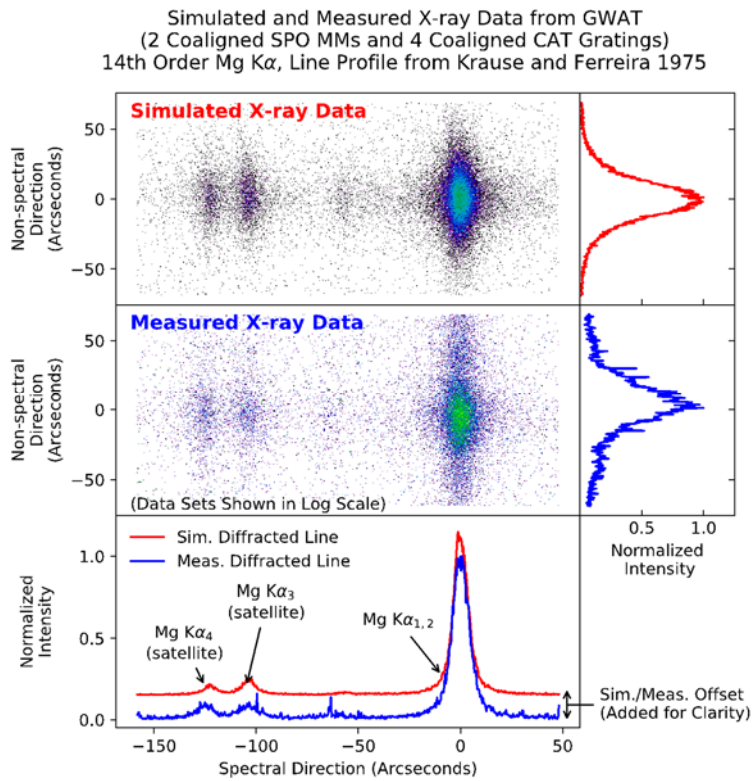
Fig. 3. *Measured Mg Kα₁,₂ spectrum in 14th order from four co-aligned gratings. Top is a ray-trace model of the experimental setup, below is the measured X-ray data. Bottom shows both data sets projected onto the dispersion axis. (Image credit: C. deRoo, SAO).*

Fig. 4. *Arcus flight-like grating window for four gratings. On the left is a flight-like CAT grating facet (grating membrane bonded to flexure frame). In the back are two facet dummies. (Image credit: E. Hertz, SAO).*

Path Forward

While the case could be made that CAT grating technology is at or near TRL 5 for Arcus with TRL 6 in the near future, the same cannot be said for Lynx. For a given telescope aperture, there is a tradeoff between grating array size (or effective area), individual facet size, and resolving power, which also depends on the detailed makeup of the telescope PSF. We will perform ray-tracing studies to understand these tradeoffs in greater detail, but we already know that for Lynx gratings need to be made larger to keep the grating count reasonable, they need to be etched deeper with thinner grating bars for higher efficiency, support structures need to be thinner for increased throughput, and some gratings may need to be coated with thin metal films.

For the six months remaining under our current grant we plan the following activities:

1. Develop CAT-grating DRIE process on a state-of-the-art tool (available at neighboring Harvard University) and evaluate grating bar angle distribution.
2. Produce CAT gratings with narrower L1 supports for characterization and future tests.
3. Investigate projection lithography and etch tools at the MIT Lincoln Lab (MIT/LL) Microfabrication Foundry for usefulness in automated, high-precision patterning for CAT grating fabrication.
4. Acquire and install HF vapor etch tool.

Beyond our current grant, and assuming new SAT funding, we hope to work on the following tasks, starting in 2019:

1. Work with MIT/LL to develop high-quality etch mask patterns for deeper gratings with narrower support structures.
2. Develop grating bar thinning process using oxidation and vapor HF etch.
3. Characterize resulting gratings (diffraction efficiency, resolving power, environmental tests).
4. Perform ray-trace studies for a Lynx CATXGS to better understand design tradeoffs.

References

[1] R.K. Heilmann, J.E. Davis, D. Dewey, M.W. Bautz, R. Foster, A. Bruccoleri, P. Mukherjee, D. Robinson, D.P. Huenemoerder, H.L. Marshall, M.L. Schattenburg, N.S. Schulz, L.J. Guo, A.F. Kaplan, and R.B. Schweickart, "*Critical-Angle Transmission Grating Spectrometer for High-Resolution Soft X-Ray Spectroscopy on the International X-Ray Observatory*," Space Telescopes and Instrumentation 2010: Ultraviolet to Gamma Ray, M. Arnaud, S.S. Murray, T. Takahashi (eds.), Proc. SPIE, **7732**, 77321J (2010)
[2] R.K. Heilmann, A.R. Bruccoleri, J. Kolodziejczak, J.A. Gaskin, S.L. O'Dell, R. Bhatia, and M.L. Schattenburg, "*Critical-Angle X-ray Transmission Grating Spectrometer with Extended Bandpass and Resolving Power > 10,000*," Space Telescopes and Instrumentation 2016: Ultraviolet to Gamma Ray, Proc. SPIE, **9905**, 99051X (2016)

[3]   R.K. Smith et al., "*Arcus: Exploring the Formation and Evolution of Clusters, Galaxies, and Stars*," UV, X-Ray, and Gamma-Ray Space Instrumentation for Astronomy XX, Proc. SPIE, **10397**, 103970Q (2017)

[4]   R. K. Heilmann et al., "*Blazed transmission grating technology development for the Arcus x-ray spectrometer explorer*," submitted to Proc. SPIE **10699**

[5]   H. M. Günther et al., *"Performance of a Double Tilted-Rowland-Spectrometer on Arcus,"* UV, X-Ray, and Gamma-Ray Space Instrumentation for Astronomy XX, Proc. SPIE, **10397**, 103970P (2017)

[6]   Blandford et al., "*New Worlds, New Horizons in Astronomy and Astrophysics*," National Academy of Sciences (2010)

[7]   R. Petre et al., "*The NASA X-ray Mission concepts study*," Space Telescopes and Instrumentation 2012: Ultraviolet to Gamma Ray; Proc. SPIE **8443**, 84431I (2012)

[8]   M.W. Bautz, W.C. Cash, J.E. Davis, R.K. Heilmann, D.P. Huenemoerder, M.L. Schattenburg, R. McEntaffer, R. Smith, S.J. Wolk, W.W. Zhang, S.P. Jordan, and C.F. Lillie, "*Concepts for High-Performance Soft X-Ray Grating Spectroscopy in a Moderate-Scale Mission*," Space Telescopes and Instrumentation 2012: Ultraviolet to Gamma Ray, T. Takahashi, S.S. Murray, and J.-W. A. den Herder (eds.), Proc. SPIE, **8443**, 844315 (2012)

[9]   J. Gaskin et al., *"Lynx Observatory and Mission Concept Status,"* UV, X-Ray, and Gamma-Ray Space Instrumentation for Astronomy XX, Proc. SPIE **10397**, 103970S (2017)

[10]   "*Enduring Quests, Daring Visions*," Astrophysics Roadmap (2013)

[11]   P. Hertz, "*Planning for the 2020 Decadal Survey: An Astrophysics Division White Paper*" (2015)

[12]   R.K. Heilmann, M. Ahn, E.M. Gullikson, and M.L. Schattenburg, "*Blazed High-Efficiency X-Ray Diffraction via Transmission through Arrays of Nanometer-Scale Mirrors*," Opt. Express, **16**, 8658 (2008)

[13]   R.K. Heilmann, M. Ahn, A. Bruccoleri, C.-H. Chang, E.M. Gullikson, P. Mukherjee, and M.L. Schattenburg, "*Diffraction Efficiency of 200 nm Period Critical-Angle Transmission Gratings in the Soft X-Ray and Extreme Ultraviolet Wavelength Bands*," Appl. Opt., **50**, 1364-1373 (2011)

[14]   A. Bruccoleri, P. Mukherjee, R.K. Heilmann, J. Yam, M.L. Schattenburg, and F. DiPiazza, "*Fabrication of Nanoscale, High Throughput, High Aspect Ratio Freestanding Gratings*," J. Vac. Sci. Technol. B, **30**, 06FF03 (2012)

[15]   A.R. Bruccoleri, D. Guan, P. Mukherjee, R.K. Heilmann, and M.L. Schattenburg, "*Potassium Hydroxide Polishing of Nanoscale Deep Reactive-Ion Etched Ultrahigh Aspect Ratio Gratings*," J. Vac. Sci. Technol. B, **31**, 06FF02 (2013)

[16]   R.K. Heilmann, A.R. Bruccoleri, D. Guan, and M.L. Schattenburg, "*Fabrication of Large-Area and Low Mass Critical-Angle X-ray Transmission Gratings*," Proc. SPIE, **9144**, Space Telescopes and Instrumentation 2014: Ultraviolet to Gamma Ray, 91441A (2014)

[17]   R.K. Heilmann, A.R. Bruccoleri, and M.L. Schattenburg, "*High-Efficiency Blazed Transmission Gratings for High-Resolution Soft X-ray Spectroscopy*," Proc. SPIE, **9603**, Optics for EUV, X-Ray, and Gamma-Ray Astronomy VII, 960314 (2015)

[18]   A.R. Bruccoleri, R.K. Heilmann, and M.L. Schattenburg, "*Fabrication Process for 200 nm-Pitch Polished Freestanding Ultra-High Aspect-Ratio Gratings*," J. Vac. Soc. Technol. B **34**, 06KD02 (2016)

[19]   R. K. Heilmann et al., *"Critical-Angle Transmission Grating Technology Development for High Resolving Power Soft X-ray Spectrometers on Arcus and Lynx*," Optics for EUV, X-Ray, and Gamma-Ray Astronomy VIII, Proc. SPIE **10399**, 1039914 (2017)

[20]   J. Song et al., *"Metrology for quality control and alignment of CAT grating spectrometers,"* submitted to Proc. SPIE **10699**

For additional information, contact Mark L. Schattenburg: *marks@space.mit.edu*

Next-Generation X-ray Optics: High Angular Resolution, High Throughput, and Low Cost

Prepared by: William W. Zhang (PI; NASA/GSFC)

Summary

This work continues technology development of X-ray optics for astronomy. Since Fiscal Year (FY) 2012, the Strategic Astrophysics Technology (SAT) program has funded this effort, which the Constellation-X project initiated and the International X-ray Observatory (IXO) project continued.

The objective is to advance astronomical X-ray optics by at least an order of magnitude in one or more of three key metrics from the state of the art represented by the four major X-ray missions: Chandra, X-ray Multi-mirror Mission-Newton (XMM-Newton), Suzaku, and Nuclear Spectroscopic Telescope Array (NuSTAR). These metrics are: (1) angular resolution, (2) mass per unit area, and (3) production cost per unit area. The modular nature of this technology renders it appropriate for missions of all sizes — from Explorers that can be implemented by the end of this decade, to Probes and Flagship missions that can be implemented during the next decade.

Key areas of technology development include: (1) fabrication of substrates, (2) thin-film coating of these substrates to make X-ray mirror segments, (3) alignment and (4) bonding of mirror segments into mirror modules, and (5) systems engineering to ensure all spaceflight requirements are met.

Major accomplishments in the past year include: (1) successful fabrication of mirror substrates shown by optical metrology to have sub-arcsec point spread function (PSF); and (2) successful alignment, bonding, and X-ray testing of a pair of mirrors using four precisely machined spacers, achieving a 2.2" image, the best with lightweight X-ray mirrors. These accomplishments demonstrate the feasibility of making diffraction-limited X-ray mirrors using mono-crystalline silicon and the validity of the meta-shell approach. We expect to continually improve both image quality and overall Technology Readiness Levels (TRLs) over the coming years.

Background

The last five centuries of astronomy are a history of technological advancements in optical fabrication and optical-systems integration. Furthering our understanding of the cosmos requires telescopes with ever-larger collecting area and ever-finer angular resolution. In the visible and other wavelength bands, where radiation can be reflected at normal incidence, a large mirror area alone directly translates into a large photon-collecting area. However, due to its grazing-incidence nature, an X-ray telescope requires a combination of both large area and thin mirrors to increase photon-collecting area.

Three metrics capture the essence of an X-ray optics technology: (1) angular resolution, (2) mass per unit collecting area, and (3) production cost per unit collecting or mirror area. The X-ray optics of every successful observatory represents a scientifically useful compromise between the three metrics that was implementable in its specific technological, budgetary, schedule, and spaceflight opportunity context. The objective of this effort is to ready an X-ray telescope fabrication process that ever tilts the compromise toward better performance for given amounts of resources in terms of money and mass.

Our effort started in 2001, with the epoxy replication process developed for Suzaku. Instead of using thermally formed aluminum substrates, we used thermally formed (or slumped) thin glass for

substrates. Taking advantage of the already smooth surface of float-glass sheets, by 2007 we were able to make glass substrates that no longer needed the epoxy replication process, saving both time and money. In late 2007, we X-ray-tested a pair of glass mirrors and produced X-ray images better than 15" half-power diameter (HPD), meeting the requirement of the Constellation-X mission. Between 2007 and 2011, we continued to improve the glass slumping technique, culminating in a process that consistently makes glass mirrors of 6" HPD. Between 2011 and 2015, we developed a mirror alignment and bonding process that has produced technology-development modules with three pairs of mirrors, making X-ray images better than 8" HPD. Compared with Chandra, this technology would lower mass and cost per unit collecting area by nearly two orders of magnitude. Compared with XMM-Newton, it would reduce mass per unit collecting area by a factor of eight and cost by a factor of three, while significantly improving angular resolution. Compared with Suzaku and NuSTAR, it would improve angular resolution by an order of magnitude, while preserving their advantages in mass and cost per unit collecting area.

In 2016, based on successful development work funded by an Astrophysics Research and Analysis (APRA) grant, we changed our mirror technology from using slumped glass to using polished mono-crystalline silicon. The major reasons for this change include:

- Polished silicon mirrors have the potential for much better angular resolution than slumped-glass mirrors;
- Silicon has far superior material properties compared to those of glass: lower density, higher thermal conductivity, higher elastic modulus, and lower coefficient of thermal expansion; and
- The silicon fabrication process does not require mandrels as needed for the glass-slumping process, saving time and money.

In conjunction with the change of substrates from slumped glass to polished silicon mirrors, we also changed the overall approach to making an X-ray mirror assembly. Figure 1 illustrates the contrast between the old approach and the new one. Both start with small mirror segments and end with a full assembly, but they differ in the intermediate step. In the old approach, a large number of wedge-like modules are built, tested, and then integrated to form the final mirror assembly. In the new approach, a relatively small number of meta-shells are built, tested, and then integrated.
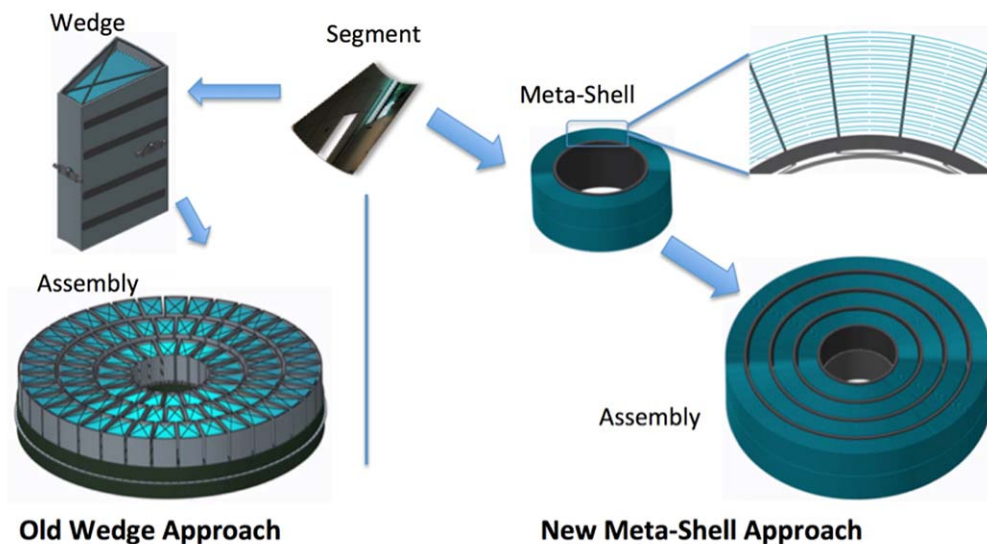
Fig. 1. *Illustration of two ways to build a large X-ray mirror assembly from a large number of small mirror segments. The wedge approach has been widely adopted and therefore has been the "standard" way, whereas the "meta-shell" approach has significant advantages.*

The new approach has several major advantages. First, each mirror segment is kinematically supported at four locations during the alignment and bonding process, minimizing gravity distortion. Second, because of the optimized locations of the four mirror supports, any frozen-in distortion and thus distortion after gravity release is minimized, making it possible to build and test sub-arcsec lightweight X-ray mirror assemblies in a gravity environment. Third, this construction process naturally defines the optical axis, making it much easier to both build and integrate meta-shells into a final mirror assembly. Fourth, the construction process proceeds naturally from inner shells to outer shells, making it much easier to baffle against stray light and realize much smaller inter-shell spacing, essential for maximizing packing efficiency.

Objectives and Milestones

The objective of this effort is to perfect a process for making mirror meta-shells that meet spaceflight environmental requirements and have progressively better performance in terms of angular resolution and effective area. As of June 2018, we have achieved better than 5" HPD. In the near term (2 to 5 years), we expect to continue and improve every aspect of the process to cross the 1" performance level. In the long term (5 to 10 years), we expect to reach 0.1".

The same set of milestones can be used to measure progress toward realizing both near-term and long-term objectives. They differ only in the X-ray image quality measured in arcsec. Each step or milestone has two metrics: image quality and consistency. The steps are as follows.

- Fabricating mirror substrates;
- Maximizing X-ray reflectivity by coating substrates with thin-film iridium or other material;
- Aligning individual mirror segments and pairs of mirror segments;
- Bonding mirror segments to a mechanical structure;
- Constructing meta-shells, requiring co-alignment and bonding of multiple mirror segments; and
- Environmental-testing meta-shells, with X-ray performance tests before and after.

Environmental tests include vibration, acoustic, and thermal-vacuum. X-ray performance tests include measurement of PSF and effective area at representative X-ray energies – e.g., 1.5 keV (aluminum Kα), 4.5 keV (titanium Kα), and 8.0 keV (copper Kα).

Progress and Accomplishments

In the past year, we made progress in every area of the technology: substrate fabrication; coating; mirror alignment; mirror bonding; and meta-shell design, analysis, construction, and testing.

Substrate Fabrication

In the past year, we validated a complete substrate fabrication process: starting with a block of commercially procured mono-crystalline silicon and ending with an X-ray mirror, with an image quality of about 0.4" HPD, shown in Fig. 2. This is about 20 times better than the best slumped-glass mirrors, comparable to or slightly better than the Chandra mirrors, and therefore the best astronomical X-ray mirror in the world. We expect to continually refine and perfect this process, not only improving mirror quality but also reducing production time and cost.
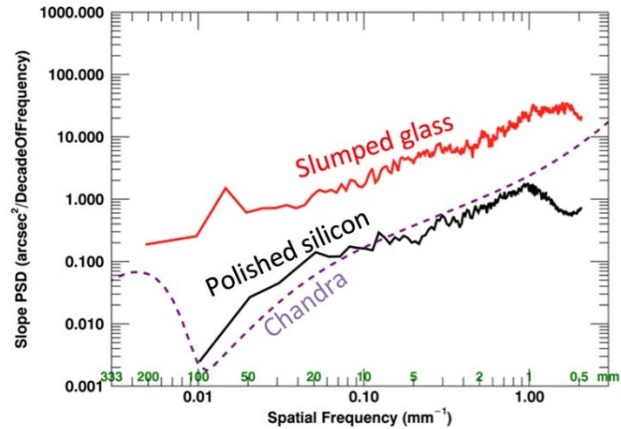
Fig. 2. *Status of lightweight mono-crystalline silicon mirror fabrication.* Left: *Photo of a 0.9-mm-thick mirror.* Right: *The axial-slope power-spectral density (PSD) in comparison with typical slumped-glass mirrors and that of the Chandra mirrors. As of June 2017, the silicon mirror is about 20 times better than the best slumped-glass mirrors and comparable to or slightly better than the Chandra mirrors.*

The substrate fabrication process consists of the following steps:

1. Figure generation.
2. Slicing or light-weighting.
3. Edge- and backside lapping.
4. Acid etching.
5. Stress-polishing.
6. Trimming.
7. Edge-polishing.
8. Ion-beam figuring.

Our work in the coming years will be to refine and perfect each step, not only improving quality but also reducing production time and cost.

Coating

Mirror substrates require an optical coating (e.g., 20-nm iridium) to enhance X-ray reflectivity. The stress of an iridium film, typically several Giga-Pascal, severely distorts the figure of a thin substrate, greatly degrading its imaging quality. We recently started collaborating with Dr. Mark Schattenburg and Dr. Youwei Yao of MIT to develop a process using silicon oxide's compressive stress on the convex side to precisely balance the compressive stress of the iridium coating on the concave side. Together we conducted a number of trials, completely coating two mirrors with less than 0.2" image degradation. This is the first time ever, to our knowledge, that anybody in the world has ever achieved this level of stress cancellation and figure preservation of thin X-ray mirrors. We expect to continue this collaboration to perfect the process, both in further reducing or eliminating the figure degradation and in increasing the efficiency of the process to minimize cost.

Mirror-Segment Alignment and Bonding

Traditionally, the alignment of a mirror is achieved by using a 6-dof (degrees of freedom) stage that can translate and orient a rigid body in all possible ways. We used this traditional method until early 2016, when we switched to using the fact that an X-ray mirror segment, or more generally a cylindrical mirror segment, can be supported at four posts (or spacers) with its orientation uniquely determined. The orientation of the mirror can be fine-tuned by precise adjustment of the radial height of one or more of these posts. Figure 3 shows our implementation of this concept, where each

mirror segment is supported by four spacers whose radial heights are precisely machined. In practice, this is an iteration process guided by Hartmann measurements.
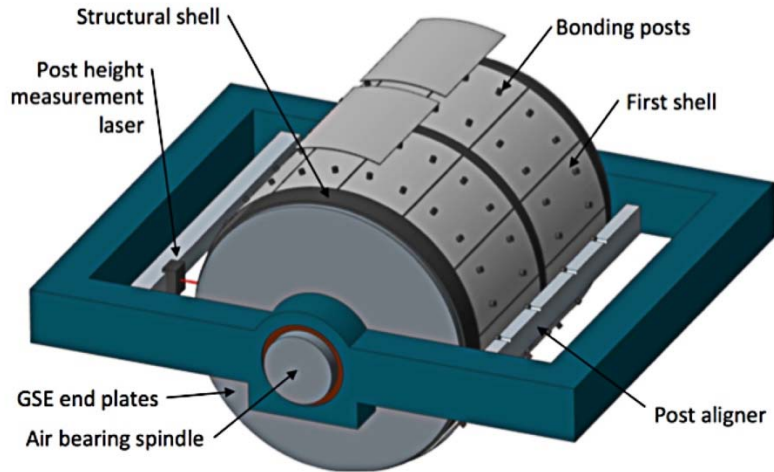
Fig. 3. *Illustration of the mirror alignment and bonding process. Each mirror segment is supported and aligned by four spacers. The radial heights of these spacers are precisely and iteratively machined in-situ, guided by Hartmann measurements (GSE, ground-support equipment).*

As shown in Fig. 3, once the four spacers have been machined to achieve alignment for the mirror segment, a minute amount of epoxy is applied to each spacer. The mirror segment is then placed on the spacers and a small vibration jiggles the mirror into its optimal alignment. Once the epoxy cures, the mirror is permanently bonded.

In the past year, we continued with stand-alone experiments to improve several key elements of this alignment and bonding process. First, the alignment is uniquely determined by the four spacers. A mirror was repeatedly placed and removed to show that the images of the different placement trials precisely reproduce the same quality and location. Second, a grinding and buffing process can deterministically change the height of a spacer with sub-µm precision. Third, the application of epoxy on the spacer does not change the alignment of the mirror, implying that the epoxy thickness variation from spacer to spacer is acceptably small. Our effort culminated in the buildup and X-ray-testing of a module consisting of a single pair of silicon mirrors, as shown in Fig. 4, achieving 2.2" HPD images, agreeing well with expectation based on optical surface metrology. We expect to continue this improvement process such that we will cross the 1" image barrier in the next two years.
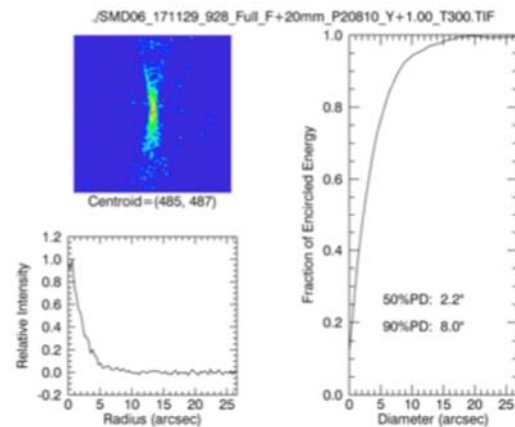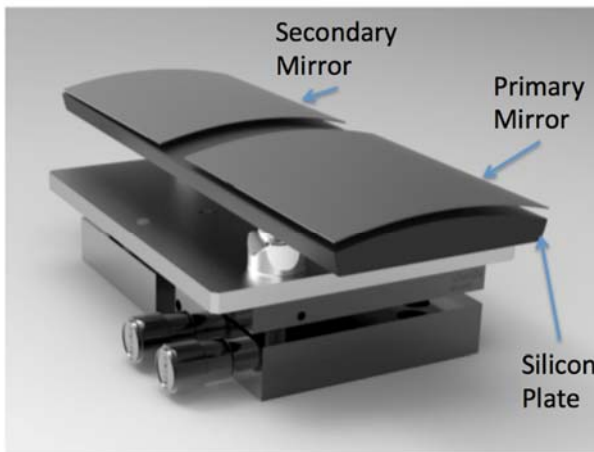
Fig. 4. Left: *a pair of mono-crystalline silicon mirrors aligned and bonded using four spacers each on a silicon plate.* Right: *X-ray image and its properties of the pair of mirrors on the left when fully illuminated with 4.5 keV X rays in a 600-m X-ray beam line in Area 200 at GSFC (EED, Encircled Energy Diameter). The 2.2" HPD image is the best image produced by lightweight X-ray mirrors in the world.*

Meta-Shell Design, Analysis, and Test

Since the conception of the meta-shell approach a little over a year ago, we have conducted a design, analysis, and test exercise. Figure 5 shows the preliminary design of a mirror assembly with an outer diameter of 1.3 m. It consists of six meta-shells, each having about 20 layers of mirrors, not all of which are drawn. A set of preliminary structural, thermal, and performance analyses has led to the following conclusions:

- Each meta-shell, with its relatively thick structural shell and interlocked mirror segments, is stiff and has good mechanical integrity; assuming the use of a standard aerospace epoxy, such as Hysol 9309, and a reasonable bond area for each spacer, about 2 mm in diameter, the meta-shell can sustain launch loads; this conclusion has been empirically verified by a set of vibration tests of articles shown in Fig. 6;
- The meta-shell construction process, as shown in Fig. 3, where the optical axis is horizontal, does not freeze in any significant amount of distortion, meaning that when the meta-shell is turned vertical, the frozen figure distortion is sub-arcsec;
- A meta-shell can be X-ray-tested in a horizontal beam line. The images of some of the mirrors show minimal distortion; by rotating the meta-shell, we expect to be able to fully characterize the imaging performance of the entire meta-shell; and
- Because the meta-shell is made of silicon, with only trace amounts of different materials such as epoxy and iridium, a bulk temperature change of 1°C changes the imaging performance by only 0.1" HPD.
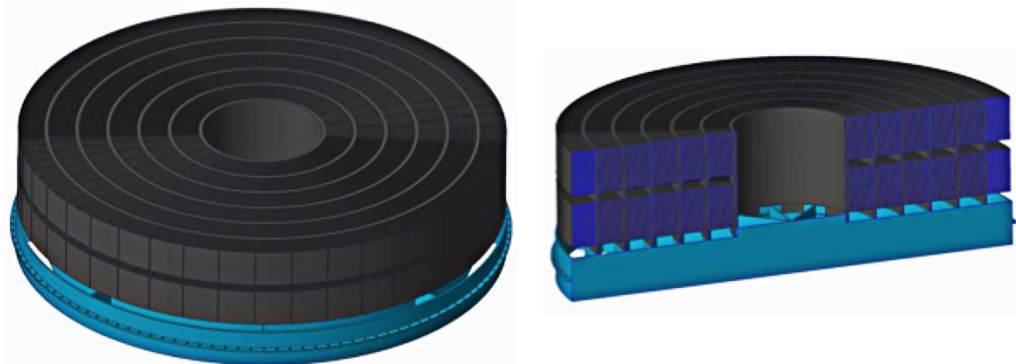
Fig. 5. *Illustration of a mirror assembly consisting of six meta-shells. Each meta-shell is flexure-mounted onto an aluminum (or composite) structure wagon wheel. The spokes of the wagon wheel are all hidden behind the spacers and cause no additional blockage.*
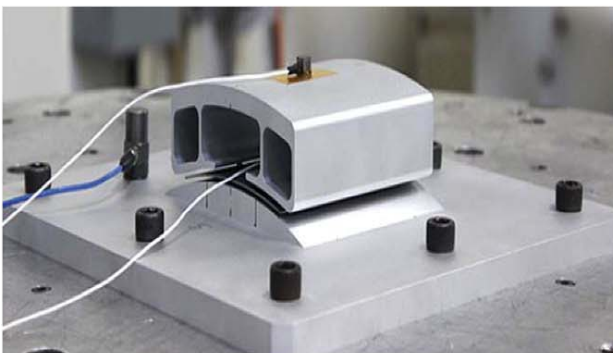
Fig. 6. *Two articles tested on a vibration table to prove the concept of bonding thin brittle mirror segments with four spacers.* Left: *a thick silicon mirror segment bonded by four spacers to an aluminum base plate simulating the structural shell and by another four spacers to a light-weighted aluminum block simulating the mechanical effect of additional mirror segments.* Right: *an aluminum cylinder bonded with 54 small clear glass mirror segments in three layers simulating silicon mirror segments. Both articles were vibrated to, and survived, a quasi-static level of 12.3 g, demonstrating that the meta-shell construction meets a significant and necessary requirement.*

Overall, the analysis and test results have shown that the meta-shell approach is sound in every aspect: performance, thermal, and structural. We note that this approach incorporates the merits of all four currently operating missions' X-ray mirror assemblies.

Path Forward

Based on our previous work, as well as heritage of previous missions such as Chandra, XMM-Newton, Suzaku, and NuSTAR, we have conceived and validated the meta-shell approach for our technology development. Numerous stand-alone experiments and finite element analyses, both structural and thermal, have validated the approach. In the coming year, we will start building and testing mirror modules, or meta-shells, based on this approach. Initially, we will continue to build and test single pairs. Then, we will proceed to build a meta-shell with three layers of mirrors, with a total of 72 mirror segments. We will then X-ray-test this meta-shell, environmentally test it, and repeat the X-ray test to verify the environmental testing did not degrade its performance.

For additional information, contact William W. Zhang: *william.w.zhang@nasa.gov*
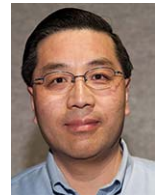
US Contributions to the Athena Wide Field Imager

Prepared by: David Burrows (Department of Astronomy & Astrophysics/PSU)

This document is the second (FY18) annual technical report for the above-mentioned grant to our unsolicited NASA proposal for US contributions to the Athena Wide Field Imager. The project has four subcontracts to MIT, SAO, Stanford, and Southwest Research Institute (SwRI). The report is broken into five sections covering the work done by I) PSU and SwRI, II) MIT, III) SAO, IV) Stanford, and V) a travel summary. The period covered by this report is from August 2, 2017 through August 1, 2018.

TECHNICAL SUMMARY
The scope of our grant consists of the following areas:
1)Development of a Science Products Module and its software/firmware. The SPM is a high-speed CPU board provided by SwRI that will provide additional on-board data processing capability beyond what the main instrument CPU board can handle. The software running on it will consist of a Transient Analysis Module provided by PSU and a Background Analysis Module provided jointly by MIT and SAO.
2)Support of design and testing of the VERITAS2 ASIC, which provides the readout signal chain for the DEPFET detectors. This work is being done by SLAC at Stanford and by Brookhaven (under subcontract from Stanford). Stanford has contributed additional effort related to Athena that was not funded by this grant, but is described below.

I) Penn State and Southwest Research Institute
The Pennsylvania State University (referred to hereafter as Penn State or PSU) is the prime recipient of this grant. During the second grant year we have performed the following work:

1) Obtained export licenses to cover the work done under this grant so that we can have discussions with our European partners without violating export control laws. We are still in the final stages of getting signatures from the European collaborators to the Ultimate Consignee documents.

2) Attended a number of Athena meetings and general scientific meetings at which the Athena US contributions were presented.

3) Negotiated Assessment Criteria for inclusion of the SPM with the WFI leadership team at MPE. This resulted in a document describing these assessment criteria.

4) David Burrows (PI, PSU), Mike Zugger (SE, PSU) and Steve Persyn (SwRI) attended four technical interface meetings for the WFI Instrument Control and Processing Unit (ICPU) to discuss internal interfaces and design of the ICPU. These quarterly meetings were not anticipated in our original proposal, but we have been able to fund this travel using existing funds. The design of the ICPU has changed significantly over the past year, with the current design envisioning a split ICPU consisting of a main unit located far from the instrument camera head and containing the Central Processing Module, Power Distribution Unit, and SPM, and a Remote Terminal Unit located close to the detector electronics that includes a SpaceWire router, Analog Interface Board, Filter Wheel Controller, and additional power distribution. The overall architecture is shown in Figure 10.
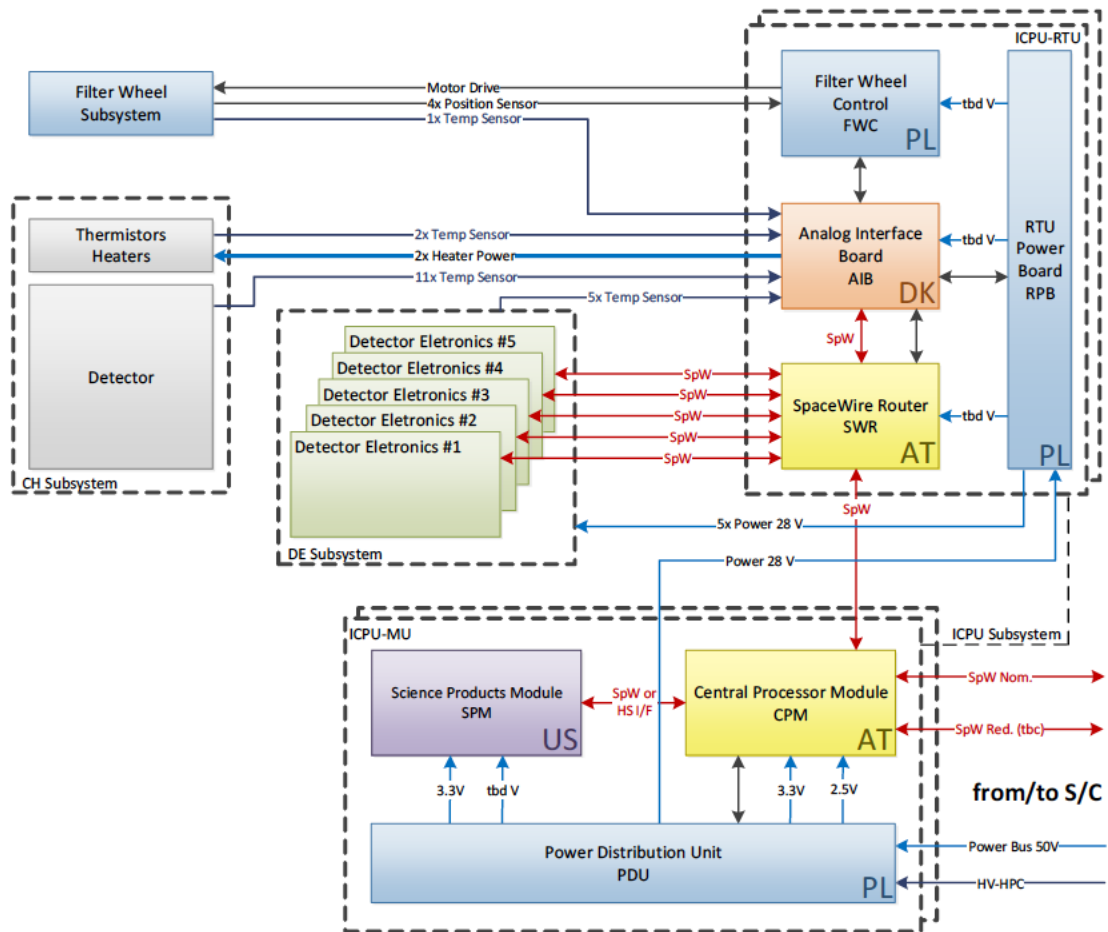
Figure 10: Overall WFI block diagram, showing the relationship between the SPM and the rest of the electronics.

The SPM receives power from the PDU and receives and transmits data and telemetry through the CPM (although at the last ICPU Technical Meeting there was discussion of the possibility of the SPM receiving data directly from the Spacewire router in the Remote Terminal Unit; this trade has not been resolved).

5) In response to preliminary estimate from MIT of the processing requirements for the Background Analysis Module, SwRI has modified the baseline SPM design to incorporate a

Microsemi RTG4 FPGA in place of the Virtex V4 FPGA in the original design. The new SPM design is shown in Figure 11.
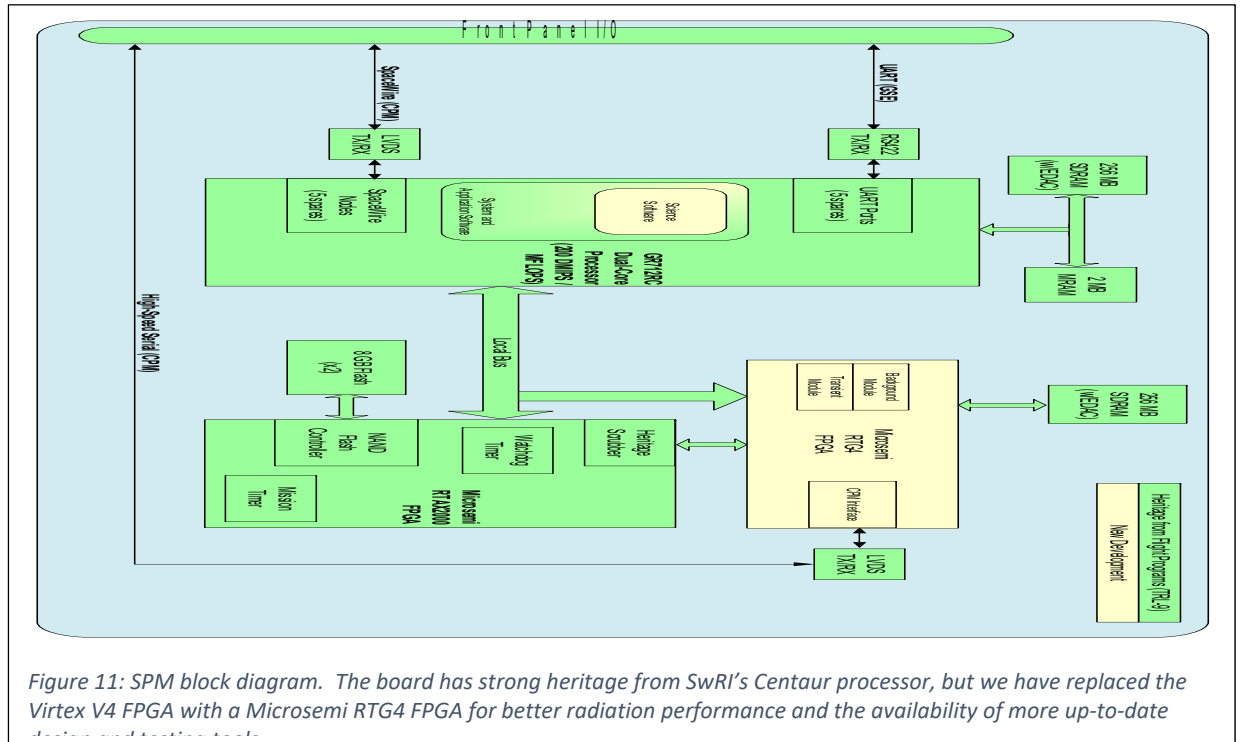
Figure 11: SPM block diagram. The board has strong heritage from SwRI's Centaur processor, but we have replaced the Virtex V4 FPGA with a Microsemi RTG4 FPGA for better radiation performance and the availability of more up-to-date design and testing tools.

6) Dr. Pragati Pradhan has been developing a detailed flow diagram for the transient analysis algorithm and doing preliminary tests of this algorithm on Swift XRT data sets. The latest version of the algorithm is shown in Figure 12. Her work to date has focused on source detection and subsequent analysis of source variability. Initial testing was performed using data sets from Swift and Chandra. She is now working on producing simulated data sets using the Athena SIXTE simulator, which she is using to develop and test the transient analysis algorithm on a desktop computer. This testing will lead directly to verification of the SPM assessment criteria for the transient analysis. Preliminary results show that the algorithm can detect sources and match them with catalog source in 8 seconds, using a SIXTE simulation of a 1000 s observation of a typical deep sky field.

Figure 12: The preliminary Transient Analysis Module flowchart.

7) Transient source rates: Dr. Pradhan has also been estimating rates at which transient sources of various types will be discovered by the SPM. Rates for "galactic" X-ray transients in distant galaxies are very small. Off-axis GRBs, tidal disruption events, and other similar transients may trigger detections at a rate of less than one per month. AGNs are likely to provide triggers on at least a weekly basis (with large uncertainties). The most exciting prospect is a class of rapid X-ray transients discovered in searches of serendipitous Chandra source detections; these could trigger the WFI at a rate of several per day, and the nature of these sources is completely unknown. Dr. Pradhan has presented these results at a number of national and institutional venues including MPE (Germany, Oct. 2017), Univ. Southampton (UK, Oct. 2017), AAS (Washington DC, Jan. 2018), Astronomical Society of India (India, Feb. 2018), HEAD (Chicago, March 2018), Athena SWG 2.6 meeting (Radboud Univ., Netherlands, June 2018), and ISDC (Univ. Geneva, Switzerland, June 2018).

8) Drs. Burrows and Pradhan are both preparing to attend the Athena Science Workshop entitled 'Exploring the Hot and Energetic Universe' in Palermo in Sept, 2018, and will give contributed presentations on the Athena WFI SPM Transient Analysis concept.

II) Massachusetts Institute of Technology (MIT)

This year we concluded our analysis of 'full-frame' images from Suzaku and Chandra, which showed a clear spatial correlation between charged-particle tracks and un-rejected background events. These results were reported to the US WFI team and the broader WFI Proto-consortium. They were also presented as posters at several conferences. We then began a similar analysis of

simulated WFI background images provided to us by European members of the WFI background working group, and showed that background could be reduced by ignoring spatial regions surrounding particle tracks. The latter result provided independent confirmation of earlier work by the MPE WFI team. We plan to refine this this approach in the coming year. We also supported development and documentation of requirements for the SPM's Background Analysis Module (BAM), and began to assess engineering resource requirements for implementing a generic background reduction algorithm in SPM firmware.

1) We supported bi-weekly telecons of the WFI Proto-consortium's Background Working Group.

2) We supported the following face-to-face meetings with other members of the WFI team:
   - WFI Proto-consortium (WFIPC) & WFI Background Working Group (WFIBWG) meetings, Warsaw, October, 2017
   - WFIBWG meeting in Milan, January, 2018
   - US WFI Team meeting in Baltimore, March 2018
   - WFIPC & WFIBWG meetings in Garching, April 2018

3) We presented results of our WFI background analysis work at the following meetings and conferences:
   - HEAD meeting, Chicago, March 2018 (Miller et al., poster)
   - IACHEC meeting, Rome, April 2018 (Grant et al., talk)
   - SPIE meeting, Austin, June 2018 (see Grant, C.E., Miller E.D., Bautz, M.W., Bulbul E., Kraft R. P., Nulsen P., Burrows, D. N., Allen S., 2018 "Reducing the ATHENA WFI background with the Science Products Module: Lessons from Chandra ACIS", Proc. SPIE 10699, 10699-4H)

4) We completed our analysis, begun last year, of Chandra/ACIS S3 full-frame data (562 frames in total). Briefly, we showed that charged particles produce un-rejected events that masquerade as cosmic X-ray events in Chandra ACIS data at a rate of about 0.1 event per particle track. There is a strong spatial correlation, at distances less than within 20 pixels, between the tracks and the events. If it were possible to identify particle tracks onboard ACIS, its non-X-ray background could be reduced. Details are available in the SPIE contribution noted in item 3 above.

5) We began a study of simulated background data provided to us by our European colleagues in the WFIBWG. The data simulate the result of some 133 million primary cosmic protons interacting with the WFI instrument. We use these data to create WFI images containing all of the ionization produced by these particles, either directly or by secondary radiation generated in the instrument. We then apply agreed-upon (XMM-like) event detection and background-discrimination (grading) algorithms to produce simulated background spectra. We also look for spatial correlations between so-called 'MIP'[‡] events and un-rejected background events.

[‡] 'MIP' is short for minimum ionizing particle, but the conventional WFI team definition of 'MIP' is any event having at least 15 keV of deposited energy.

Preliminary results shown in Figure 13 yield a total 2-7 keV background event rate roughly 33% higher than the WFI requirement of 5 x 10^{-3} ct s^{-1} keV^{-1} in the 2-7 keV band (left panel). Ignoring events in the neighborhood of MIPs reduces this background. For example, if a region of radius 180 pixels is ignored around each MIP, the background can be reduced to the required level (right panel). The background reduction produced by this 'spatial anticoincidence' technique comes at the expense of instrument live-time in the affected part of the field of view. Approximately 25% of the total cosmic photon flux would be lost if an exclusion radius of 180 pixels were adopted. These results are consistent with those obtained at MPE.
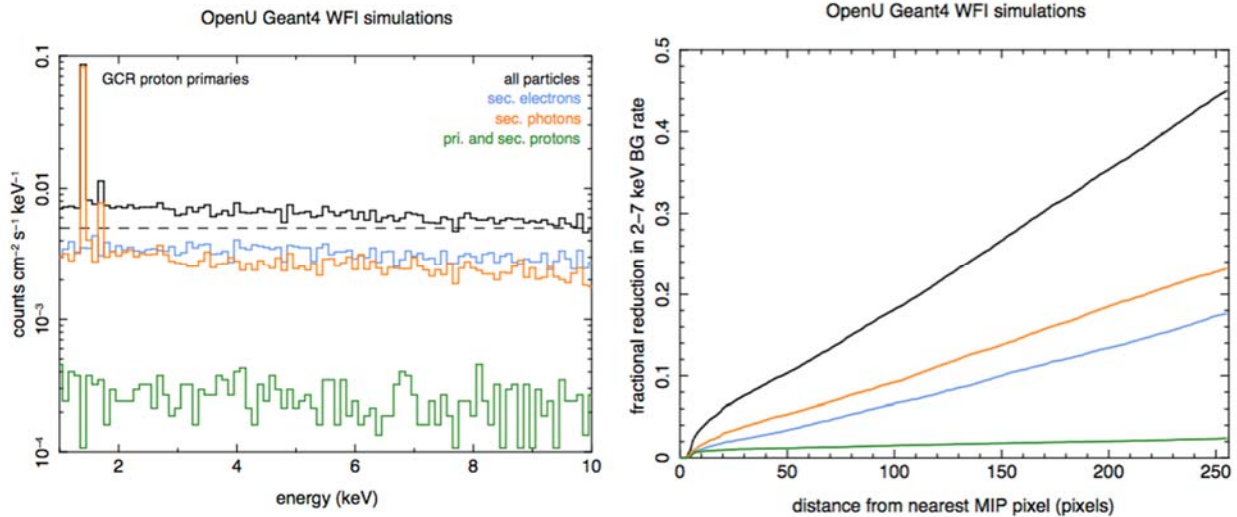

Figure 13: MIT analysis of simulated WFI non-X-ray background produced by Galactic cosmic ray protons incident on the instrument, based on GEANT4 simulations performed by the WFI team at the Open University. LEFT: The residual non-X-ray background spectrum after standard event detection and background discrimination algorithms have been applied. The different colors show contributions from different secondary particles. The total background spectrum (solid black curve) is nearly independent of energy with an amplitude of ~6.7 x 10^{-3} ct s^{-1} cm^{-2} keV^{-1}, which exceeds the WFI background requirement of < 5 x 10^{-3} ct s^{-1} cm^{-2} keV^{-1} (dashed horizontal line). RIGHT: The background level can be reduced by ignoring regions surrounding pixels with large amplitude (MIPS ≡ pixels with amplitude > 15 keV). Ignoring a region of radius ~180 WFI pixels around each MIP, for example, would reduce the background level below the WFI requirement. Analysis and figure provided by Eric Miller.

6) We have produced a preliminary flowchart of a firmware implementation of an on-board background rejection scheme for the purpose of scoping the hardware requirements in order to ensure that the SPM has the necessary processing speed. Preliminary estimates indicate a change in design from the baseline board housing a Leon 2 processor, a Virtex V4 FPGA and an RTAX2000 FPGA to a board with a Leon 2 processor, a Microsemi RTG4 FPGA and an RTAX2000 FPGA.

Plans:
We plan to explore methods for improving the efficiency of the spatial anti-coincidence technique described above. Figure 13 suggests an approach for doing this: since very little

background reduction is achieved by excluding regions around MIPs due to (primary or secondary) protons, one would presumably gain efficiency if one could identify MIPs resulting from secondary electrons, and exclude only regions around them. The potential for this approach is highlighted by Figure 14, which shows MIPs resulting from secondary protons and electrons, respectively. Most MIPs are due to secondary protons, but most of the un-rejected background is due to secondary electrons. Thus we aim to find algorithms that can distinguish the physical origin of the MIPs on the basis of the data produced by the WFI. Ever hopeful, we plan to search for a graduate student to assist in this effort.

We plan to continue our efforts, in collaboration with the US WFI team and WFI team leadership at MPE, to refine the data requirements for the WFI BAM. We also expect to develop a more accurate picture of the hardware resources needed to implement BAM algorithms.
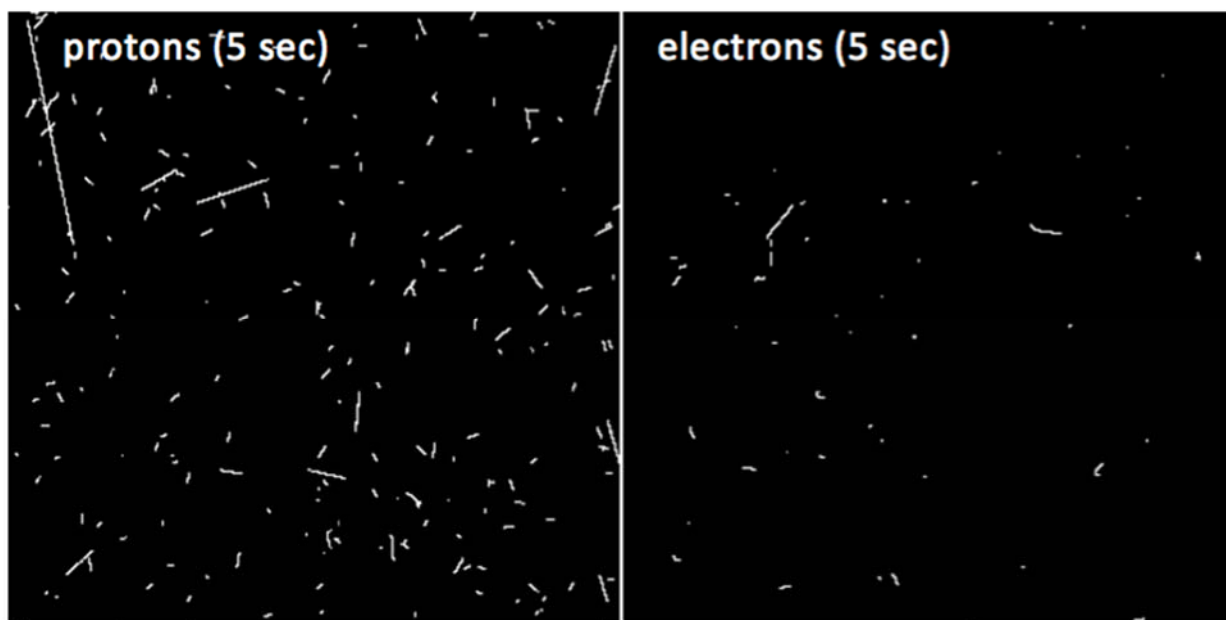
Figure 14: Simulated long-exposure images of MIPs produced by secondary protons (left) and secondary electrons (right) generated by the MIT team from GEANT4 data provided by the Open University team. Most MIPs are protons, but the un-rejected background is mostly due to electrons. Note that the WFI frame exposure time is 5 ms, so these images are each equivalent to the sum of 1000 WFI frames. Figure produced by Eric Miller.

We will continue to support regular WFIBWG telecons and workshops, US WFI team meetings, and WFI Proto-consortium meetings as required.

Finally, we will work with the US WFI team to prepare and present to WFI team leadership the best possible scientific and technical case for inclusion of the SPM in the flight WFI instrument.

III) Smithsonian Astrophysical Observatory (SAO)

Dr. Esra Bulbul began work at SAO in Sept, 2017. She is principally responsible for the data analysis and modeling work done at SAO on algorithm development for the Background

Analysis Module for the SPM. Her first task was to extend the analysis on the Swift XRT data that had been started by R. Kraft. Two full frames of data are telemetered to the ground each day, and each full image contains both X-ray and charged particle events. The full dataset, more than 8000 data frames, was provided to SAO by the Swift team at PSU. The goal is to evaluate the efficiency of the default ACIS and Swift event processing algorithms, assess the improvements that could be made by looking at 5x5 islands rather than the default 3x3 islands, and investigate alternative particle identification schemes. Most significantly, we searched for spatial correlations between events accepted as X-rays and those rejected as background based on pattern matching and pulse-height discrimination.

Using the full Swift XRT data set, she computed the two-point correlation the good events, defined as valid Swift XRT X-ray patterns and energies, and bad events. She discovered a weak correlation between good events above 1.5 keV and the bad events, but no correlation for the lower energy events. Careful examination of the data demonstrated that many of the low energy events were actually hot pixels which should be removed. She found that the number of events per frame as a function of CCD temperature showed a strong trend with more events occurring at warmer temperatures. She then created images of the event locations on a yearly basis, and any pixel with two or more events over the frames of the data was identified as a hot pixel and excluded from further analysis. After excluding all events from this bad pixel list, the number of counts per frame is found to be independent of the temperature.

After removal of hot pixels, frames with contamination from a light leak, and South Atlantic Anomaly passages, we ran the two-point correlation over the entire data set. We first computed the two-point correlation distribution of good events with other good events for X-rays in 5 energy bands. There is strong evidence of a correlation at spatial scales of < 50 pixels. There is also a hint of a correlation on larger scales, ~400 pixels. The Swift XRT data is continuously exposed to the sky during these observations, and there is often a bright X-ray source within the FOV. We concluded that this correlation is due to the presence of these X-ray sources in the field.

We also computed the two-point correlation distribution of the good events with the bad events. There is a much weaker peak on the smallest spatial scales, with no hint of the larger scale correlation. Additionally, there is significant year to year variation in the good-bad two-point correlation. The reason for this is at present unknown, but may be related to the distribution of source intensities over a given year of observation.

Because of the continuous exposure to the sky, we concluded that the Swift XRT data was not the ideal set to understand the relationship between the particle events and the unrejected background in the Athena WFI. We developed a very sophisticated point source detection algorithm. Developing a technique to account for the sky visibility to remove the bright point sources would have little relevance to our main objective of understanding the Athena WFI background. Additionally, the orbit of Swift (LEO) is very different than that proposed for Athena (L2). In particular, the charge-particle energy spectrum is very different. The protons that dominate the charged-particle background are much lower in energy for Swift than for Athena. Finally, the focal plane sensor for the Swift XRT is an EPIC MOS device, significantly different than the WFI DEPFETs. The EPIC MOS devices have smaller pixels, a smaller

depletion depth, and a much slower frame rate. For these reasons, we decided to pursue another avenue of investigation.
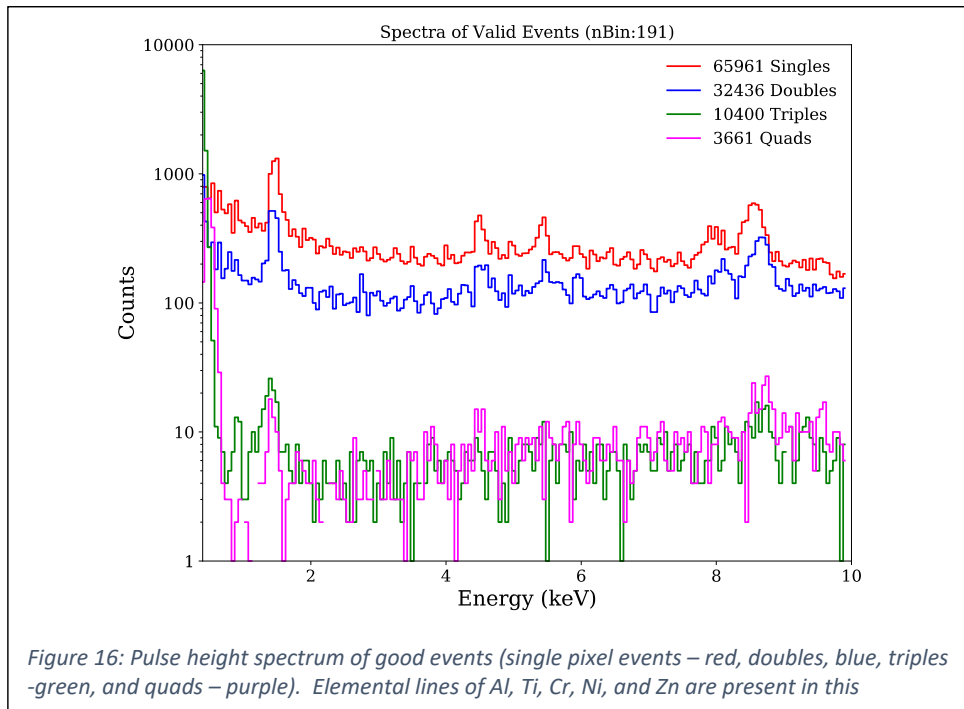
We therefore began a careful examination of the XMM PN camera data taken in Small Window mode (SWM). In SWM mode, only a small region of the sensor is read out at a rapid (~5.5 ms) rate, similar to the default frame rate for the Athena WFI. These data are also typically taken with the filter wheel in the closed position so that there are no sky X-rays in the field. Any event that is identified as valid by the on-board software must have originated from a charged-particle interaction in the detector or is a secondary X-ray created by the interaction of a charged-particle in the camera housing. Most importantly, these data are taken with the MIP filtering disabled, so that any pixel that is above a threshold value is telemetered to the ground. Thus we have access to all the events that appear as valid X-rays and charged particle. There are ~300 PN SWM observations taken since the beginning of the mission, with typical exposure times of ~3-4 ks. The data are in the form of event files. We turned these event files back into images and created a time series movie for each of the observations for further analysis. Only ~10% of the frames have events, either valid X-ray events or charged-particles, in them.

Upon careful examination of the data, we realized that a large number of the valid events had energies < 400 eV. We discussed this with Michael Freyberg of MPE and he explained to us that the vast majority of these events are due to electronic noise in the output amplifiers and should be rejected. These are now filtered out of the data. Additionally, we removed events that are located at the detector boundary. There is no way to determine if an event at the boundary is a single pixel event or whether it is the partially collected charge of an event that landed off the active area of the detector.

With this filtering, we identified frames with just rejected events (event that are not 'good' events due to either the PH being to large or the pattern not matching a real X-ray - 1.5% of the total frames), frames with just good events (0.02% of the total) and frames with at least one rejected event and at least one good event (0.003% of the total frames). Note that the vast majority of frames have no events because the frame time is ~5.67 ms in Small Window mode. The numbers of frames with just bad events and with just good events are shown in Figure 15.

Figure 15: Fraction of frames with just bad (blue) and just good (green) as a function of time. There is a strong variation correlated with the Solar cycle.
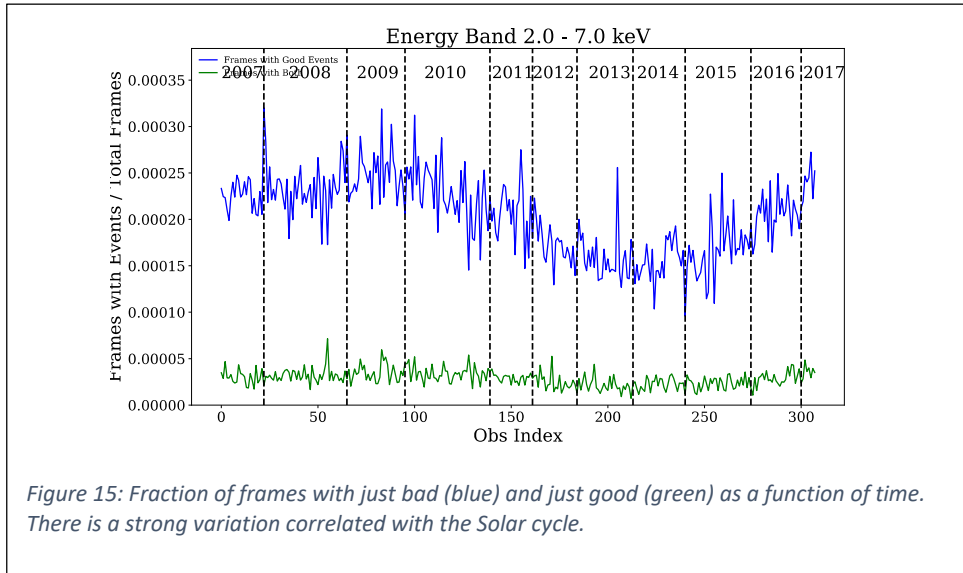
We created the spectrum of the good events shown in Figure 16. The spectra are broken down by event type – single pixel events, doubles, triples, and quads. The PH spectra are relatively flat, typical of instrumental background, with elemental emission lines clearly present from materials in the camera body.

Figure 16: Pulse height spectrum of good events (single pixel events – red, doubles, blue, triples -green, and quads – purple). Elemental lines of Al, Ti, Cr, Ni, and Zn are present in this

We computed the temporal correlation between good events as shown in Figure 17. If the good events are independent, the correlation time should be on the order of the time between events (or the reciprocal of the rate). We find that the correlation time constant is roughly the same as the reciprocal of the rate, demonstrating the independence of the events. This confirms that our

filtering has removed most of the instrumental artifacts associated with the long reset time constant of the output amplifiers.

Most recently, we resolved an algorithmic problem of the connectedness of multiple complex islands of charge in individual frames. We can now identify spatially separated peaks of charge with arbitrarily complex patterns, and identify the location of an individual island as the pixel with the highest signal.

Figure 17: Temporal correlation function of time between good events.
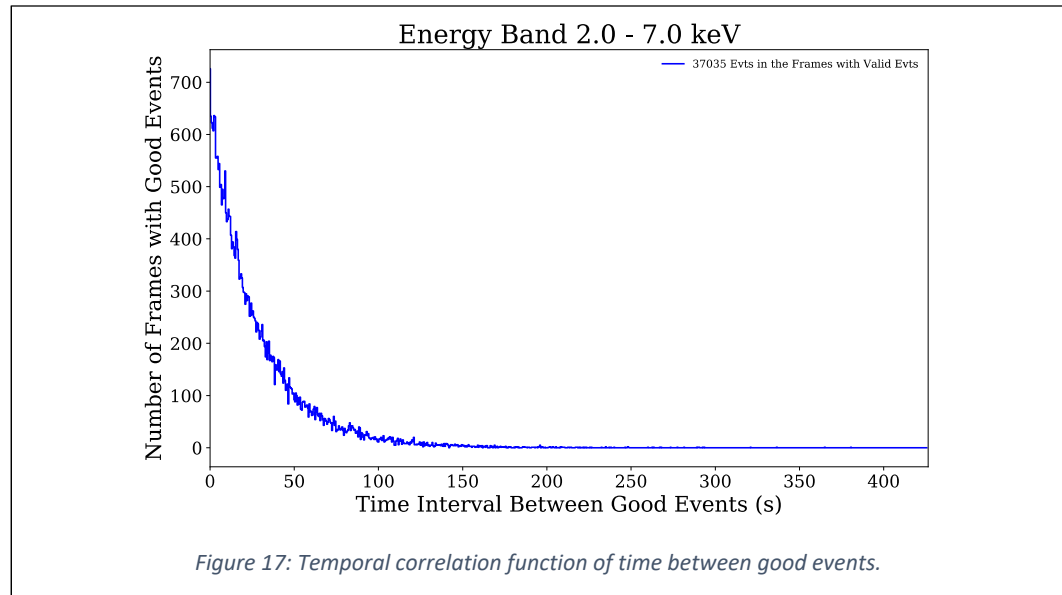
We are now coding the algorithm to do the two-point spatial correlation of good events, of bad events, and good events with bad events. Our goal is to make a detailed comparison of the spatial correlation, spectrum (of both the good and the bad events), and rate with the WFI Geant-4 simulations being used by our MIT colleagues. We will also look for trends and correlations in pulse height and event grading. One line of future investigation is looking at the branching ratios of the good events and compare with that measured for the sky X-rays. If many of the 'good' events are secondary electrons, as suggested by the simulations, it may be that there are some differences in the branching ratios of X-rays versus these electrons.

Drs. Bulbul and Kraft attended the Athena WFI Background Working Group meeting in Milan in January, 2018 and the WFI Proto-consortium meetings in Warsaw in Oct, 2017 and in Garching in Apr 2018. Drs. Bulbul, Kraft, and Nulsen attended the meeting of the US consortium in Mar 2018 in Baltimore. Dr. Bulbul prepared a talk and a paper for the 2018 SPIE meeting in Austin, TX. Drs. Bulbul and Kraft are both preparing to attend the Athena Science Workshop entitled 'Exploring the Hot and Energetic Universe' in Palermo in Sept, 2018, and will give contributed presentations on Athena WFI and XIFU science topics.

IV) Stanford University and SLAC

Efforts by the Stanford/SLAC WFI team (Allen, Herrmann, Mantz, Wilkins) during the year were threefold: firstly, we continued our successful engagement in the ASIC design and testing

activities with colleagues at MPE (see Section A below); secondly, we advanced our exploration of the fast timing capabilities of the WFI for X-ray reverberation mapping of Galactic black hole binary systems (Section B); and thirdly, we began an exploration of the potential of machine learning algorithms for the on-board cleaning of WFI data, to remove particle-induced background events (Section C).

Herrmann and Allen attended the WFI consortium meeting in Warsaw in October 2017, reporting on the work in Sections A and B. Herrmann and Wilkins attended the April 2018 consortium meeting in Munich, providing further updates on these topics. The full Stanford/SLAC group attended the US team meeting in Baltimore in March 2018, making presentations on Sections A-C. Herrmann presented the work in Section 1 at the SPIE meeting in June in Austin, TX. Herrmann has been on leave and based at Brookhaven National Laboratory since May 1, 2018, but is continuing to support the Athena WFI.

A) ASIC design and testing

We have continued our studies of DEPFET drain readout as a potential design option for the Athena WFI, exploring whether it fulfills requirements with sufficient margin. After the first proof-of-principle measurement last year, we dedicated significant effort to developing techniques to determine the operation parameters for this readout mode in a quick and efficient manner, so as to be able to optimize operation and guide the design of the new chip. Studying the VERITAS 2.1 design in simulations, and on the test bench, we determined the VERITAS 2.1 operating condition range and were able to suggest optimum operating conditions and timings for use by the MPE team in their DEPFET measurements.

We also developed a DEPFET operation parameter optimization procedure, utilizing the debugging features included in the VERITAS design, to speed up the DEPFET characterization measurements. This improved procedure can cut the ramp-up phase for new detectors from more than a week to approximately one day, allowing more rapid measurement campaigns for various DEPFET variants and/or for more time to be spent on detailed characterizations of specific sensors. The technique also allows us to measure in-situ the DEPFET bias current inhomogeneity distribution, a parameter that was previously only accessible with separate probe station measurements. Such data are valuable to the overall DEPFET sensor development effort and proved crucial in aiding the next VERITAS input stage design choices (which have to cope with the aforementioned DEPFET inhomogeneity).

Extensive measurements of DEPFET variants performed by the MPE team have shown that the bias variations are larger than anticipated during the VERITAS 2.1 design process, and may pose a problem for the operation of larger sensors. We used these insights to derive lower I2V gain factors (25, 35, 50 kOhm) to handle the worst case bias variations seen in pre-flight productions. The highest gain should still provide the same (excellent) noise performance demonstrated by the measurements with VERITAS 2.1. We conducted extensive simulations to verify these design changes and their expected impact on performance. The excess noise in channels 3, 31 and 63 is now fully understood: it originates from parasitic capacitance in the debugging network between the preamplifier input and filter output. We changed the VERITAS 2.2 design to fix this problem.

We also addressed the systematic 8-channel pattern previously noted in the drain readout measurements. While we are still investigating the exact mechanism of this effect, we have identified a slight asymmetry in the VERITAS 2.1 layout that might cause this effect: channel 3 of every block of 8 is different and includes special bias distribution features. We have decided to modify the layout and move the amplifier bias distribution out of the channels to make sure that in VERITAS 2.2 all channels will have the same layout.

We performed simulations for the differential output buffer of VERITAS 2.1 and studied the cause of sporadic oscillation that can attributed to NMOS to PMOS mismatch in the AB output stage. For VERITAS 2.2, we developed an improved differential output buffer that allows the chip to drive a commercial ADC directly, hence reducing system component count and complexity.

At the end of last year we faced an ASIC-related hazard that resulted in permanent damage to an input channel. We performed a series of measurements with the ASIC test setup and simulated the input stage to understand what hazard condition might have caused the damage. It seems that a large positive input potential (from 'bad' bias conditions or clocking errors) can cause a drain bulk punch-through in one NMOS transistor of the offset current stage. This seems in turn to often result in a latch-up condition. To mitigate these conditions, we developed two clamping circuits: one at the input pad and another after the active cascode, before the I2V stage. These clamp circuits will require an additional input pad. While we have performed extensive simulations to estimate the performance impact of these changes, we decided to submit two chip variants of VERITAS 2.2 to mitigate risk: one with these clamping circuits and one without.

Further effort went into maintenance of the existing VERITAS 2.1 design database and the software tool chain, in order to prepare for the upcoming submission. Within this effort, we verified that the VERITAS 2.1 ASIC physically in hand is identical to the VERITAS 2.1 design database. We anticipate submitting two variants of VERITAS 2.2 for fabrication: a full-featured chip and a more conservative variant with minimum changes (Figure 18). The conservative variant is now ready for submission, while the full featured VERITAS variant is integrated and in the process of validation. We anticipate submission later in August.

Summary:
- The combined US+MPE team have made good progress in demonstrating drain readout as viable option for the Athena WFI. Many fruitful measurement campaigns were carried out together.
- We identified key issues with the existing VERITAS 2.1 design and wrote the "final" VERITAS 2.1 datasheet.
- We studied, designed, simulated and implemented design improvements for the VERITAS 2.2 design.
- The new VERITAS 2.2 ASIC is expected to be submitted for production later in August 2018.

Figure 18: Layout of the conservative variant of VERITAS 2.2, now ready for manufacturing.
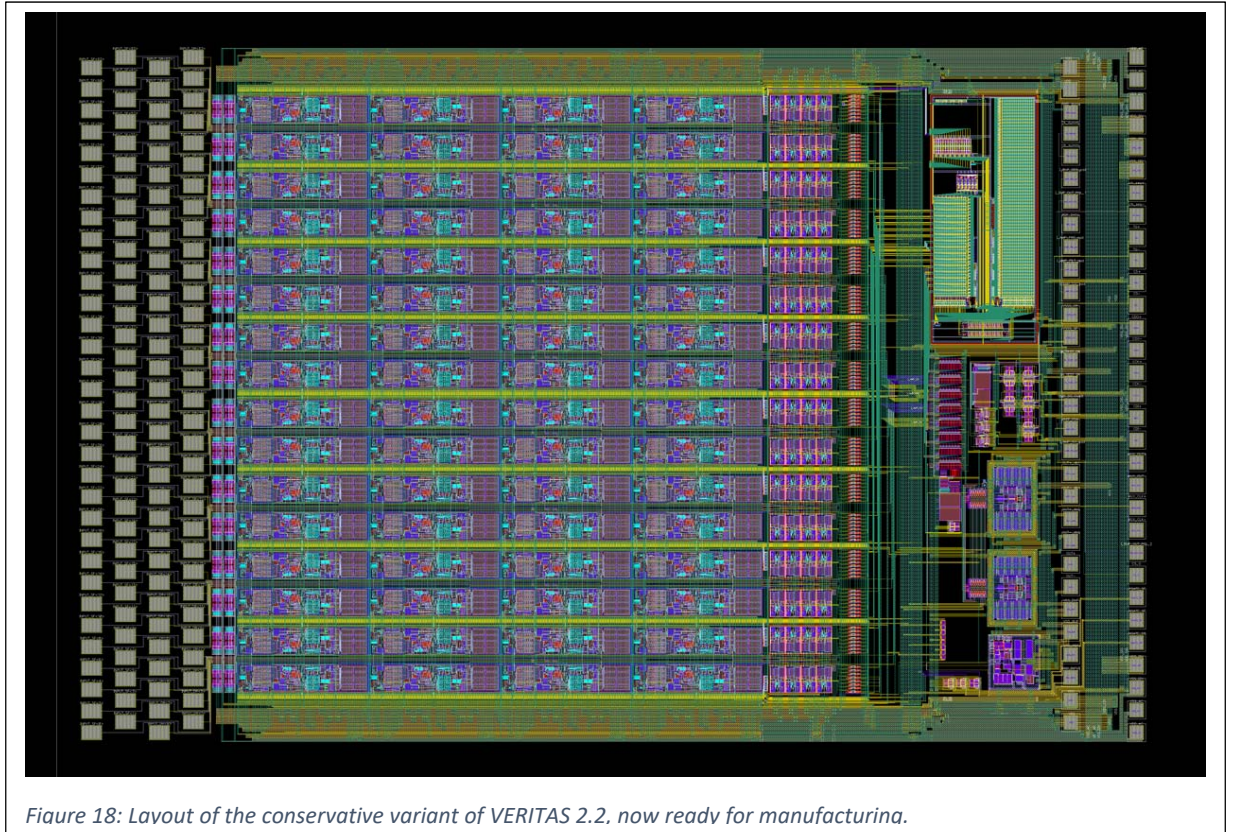
B) Exploring the WFI fast timing capability

Note: this work was primarily funded by other sources, not by this grant.

The Stanford/SLAC team has continued studies of the scientific drivers for high time resolution measurements, using either the separate fast detector or a window mode on the main WFI detector, in order to determine the capabilities required of the readout ASIC.

In particular, work has focused on X-ray reverberation studies of the immediate vicinities of black holes, in particular to study the structure of the inner regions of accretion flows and of the putative coronae that produce the intense X-ray continua emission in these sources. X-ray time delays around supermassive black holes in active galactic nuclei (AGN) of ~100s have been measured with XMM-Newton, corresponding to the light travel time between the highly variable source of the continuum emission (the corona) and the accretion disc off which it is reprocessed. This enables the mapping of structures on scales of 2-10 r_g (where the gravitational radius $r_g = GM/c^2$ is the radius of the event horizon around a maximally rotating black hole). The equivalent light travel time across $1r_g$ for a 10 solar mass black hole is 50μs.

For Athena, conducting similar experiments around stellar mass black holes will be important in order to understand accretion physics across the mass scale, and to understand state transitions and the regulation of accretion and the output of black holes (which in AGN drives feedback) on long timescales, since state transitions occur on observable timescales.

X-ray Timing Simulations:

Simulations have been developed to assess the capabilities of Athena to detect variability and reverberation time lags over a range of interesting timescales, to assess whether it will be possible to detect X-ray reverberation from the innermost regions of X-ray binaries and how the detector readout characteristics will impact this measurement.

Random light curves are generated with realistic f^{-2} power spectra, representing the primary variability in the X-ray continuum. These are then convolved with an impulse response function to generate the reverberating light curve seen in the reflected X-rays from the accretion disc. In the simplest case, to assess the detectability of a time lag, this is a delta function representing a simple time shift. The primary and reverberating light curves are then scaled in count rate according to the expected flux from a realistic X-ray binary (Cygnus X-1, observed in the low hard state when X-ray reverberation is expected to be the most significant - $7x10^3$ ct s^{-1} in each of the 0.3-1.0 and 1.0-4.0 keV energy bands between which reverberation is seen, with the reduced 119.0 cm mirror radius). The flux according to each light curve is then spread over the detector pixels, binned according to the detector readout frames and then Poisson noise is applied by drawing the photon count in each time bin from a Poisson distribution with a mean corresponding to the value of the original light curve.

Once the continuum-dominated and reverberating light curves were simulated, their Fourier transforms and cross spectra were computed in the same manner as for real observations, from which the lag spectrum is produced and reverberation is measured.

Work is now underway to integrate the simulation of X-ray reverberation with the SIXTE simulator package in order to perform full end-to-end simulations including the optics and detector readout process. There are, however, some unfortunate limitations in SIXTE in that it is not currently possible to input source light curves in which there are time lags between X-ray energy bands; thus it is necessary to simulate the initial list of photons that are to be detected in full (with sufficient time resolution) rather than allowing SIXTE to generate photons from a source model.

Detectability of time lags and the importance of timing resolution:

Initial simulations revealed that Poisson noise is the limiting factor in detecting rapid X-ray reverberation on gravitational-radius scales in X-ray binaries. For the default (146.9 cm radius) mirror configuration and 10µs time binning, the shortest lag that can be (just) recovered in a Cygnus X-1 LHS-like source is 100µs ($2r_g$), while 250µs ($5r_g$) is the shortest lag that is clearly detected (250±50 µs) over a broad range of Fourier frequencies. Reducing the Athena mirror radius to 119.0cm would have a substantial impact on the soft X-ray count rate (to which there is a large contribution from the outer mirror shells). The shortest clearly detectable lag for a Cygnus X-1 low/hard state-like source would then become 1000µs ($20r_g$). In order to recover the accuracy of lag measurements achieved with the larger mirror area, sources 1.25x brighter would be required. Fluxes this bright (or brighter) are frequently observed in some nearby X-ray binaries during outburst states. Thus, while the reduced mirror area would clearly impact reverberation science in the more common low-hard states of binary sources, high-impact

science probing the immediate vicinity of stellar mass black holes could still be carried out during outbursts and state transitions.

Our simulations also underscore the importance of the detector having high time resolution (i.e. short readout frames such that photons can be counted into short time bins). The time binning of the light curve limits the shortest lag that can be developed, with a bin size longer than the intrinsic time lag causing a systematic overestimate in the lag. In order to be confident of a lag measurement, it is necessary to accumulate light curves with time binning (and hence detector readout frames) a factor of a few shorter than the shortest time lag that is to be measured.

Detector readout effects:

When performing high resolution X-ray timing experiments, variability and time lags are being measured on timescales comparable to the readout frame time of the detector, hence the detector readout process could have a significant impact on experimental results. While previous X-ray timing experiments have integrated over many readout cycles, readout timescales now become important, particularly if the count rates are sufficiently high that a significant number of photons arrive on pixels while they are being read out, causing misfit events (where they may appear in either the current or the next frame with altered energy, described by the 'weighting function'). Full end-to-end simulations that are being developed with SIXTE will incorporate these effects in addition to pile-up limitations as the count rate per pixel becomes high, to assess the importance for high-resolution timing.

In the DEPFET arrays, rows are read out sequentially, so while, for example, the full frame time of the fast detector may be 80μs, individual rows are read out in 2.5μs with the readout shifting to the next line 2.5μs later. This results in the time binning on successive lines of pixels being offset from one another by the line readout time rather than the frame time. Our initial simulations have demonstrated that when lines are read out successively, while the full frame time may be 80μs, timing information is retained on the line readout timescale of 2.5μs and that in some circumstances, with high signal-to-noise per line, time lags can be measured with a shorter effective time resolution corresponding to the row time, not the frame time. The next steps will be to determine the optimum algorithm for reconstructing the maximal timing information from the rolling shutter.

C) Towards cleaner Athena data with machine learning

Note: this work was primarily funded by other sources, not by this grant.

Our Stanford team has begun to explore the potential of machine learning algorithms for on-board cleaning of the Athena WFI data of particle-induced background events. Key considerations here are the limitations of on-board hardware, the speed with which filtering decisions must be made (of order milliseconds) and the sparsity of the data.

For the current generation of X-ray satellites carrying CCD detectors in low orbits, most data can telemetered to the ground, where they are cleaned of background events using simple 2x2 or 3x3 pixel pattern recognition algorithms. While this basic cleaning is adequate for most current purposes, it will be insufficient for the study the faintest, most diffuse sources with Athena. Moreover, given its large (1024x1024) array of DEPFET active pixel sensors, their fast readout, and the high, particle-rich orbit of Athena (L1 or L2), the primary event filtering for the WFI will need to be done on-board and in real-time (the raw data rate would by far exceed the feasible telemetry rate). We anticipate that fast, effective particle background rejection should in principle be achievable using machine learning.

Stage 1: proof of principle

We will first demonstrate the applicability of machine learning algorithms, specifically image recognition neural networks, to the problem of background detection in X-ray images, based upon simulations of how charged particles will interact with the Athena WFI detector. These simulations have been developed by collaborators at The Open University (UK) and MPE (Germany) utilizing the GEANT4 code, a Monte Carlo code widely used in particle physics and space science that tracks incoming cosmic rays and the energy they deposit as a function of position (this translates to the brightness of pixels in an image). An image is produced each time the detector is read out, in this case once every 5ms.

We will use the GEANT4 simulations to train and assess the capability of neural networks to recognize the pixel patterns produced by particles, as opposed to those from bona fide X-rays. Charged particles will typically deposit energy across many adjacent pixels as they travel through the detector, while individual X-ray photons will illuminate either single or adjacent pairs (or rarely adjacent groups of three or four pixels). While existing algorithms for cleaning X-ray data distinguish particle detections from X-rays based simply upon the number of adjacent pixels illuminated, secondary interactions of particles can produce small 'islands' of illuminated pixels surrounding the primary that can masquerade as X-ray photons. To obtain the lower background levels needed for future missions like Athena, we propose to use machine learning algorithms that consider the whole image to associate these secondary detections with the primary detection of the particle.

Stage 2: optimization to meet hardware requirements:
While our initial proof-of-principle studies will use out-of-the-box convolutional neural network algorithms, these will likely not achieve the speed required when using the limited computational resources available in the Athena SPM. The second stage of our plan will therefore be to develop algorithms that can run quickly on limited CPU and FPGA resources. While many image recognition algorithms were developed to run on photographic images, due to the short time between WFI image frames, we will seek to take advantage of the fact that most of the pixels in any given image will record zero signal (only a handful of photons and particles hit the detector every 5ms). We propose to develop convolutional neural networks using sparse matrix algorithms to achieve the required speed-up and compression of the network. We hope to engage with other Stanford data science experts and the broader US Athena WFI team to advance this research. Our eventual goal would be the inclusion of this processing capability aboard the Athena SPM and potentially other future missions.

V) Travel
Various members of the US WFI team attended the following meetings related to Athena science and/or technical status/interfaces during the reporting period:

1. **Oct. 2017: Athena WFI Consortium meeting, Warsaw, Poland.** This meeting was combined with ICPU (Instrument Control and Processing Unit) Technical Meeting #3 and a meeting of the WFI Background Working Group. All parties were represented.
2. **Feb. 2018: Athena ICPU Technical Meeting #4, Garching, Germany.** Discussed ICPU design and internal interfaces. PSU and SwRI present for US SPM.
3. **March 2018: HEAD meeting, Chicago, IL.** Presented WFI contributions to Athena at special meeting of the High Energy Astrophysics Division (PSU, MIT, SAO).
4. **March 2018: US WFI Consortium meeting, Baltimore, MD.** Entire US WFI team met to review status and discuss our inputs to SPM Assessment Criteria draft document from MPE.
5. **April 2018: Athena WFI Consortium meeting, Garching, Germany.** This meeting was combined with ICPU (Instrument Control and Processing Unit) Technical Meeting #5. Entire team represented.
6. **June 2018: SPIE Astronomical Telescopes and Instrumentation meeting, Austin, TX.** Presented status of SPM board design, Transient Analysis Module and Background Analysis Module.
7. **June 2018: Athena Science Working Group 2.6 meeting, Nijwegen, Holland.** PSU attended this working group meeting called to discuss Athena mission contributions to transient science in general, and to the era of multimessenger astrophysics in particular. Presented WFI SPM capabilities in on-board transient source detection.
8. **July 2018: Athena ICPU Technical Meeting #6, Graz, Austria.** Discussed ICPU design and internal interfaces. PSU present for US SPM.
9. **Various: multiple trips by Sven Herrmann to MPE** to assist with the Veritas 2 ASIC design and debugging.

Superconducting Antenna-Coupled Detectors for CMB Polarimetry with the Inflation Probe

Prepared by: James J. Bock (JPL, California Institute of Technology)

Summary

We are developing advanced antenna-coupled superconducting detector-array technology for the NASA Inflation Probe (IP), a future satellite dedicated to comprehensive measurements of Cosmic Microwave Background (CMB) polarization in NASA's Physics of the Cosmos (PCOS) Program. This Strategic Astrophysics Technology (SAT) project will extend the demonstrated frequency range of antennas down to 30 GHz, and develop dual-band antennas that offer larger wafer formats with a higher density of detectors, a valuable resource in a 100-mK space-borne focal plane.

Antenna-coupled detectors have the requisite attributes – sensitivity, frequency coverage, and control of systematic errors – called for in community studies of space-borne CMB-polarization experiments. The arrays provide integral beam-formation, spectral-band definition, and polarization analysis; and scale to operate over the wide frequency range of 30 to over 300 GHz required to remove galactic foregrounds at near-background-limited sensitivity. The devices have rapid response speed and 1/f noise stability for slow-scanning observations without requiring an additional level of signal modulation.

Our program rapidly infuses new detector technology into scientific observations, the fastest way to learn about real-world performance in demanding applications. Simultaneously, the program develops aspects of the technology uniquely required for space-borne operations. We are expanding the frequency coverage of the antennas, and applying these devices to improved foreground separation between the galaxy and the CMB. We are developing broadband antennas to better exploit full access to the electromagnetic spectrum in space. We are expanding the development of focal-plane modules that integrate detectors and readouts into a package for large focal planes, and fielding these devices in active CMB experiments to determine scientific performance in representative environments. We are furthering our measurements of cosmic-ray susceptibility, based on our experience with the detectors on the European Space Agency (ESA) Planck satellite. Finally, we are starting to integrate arrays from larger 150-mm wafers into focal plane modules. These modules integrate the sensor and readout in a single package that can be individually tested, and then assembled into a full focal plane. As the readouts are integrated behind the detectors, they can be tiled into an arbitrarily large focal plane.

This two-year grant began in January 2018, and includes Jeff Filippini at the University of Illinois Urbana-Champaign (UIUC); and Krikor Megerian, Hien Nguyen, Roger O'Brient, Anthony Turner, and Alexis Weber at JPL. The program actively engages postdocs and students at Caltech, including Bryan Steinbach, Jon Hunacek, Howard Hui, and Sinan Kefeli. The students characterize the devices at cryogenic temperature, and then use the arrays in astrophysical measurements of CMB polarization.

Scientifically, the devices have led the way in state-of-the-art (SOTA) CMB measurements from ground-based and balloon-borne observations. This year, the BICEP/Keck Array collaboration published the first results incorporating measurements in three spectral bands, 95, 150, and 220 GHz from data obtained through 2015, which provide the best constraints on inflationary polarization signal to date. The new data from 220 GHz now measure polarized dust emission with the same sensitivity as the Planck satellite in its most dust-sensitive band at 353 GHz. This important

development enables sub-orbital experiments to ultimately surpass the foreground sensitivity from available space-borne data in order to reach new constraints on the Inflationary birth of the universe. CMB polarization data have now surpassed CMB temperature information for constraining the amplitude of the Inflationary gravitational-wave background, a transition predicted in the 1990s. The BICEP/Keck Array collaboration is currently analyzing data up through 2017 that offers approximately five times more data at both 95 and 220 GHz from the 2015 release, another significant step forward. Based on the performance of the 270-GHz focal plane in 2017, which demonstrated that atmospheric noise does not substantially degrade polarization measurements at this frequency, we fielded an improved 270-GHz focal plane in 2018 that is currently taking data.

The rapid improvement in sensitivity at 95 GHz will soon drive the need for improved measurements of galactic synchrotron emission at low frequencies, which are presently limited by the sensitivity of available space-borne data from the Planck and WMAP satellites. Our SAT program is thus now turning to the development of new low-frequency 30 and 40-GHz arrays and modules for 150-mm wafers. These large-format, low-frequency arrays promise to rapidly overtake space-borne data to provide the new levels of foreground removal needed to improve constraints on cosmic Inflation. Furthermore, as low-frequency devices are physically large and consume precious focal plane area in the IP space mission, we are developing a dual-band design to simultaneously operate at 30 and 40 GHz, increasing areal efficiency.

In January 2015, the Suborbital Polarimeter for Inflation Dust and the Epoch of Reionization (SPIDER) balloon experiment flew with six full focal planes operating at 95 and 150 GHz. The detectors performed well in the scientific environment closest to space, with low photon backgrounds, slow-scanned observations, and a challenging cosmic-ray environment. The next flight of SPIDER is planned for the 2019/2020 season and provides an opportunity to test improved RF shielding designs and further our studies of cosmic-ray susceptibility.

Background

The importance of CMB-polarization research has been recognized in national reports including the 1999 National Academy Report; the 2001 Decadal Survey; and the 2003 National Research Council (NRC) report, "*Connecting Quarks with the Cosmos.*" In 2005, the Task Force on CMB Research stated that its first technology recommendation was "*technology development leading to receivers that contain a thousand or more polarization-sensitive detectors,*" and that *"highest priority needs to be given to the development of bolometer-based polarization sensitive receivers.*" The Astro2010 decadal report endorsed a CMB technology program of $60M-$200M, its second-ranked medium initiative for space. In addition, the decadal report states the amount could be increased to $200M following a mid-decade review of the state of CMB-polarization measurements. The CMB Technology Roadmap ranked detector arrays as its highest CMB-technology priority, recommending a program that takes maximum advantage of operating the arrays in sub-orbital and ground-based CMB-polarization experiments.

A new definition study of the IP, the Probe of Inflation and Cosmic Origins (PICO), was recently initiated, one of the NASA Probe mission studies. PICO (Fig. 1) builds on previous studies prior to the 2010 Decadal Review that developed the basis for space-borne CMB-polarization measurements, incorporating high-sensitivity detector arrays as the key technology, operating over a wide range of frequencies to accurately measure and remove polarized galactic foregrounds. The detector system must demonstrate extreme 1/f noise stability, forward-beam definition with stray-light immunity, radio-frequency (RF) and magnetic shielding, excellent spectral-band and time-constant matching, and cosmic-ray insusceptibility. PICO incorporates approximately 13,000 detectors in 21 broad bands ranging from 20 to 800 GHz. This large focal plane is constructed from 31 focal plane modules, assuming antenna-coupled TES bolometer sub-arrays on 150-mm wafers, coupled to integral Superconducting-QUantum-Interference-Device (SQUID) readouts.
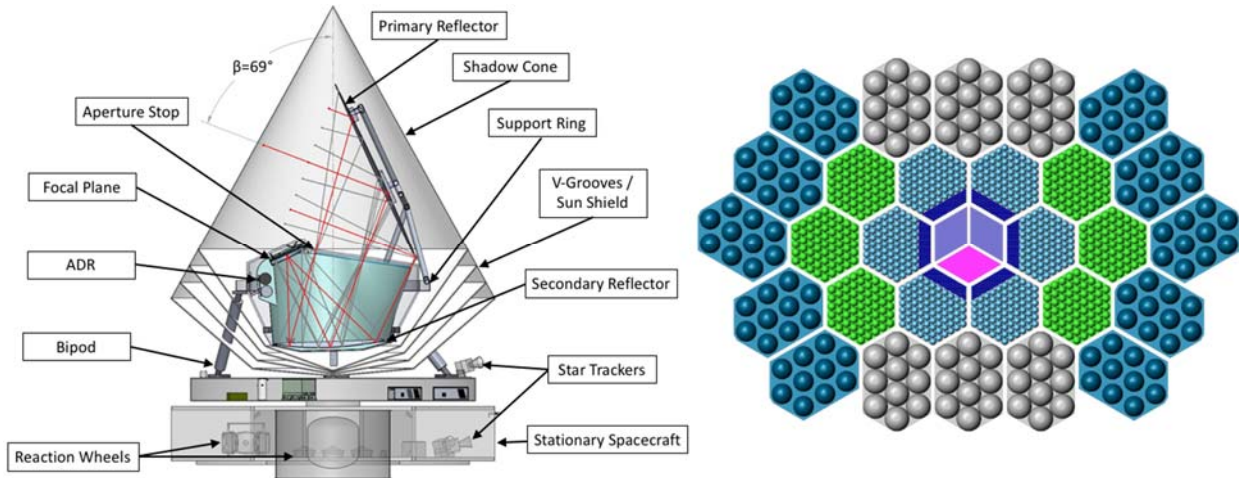
Fig. 1. Left: *The PICO Probe mission study [1] of the IP, designed to deeply map the full sky in polarization in multiple bands with unprecedented sensitivity to Inflationary polarization (ADR, adiabatic demagnetization refrigerator). The mission observes the sky from an L2 orbit with a passively-cooled 1.4-m telescope, using a spinning and precessing scan strategy that provides redundant all-sky coverage with a large modulation of focal-plane angle that is ideal for polarization studies.* Right: *The PICO focal plane with 13,000 detectors in 21 spectral bands from 20 to 800 GHz. The design uses multi-frequency antennas in focal plane modules with integral readouts.*

The IP will measure CMB polarization over the entire sky to cosmological and astrophysical limits. The CMB is thought to carry a B-mode polarization signal imparted by a gravitational-wave background produced by the Inflationary expansion $\sim 10^{-32}$ seconds after the Big Bang. The Inflationary polarization signal is sensitive to the energy scale and shape of the Inflationary potential, and can be clearly distinguished from polarization produced by matter-density variations due to its distinctive B-mode spatial signature. A detection of the Inflationary polarization signal would do more than just confirm Inflation — the amplitude of gravitational waves depends on the model and energy scale of Inflation, so detection would distinguish between models and constrain the physical process underlying Inflation. Such a measurement has profound implications for cosmology and bears on the current frontiers of fundamental physics: the union of general relativity and quantum mechanics, string theory, and the highest accessible energies.

The IP will also map the CMB-polarization pattern produced by gravitational lensing. Intervening matter between us and the surface-of-last-scattering slightly distorts the background CMB polarization, imparting a B-mode signal that peaks at arcmin angular scales and probes the evolution of large-scale structure, which is sensitive to neutrino mass and dark energy. The CMB lensing signal is related to the projected gravitational potential of this matter, and provides a powerful combination with dark-energy surveys such as baryon acoustic oscillations and weak lensing.

Antenna-coupled Transition-Edge-Sensor (TES) bolometer arrays (Fig. 2) are a scalable, planar focal-plane architecture that coherently sums an array of individual slot antennas with a microstrip feed network, controlling the phase and electric-field amplitude distributed to each slot. The planar antenna enables customized shaping of the detector beam-pattern for controlling detector illumination on critical optical surfaces. The antenna operates in two polarizations: an array of horizontal slots couples to one detector, and an interleaved array of vertical slots couples to another. The spectral band is defined by a three-pole RF microstrip filter. Power from the antenna is deposited in a meandered Au resistor on a thermally isolated bolometer, detected by a Ti/Al TES detector and read out by a multiplexed SQUID current amplifier. As shown in Fig. 2, this technology has now been demonstrated in scientific observations in spectral bands centered at 95, 150, and 220 GHz. A fourth band at 270 GHz has been developed under the SAT program and started first-light observations in 2017.
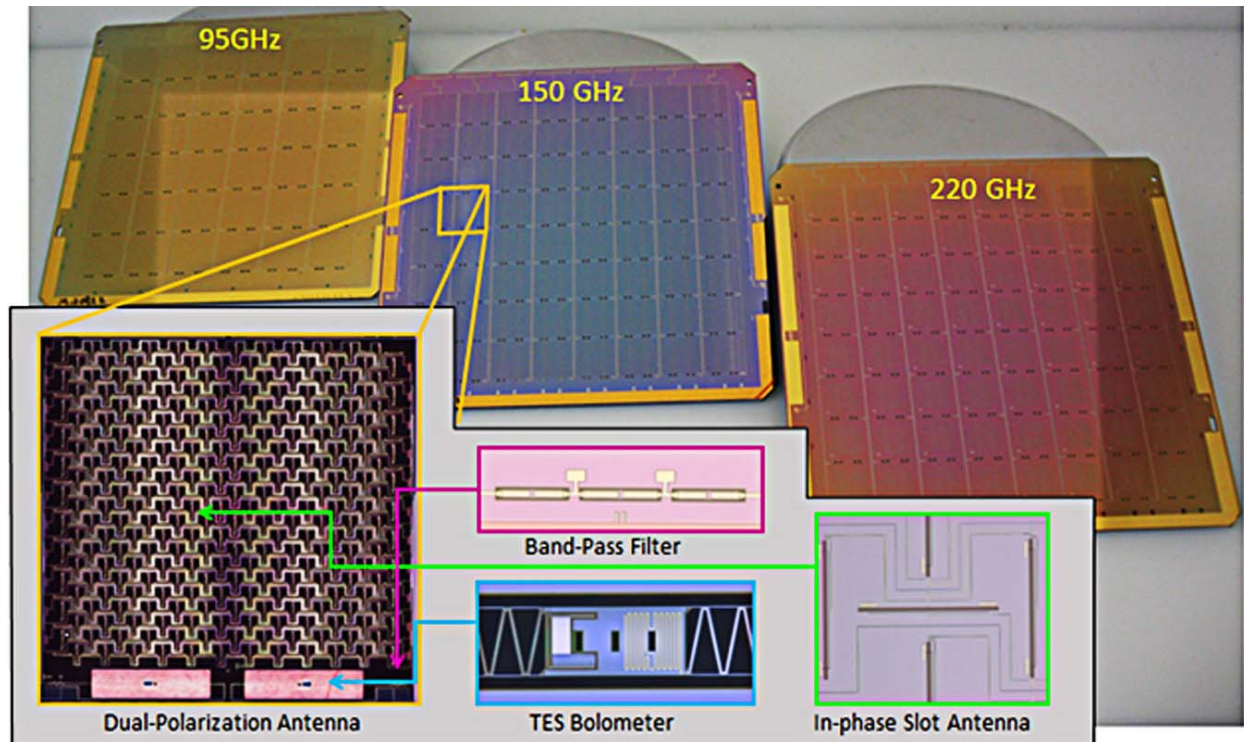
Fig. 2. *Focal-plane array wafers designed for operation at 95, 150, and 220 GHz. Each wafer is based on planar dual-polarization antennas consisting of an array of slot antennas coherently combined with a feed network. The output of the antenna passes through a lithographed band-defining filter and terminates in a resistive meander located on an island thermally isolated on micro-machined silicon-nitride beams. Power deposited on the bolometer is sensed with a voltage-biased TES bolometer readout with multiplexed SQUID current amplifiers.*

Planar antennas are entirely lithographed and avoid coupling optics such as feedhorns or hyper-hemispherical lenses, ideal for a low-mass 100-mK focal plane. The devices can cover the wide range of frequencies by scaling the antenna with wavelength and keeping the detector element essentially unchanged. The antennas demonstrate excellent polarization properties and the lithographed filters provide reproducible control of the spectral band. The Ti TES detectors give predictable noise properties and low-frequency noise stability appropriate for slow-scanned observations from space.

Current State of CMB Polarization Measurements

In recent years, CMB-polarization measurements have broken new ground in placing constraints on a background of gravitational waves produced in some models of Inflation. Antenna-coupled TES bolometer-array technology is ideal, because the architecture scales in frequency, and we have developed science-grade arrays in three frequency bands (Fig. 2). In Fig. 3 we show the latest scientific measurements from the BICEP2/Keck experiment obtained at these three frequencies from data up to 2015 [7]. The 220-GHz data in this paper have comparable sensitivity to the Planck satellite in constraining polarized interstellar dust emission (five times more data have since been collected through 2017 at this frequency). The maps demonstrate SOTA sensitivity, while serving as valuable tests for controlling systematic errors. Indeed, the sensitivity at 150 GHz, below 50 nK in a square degree, is comparable to the sensitivity expected for the IP satellite, so controlling systematic errors at this sensitivity is directly relevant. However, instead of reaching this depth in a small region in a single band, the IP will map the entire sky in multiple bands at this sensitivity.
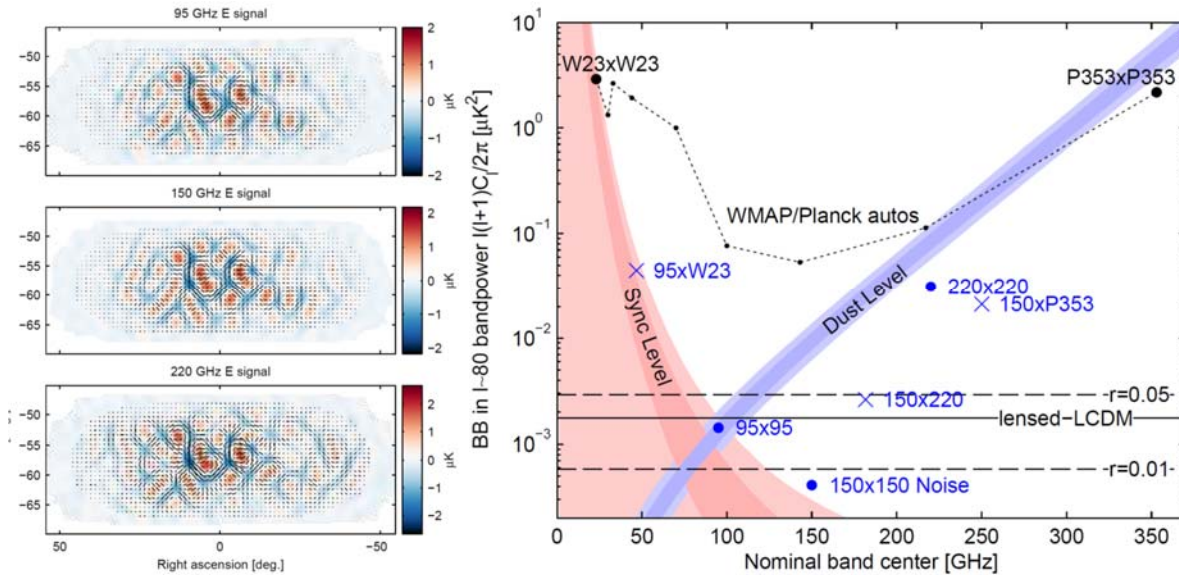
Fig. 3. Left: *New CMB maps (Dec, declination; RA, right ascension; deg, degrees; RMS, root mean square) from BICEP-Keck using data through 2015. The maps show E-mode polarization both in amplitude (color) and polarization (length of bars proportional to amplitude, indicating direction). A common pattern is clearly reproduced in all three frequencies even through the signal level is faint at ~1 μK.* Right: *Polarized signals (bands) and statistical B-mode polarization sensitivity (data points) in a multipole bin centered at ℓ = 80 where the Inflationary polarization peaks. The plot is given in units of CMB temperature sensitivity, so horizontal lines show signal levels for lensing and inflationary polarization at amplitudes of r = 0.05 and 0.01. Note the high-sensitivity data point for the 150×150 spectrum. Galactic polarized foreground emission fitted from the data is shown in blue (interstellar dust) and red (synchrotron). While this plot shows statistical sensitivity, the overall errors on Inflationary polarization are dominated by measurement uncertainty on galactic dust, which is rapidly improving thanks to technology advances at 220 and 270 GHz from the SAT program. New measurements will soon be needed to constrain galactic synchrotron radiation, which will become the dominant uncertainty as the 95 GHz sensitivity improves. Synchrotron emission is currently undetected in this low-foreground field in WMAP and Planck data, but new data at 30 and 40 GHz enabled by SAT technology can improve on current sensitivity by more than an order of magnitude in a single observing season. Figures taken from reference 7.*

Objectives and Milestones

This SAT program advances the detector attributes needed for space-borne observations, specifically, developments related to frequency coverage, wafer formats, focal-plane packaging, process monitoring, TES development, and RF and cosmic-ray susceptibility. The tasks for our 2018 SAT program build on current antenna-coupled detector technology to address specific challenges for a space mission as follows:

- Extend the frequency range to science-capable 30 and 40-GHz arrays on 150-mm wafers;
- Develop dual-band 30/40-GHz devices with broad-band antennas;
- Develop focal-plane modules for 150-mm wafers with high-density circuits;
- Develop a resonator chip for tracking propagation loss in fabrication process;
- Develop and test a filter to mitigate radiated RF power;
- Develop a uniform 100-mK TES process; and
- Measure cosmic-ray particle susceptibility in 100-mK arrays.

Progress and Accomplishments

Focal-plane technology developed under this SAT program continues to make strong progress in demonstrating scientific performance. BICEP3 operates 20 focal-plane modules, similar to the modular

focal planes planned for the IP shown in Fig. 1b. This technology was developed under the SAT program, and the modular design enables component-wise development and testing. New antennas designs were extended to operate at higher frequencies. Antennas operating in a new observing band at 270 GHz were scientifically demonstrated in the Keck Array in 2017. This extended frequency coverage enables new measurements on polarized emission from galactic dust, an important foreground. New scientific results were presented (see reference 7 and Fig. 3) using the first polarized measurements at 220 GHz, with antenna technology originally developed through the SAT program.

This year, we completed fabrication of science-ready 40-GHz sub-arrays, with device parameters optimized for optical loading from a ground-based site. The wafer has been integrated with a prototype module for 150-mm-diameter wafers (Fig. 4) and is now being tested. The module incorporates the detector wafer, the multiplexed SQUID readout, an anti-reflection wafer, and a $\lambda/4$ optical back-short in a compact package that uses the space behind the wafer to maximize areal packing. The design employs a flexible, dense Si circuit board that enables it to work with a variety of detector formats. The module was previously integrated with a prototype 40-GHz sub-array and passed thermal and mechanical tests. The 150-mm wafer fabrication process continues to improve, and we recently incorporated changes to the Nb patterning and TES contacts, steps that will increase device yield. In the coming test, the module will be characterized with the 40-GHz sub-array for noise and magnetic shielding.
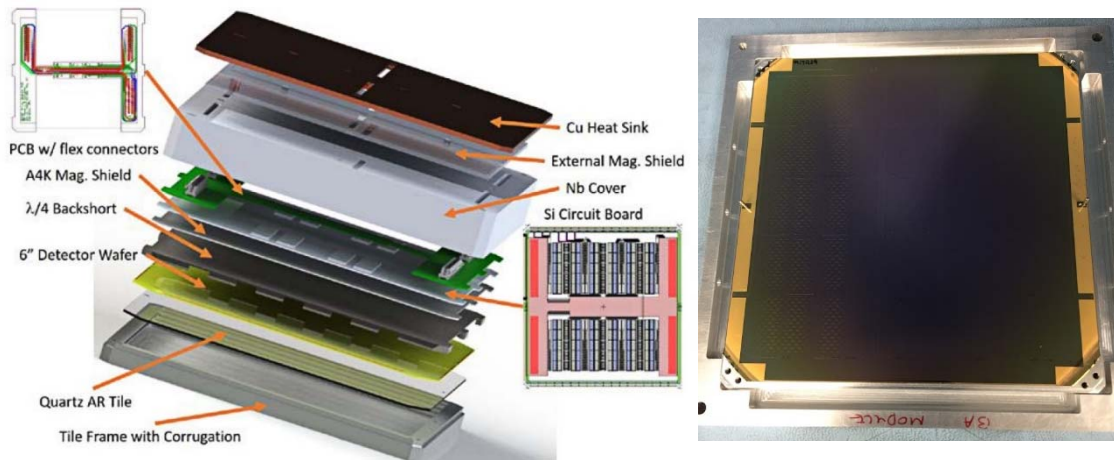

Fig. 4. Left: *Module design for accommodating arrays from 150-mm-diameter wafers. The design employs a silicon circuit board for a dense design, routing between the detector wafer and Time Division Multiplexing (TDM) SQUID chips with aluminum traces. The silicon wafer interfaces to a conventional connectorized printed circuit board (PCB) for bias lines, row address, and SQUID signal outputs. The row address lines route through 10 columns of N-chained base-11 SQUID chips. This allows us to flexibly allocate channels in multiple configurations such as 35, 95, and 150 GHz with 64, 288, and 648 channels.* Right: *Prototype module developed and tested with a 150-mm wafer 40-GHz sub-array for electrical and thermal compatibility. A science-compatible 40-GHz sub-array, with device parameters tailored for expected optical loading from a ground-based site, is currently in fabrication for testing with the module.*

We also developed two new antenna designs for extending to lower frequencies, a 30-GHz antenna and a dual-band 30/40-GHz antenna. The 30-GHz antenna and bandpass filter designs (Fig. 5) are scaled from higher frequencies. However, the long wavelengths presented a challenge for terminating the antenna on the TES bolometer. We developed a new transition section between the Nb stripline to the Au absorber, made with alternating sections of Nb and Au, to minimize reflections. This approach is also being adapted for the 40-GHz and dual-band designs. The dual-band design (Fig. 6) incorporates a broad-band antenna that we originally developed and tested for 200-300 GHz. The antenna leads to a diplexer that splits the band between the two frequencies, and bandpass filters for both bands. Operating at two frequencies simultaneously, the device has 4 detectors per pixel instead of 2. We extensively modeled the frequency response and the antenna pattern (Fig. 6). Both designs are complete and ready to proceed to fabrication on 150-mm diameter wafers. Both designs

will be produced as sub-arrays that are drop-in-compatible with the new focal-plane module design (Fig. 4). In fact, the focal plane module edge corrugations were carefully designed and optimized for the broad-band performance needed for the dual-band antenna.
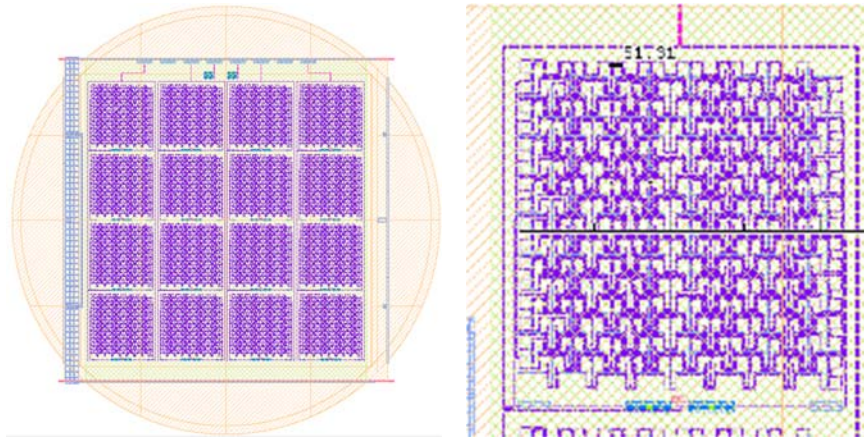
Fig. 5. Left: *Wafer design for a 30-GHz sub-array on a 150-mm diameter wafer. 30 GHz represents a new frequency, the lowest yet developed for planar antennas.* Right: *View of a single dual-polarized pixel using planar antennas in vertical and horizontal antennas, 3-pole band-pass filters, and transition-edge superconducting bolometers.*
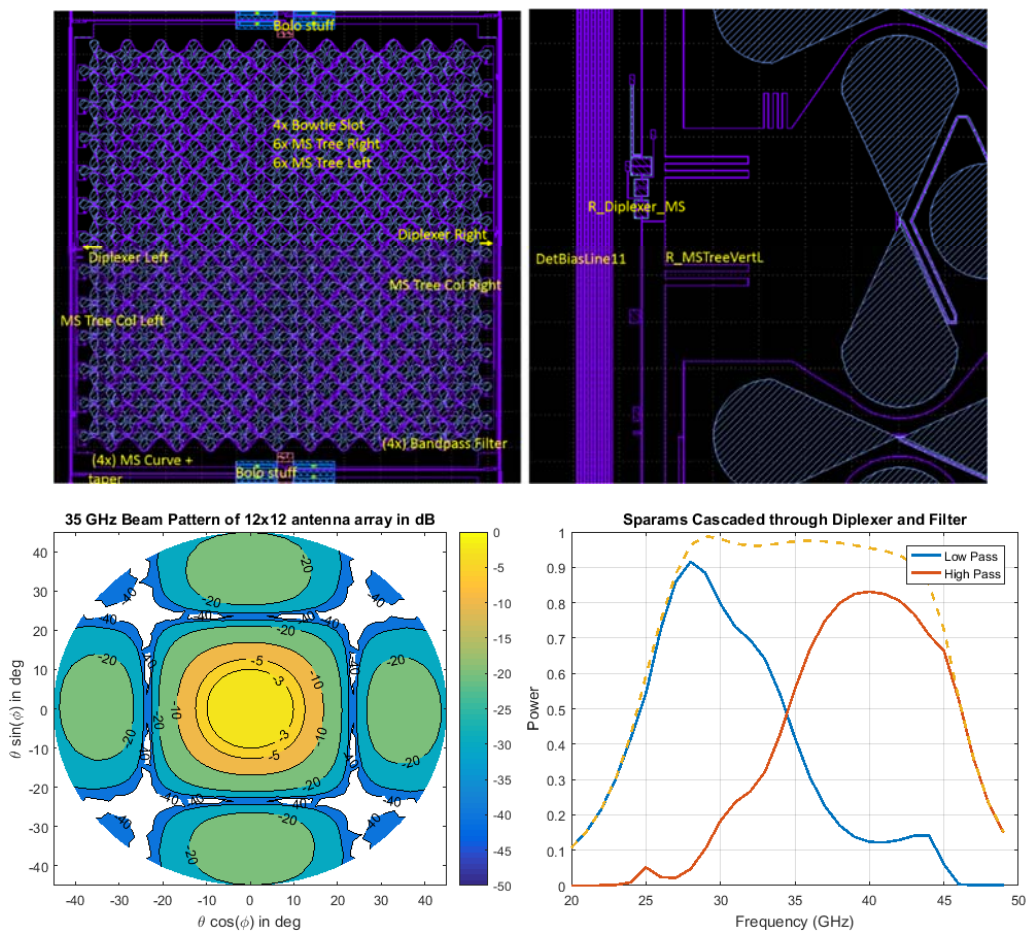
Fig. 6. Top left: *Broad-band antenna pixel for dual-band 30/40-GHz operation in two polarizations. The output of the broad-band antenna goes to two diplexers, and then bandpass filters and detectors.* Top right: *Detail of the diplexer design at the left edge of the antenna.* Bottom left: *Modeled antenna beam pattern at 35 GHz, showing a*

characteristic 2-D tapered sinc pattern. This antenna is intended for aggressive packing with a cold telescope, and couples to the aperture at the -5 to -10 dB level. Bottom right: *Modeled spectral response of the antenna, diplexer, and bandpass filter combination that provides high efficiency over the two spectral bands. The sum of the 30-GHz and 40-GHz response is given by the orange dashed line. The bands can be further separated by using more poles in the diplexer, which may be desirable depending on the instrument design.*

We previously developed an RF-mitigation filter consisting of a band-pass mesh filter placed over the sub-array. The filter uses an inductive mesh layer to reduce RF coupling to the focal-plane detectors through the optics, a problem encountered in the SPIDER flight. The filter was tested to show high in-band transmission and strong RF rejection. The filter has been integrated into a SPIDER focal plane and is currently being tested at system level in preparation for the upcoming 2019/20 Antarctic long-duration balloon (LDB) flight.

Response to particle radiation is a critical concern for space technologies, due to the high flux of cosmic rays present outside the atmosphere. This is a particular concern for bolometric detectors, posing a particular challenge to the analysis of Planck-HFI data. As part of our efforts to develop space-qualified antenna-coupled TES arrays, we have thus begun a program to characterize the response of these devices to particle radiation, and introduce any needed mitigations. This program is led by the Filippini group at the University of Illinois at Urbana-Champaign. We first tested 300-mK arrays in the laboratory and analyzed cosmic-ray events from the 2015 SPIDER balloon flight. More recently, we began extending this work to 100-mK devices.

SPIDER, a CMB polarimeter, completed a successful 16-day LDB flight over Antarctica in January 2015. SPIDER's six cameras each supported four JPL antenna-coupled TES wafers, for a total of 2400 TES channels. At high altitude (36 km) and latitude, SPIDER encountered a cosmic-ray flux very similar to that in space at ~GeV energies and above, though suppressed somewhat at lower energies by Earth's magnetic field and a more favorable portion of the solar cycle.

Figure 7 shows the spectrum of reconstructed energies from the cosmic-ray glitches seen in one 90-GHz receiver. The spectrum is in reasonable agreement with Monte Carlo simulations of cosmic-ray proton hits on the bolometer using the GEANT4 package. The low rate of coincidence between detectors (~5% of glitches) suggests that long-distance energy propagation within the shared wafer is not a critical issue. Cosmic-ray glitches show a common shape independent of energy, limited by the ~35 Hz cutoff of the readout's digital anti-aliasing filter. These glitches have had a negligible impact on SPIDER's science analysis.
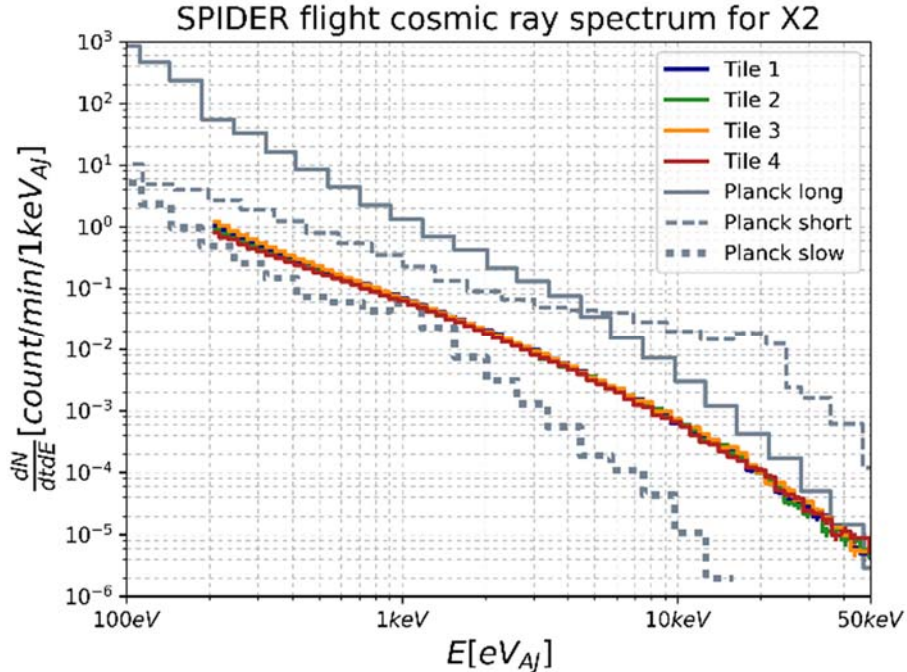
Fig 7. Reconstructed per-detector apparent energy spectrum for one SPIDER 90-GHz receiver. Identifiable glitches were seen about once every three minutes in each detector. Also shown are similar spectra for the various Planck-HFI glitch classes (from Catalano et al. 2014).

This year, we completed a custom test stand (Fig. 8) and exposed a full 128-TES SPIDER flight array, fully read out using SPIDER's time-division SQUID multiplexer system, to several collimated ^{241}Am radioactive sources, some targeting bolometers, and others targeting the wafer far from any bolometer. These sources yielded hits from both alpha particles and secondary electrons ejected from the collimator; GEANT4 simulations indicate that these closely mimic typical energy depositions from cosmic ray hits to the wafer and bolometer, respectively. Coincidence rates during this full-array test are very low, with no obvious evidence of response to wafer hits. Studies of data acquired at higher sampling rates (Fig. 8) show no long recovery time constants. These data have also enabled detailed comparisons with a more complete time-domain model we have developed of the SPIDER TES and readout system.
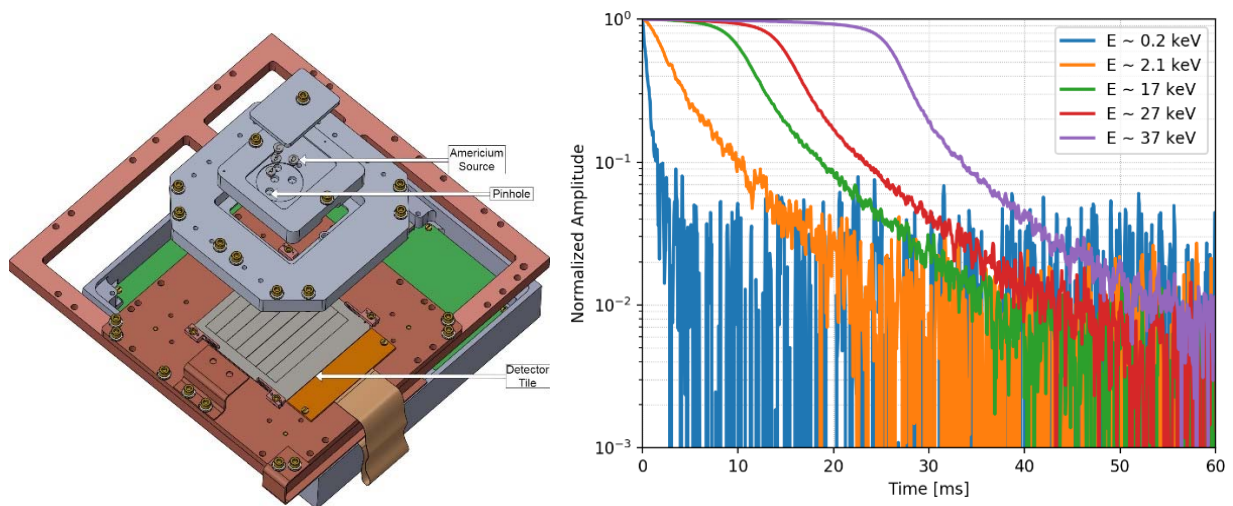
Fig 8. Left: Rendering of the UIUC particle test stand. A single SPIDER flight tile is mounted beneath a replaceable collimating source housing and read out by SQUID multiplexer electronics housed below. Right: *Measured glitch*

shapes for events of various reconstructed energies. TES saturation is visible for high-energy events, but none show decay time constants longer than ~10 ms.

In sum, results for 300-mK TES arrays are encouraging: cosmogenic glitch rates appear manageable, recovery times are short, and no long-distance energy propagation or response to wafer hits is apparent. Our program of radioactive source tests informed by Monte Carlo simulations have produced a largely consistent picture, and would be a productive and low-cost path for future space bolometer systems.

As with Planck-HFI, future space-based CMB bolometers are likely to operate at or below 100 mK for improved sensitivity. Though much of the 300-mK experience above should carry over, there may be important differences due to, e.g., poorer thermal links among array components. Thus, UIUC is pursuing a similar test program of 100-mK-optimized devices, evaluating options for purchase of an appropriate 100-mK cooling system this calendar year.

Path Forward

Table 1 shows the project's milestone schedule, and status. We anticipate important performance tests of the 150-mm focal plane module in the coming test run to validate its scientific performance with a 40-GHz sub-array. The new 30-GHz and dual-band 30/40-GHz devices are proceeding to fabrication. These low-frequency devices have an immediate scientific application, constraining polarized synchrotron emission in deep CMB measurements, and are directly relevant to the area-efficient and modular focal planes needed for the IP. We are continuing to test technical mitigations for RF and cosmic-ray susceptibility extending to 100-mK base temperature. All of these technologies developed by the SAT program are applied in cutting-edge CMB experiments that provide system-level demonstrations in the most representative environments possible, showing end-to-end suitability to demanding scientific standards for performance and systematic error control.

Topic	Milestone	Schedule and Status
Diplexed 30/40-GHz Focal-Plane Arrays	**30-GHz Arrays** Demonstrate antennas for the 30-GHz frequency band to test operation at low frequencies	**March 2018 – October 2018** Design completed, starting fabrication
	Wide-Band Antenna for 25 – 45 GHz Demonstrate wide-band antenna	**January 2018 – September 2018** Design completed, starting fabrication
	30/40-GHz Diplexer Demonstrate 2-band diplexer	**January 2018 – September 2018** Design completed, starting fabrication
	Dual-Band Antenna Performance Measure device spectral response and beams	**September 2018 – December 2018** Tests start when fabrication completes
	Dual-Band Science Performance Measure device Noise Equivalent (CMB) Temperature (NET) and scientific performance	**March 2019 – December 2019** Not started
Focal-Plane Modules for 150-mm Wafers	**Develop and Test Module** Determine electrical and thermal performance	**January 2018 – June 2018** Completed
	Science-Ready 40-GHz Sub-Arrays Develop arrays to integrate with module	**March 2018 – August 2018** Arrays done and ready for integration
	Science Systematics Determine noise and magnetic shielding performance of integrated assembly at 40 GHz	**August 2018 – October 2019** Tests start after integration

Optical-Efficiency Monitor Chip	**Efficiency Test Chip** Develop and test passive resonator chips to monitor as-fabricated propagation loss	**January 2019 – November 2019** Not started
Uniform 100-mK TES for Large Arrays	**100-mK TES Deposition Process** Develop deposition process for uniform 100-mK TES films on 150-mm wafers	**March 2019 – November 2019** Not started
Cosmic-Ray Frame Interactions at 100 mK	**Particle Interactions at 100 mK** Extend cosmic-ray testing to 100 mK	**January 2018 – December 2019** Testbed upgraded to 100-mK operation

Table 1. *Project milestones, schedule, and status by topic.*

Publications

1. B.M. Sutin et al., "*PICO – The Probe of Inflation and Cosmic Origins*," SPIE, in press (2018)

2. P. Ade et al., "*Antenna-Coupled TES Bolometers Used in BICEP2, Keck Array, and SPIDER*," ApJ, **812**, 176B (2015)

3. BICEP2 and Keck Array Collaborations, "*BICEP2/Keck Array IX: New Bounds on Anisotropies of CMB Polarization Rotation and Implications for Axion-Like Particles and Primordial Magnetic Fields*," arXiv 1705.02523 (2017)

4. A.A. Fraisse et al., "*SPIDER: Probing the Early Universe with a Suborbital Polarimeter*," JCAP, **04**, 047 (2013)

5. J.M. Nagy et al., "*A New Limit on CMB Circular Polarization from SPIDER*", Astrophys. J., **844**, 151 (2017)

6. BICEP2 and Keck Array Collaborations, "*BICEP2/Keck Array VIII: Measurement of Gravitational Lensing from Large-Scale B-Mode Polarization*," ApJ, **833**, 228B (2016)

7. BICEP2/Keck Collaborations, "*Improved Constraints on Inflationary Gravitational Waves using BICEP2/Keck Data up to the 2015 Season in Conjunction with WMAP/Planck*," PRL, submitted (2018)

8. BICEP2/Keck Collaborations, "*Improved Constraints on Cosmology and Foregrounds from BICEP2 and Keck Array CMB Data with Inclusion of 95 GHz Band*," PRL, **116**, 1302B (2016)

9. BICEP2/Keck and Planck Collaborations, "*Joint Analysis of BICEP2/Keck Array and Planck Data*," PRL, **114**, 1301 (2015)

10. BICEP2/Keck Array Collaboration, "*BICEP2/Keck Array V: Measurements of B-Mode Polarization at Degree Angular Scales and 150 GHz by the Keck Array*," ApJ, **811**, 126B (2015)

11. BICEP2 Collaboration, "*BICEP2 III: Instrumental Systematics*," ApJ, **814**, 110B (2015)

12. BICEP2/Keck Array Collaboration, "*BICEP2/Keck Array IV: Optical Characterization and Performance of the BICEP2 and Keck Array Experiments*," ApJ, **806**, 206B (2015)

13. A. Soliman et al., "*Design and Performance of Single/Wide Band Corrugated Walls for the BICEP Array Detector Modules at 30/40 GHz*", SPIE, in press (2018)

14. R. Gualtieri et al., "*SPIDER: CMB polarimetry from the edge of space*," to appear in Journal of Low Temperature Physics (2018)

15. J.P. Filippini, "*Cosmic Rays in SPIDER and Space*", B-mode from Space Workshop, Berkeley (Dec. 2017)

16. B.P. Osherson, "*Cosmic Ray Response of TES Arrays*," PICO Collaboration Science Meeting, Minneapolis (May 2018)

For additional information, contact James J. Bock: *james.j.bock@jpl.nasa.gov*

High-Efficiency Feedhorn-Coupled TES-based Detectors for CMB Polarization Measurements

Prepared by: Edward J. Wollack (PI; GSFC), David T. Chuss (Villanova University), Kevin L. Denis and
S. Harvey Moseley (GSFC), Karwan Rostem (GSFC, JHU), and Tobias A. Marriage and Charles L. Bennett (JHU)

Summary

The relic radiation from the Big Bang, the Cosmic Microwave Background (CMB), has provided a Rosetta stone for deciphering the content, structure, and evolution of the early universe. Our current theoretical understanding suggests that the universe underwent a rapid exponential expansion, called "Inflation," in the first fraction of a second. Such an inflationary epoch would result in an observable stochastic background of gravitational waves that impress a faint polarized signature on the CMB. The cosmological importance of undertaking this measurement was highlighted in the 2010 National Research Council Decadal Survey, "*New Worlds, New Horizons in Astronomy and Astrophysics*" (NWNH) [1]. NASA consequently recognized characterization of the CMB as a high-priority science objective and a dedicated Inflation Probe (IP) mission was called out in the NASA Astrophysics Roadmap, "*Enduring Quests, Daring Visions*" [2]. These efforts are international in their scope, with collaborative mission concepts under consideration by both the Japanese and European Space Agencies. The development of enabling technologies, including large-format focal planes, for space-borne polarization missions is a priority of the NASA Physics of the Cosmos (PCOS) technology roadmap.

This two-year technology maturation effort, initiated by the Strategic Astrophysics Technology (SAT) program in January 2016, focuses on the implementation of polarization-sensitive focal-plane arrays that are compatible with the space environment. We have developed and demonstrated superconducting Transition-Edge Sensor (TES) detectors that utilize a unique combination of highly symmetric electromagnetic design elements and single-crystal silicon that results in high transmission efficiency, the required sensitivity, and low cross-polarization response. Our objective is to advance these devices to a Technology Readiness Level (TRL) of 6.

Background

The polarized signature of Inflation in the CMB offers an important tool to investigate the physics of the inflationary epoch of the early universe. Discovery of this signature would provide the first direct evidence for Inflation and would rule out most competing explanations for the initial conditions of the early universe. Characterization of this signal provides a path to probe and quantify the physics of the first $\sim10^{-32}$ second of the universe, when energy scales vastly exceeded those accessible to current Earth-bound particle accelerators.

The measurement is arguably challenging, as the polarized signal from Inflation is anticipated to be faint, likely a mere $\sim10^{-8}$ of the 2.725 K isotropic component of the CMB. High sensitivity is a prerequisite; however, any mission that targets this measurement will also have to distinguish this minute polarized signal from both instrumental effects and other astrophysical sources. This requires high sensitivity and stability, multiple spectral bands for astrophysical foreground removal, control over potential systematic measurement and calibration errors, and compatibility with unique space-borne environmental conditions. Large detector arrays as well as development of calibration

and observational techniques to achieve these instrumental attributes are key enabling technology considerations. We have developed a sensor architecture that addresses these needs of an IP mission.

The basic design and the fabrication processes that have been developed have been reported in the literature [3-5]. Figure 1 provides an illustration of the architecture. Radiation from the optics is coupled by the feedhorn of each sensor into microstrip circuitry. Each linear polarization is coupled to an independent microstrip line, filtered to set the desired spectral passband, and detected in a TES.
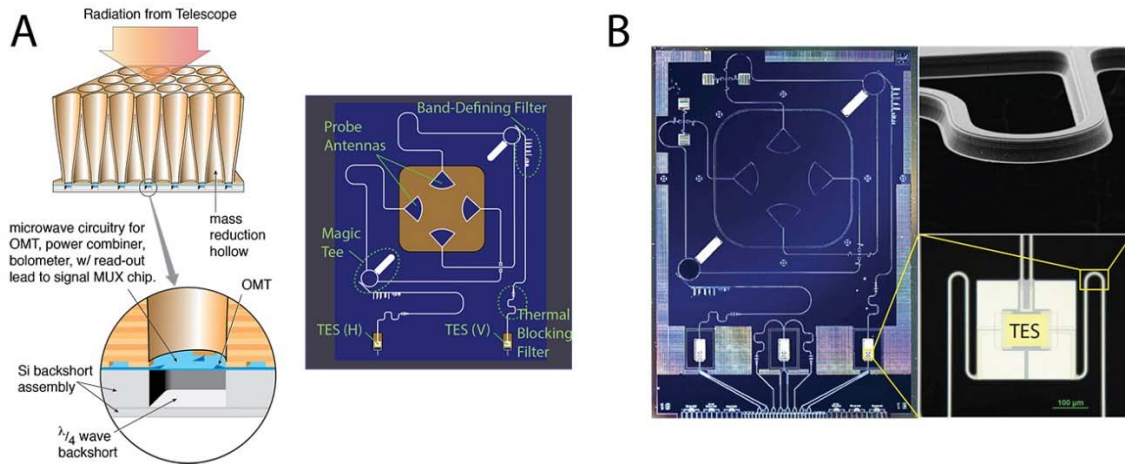
Fig. 1. (A) *The detector architecture combines the excellent beam-forming properties of feedhorns with the sensitivity of TES devices (MUX, multiplexer; OMT, ortho-mode transducer).* (B) *Photographs of the various parts of a device are shown.*

This configuration directly addresses the requirements of the IP mission as follows:

- **Polarization Sensitivity**: The symmetric planar OMT coupled scalar feedhorn ensures that each polarization has symmetric beams and high isolation over the full spectral band.

- **Sensitivity**: The TES bolometers operate at ~150 mK to ensure that the noise limit is set by the fluctuations in the CMB when operated in an appropriately stabilized space-borne system. In addition, the signal-mode sensor's large fractional bandwidth (60%) and high transmission efficiency (~90%) enable improved throughput relative to alternative implementations. The architecture is demonstrably scalable to the large focal planes required for an IP mission.

- **Systematic Error Control**: On-chip thermal blocking and bandpass filters ensure that the spectral band is well-defined for radiation coupling through the optics. Boxed microstrip and electrical closeouts for the TES detectors ensure that stray (out-of-band) radiation does not couple directly to the detector. The design has been scaled to three broadband designs that span the CMB spectrum. Multiple spectral channels will be necessary to separate the CMB signal from astrophysical foregrounds such as galactic dust and synchrotron radiation. A highly uniform dielectric layer provides the control required to realize broadband circuit elements across the array reliably.

- **Prevention of Surface and Deep Dielectric Charging**: Damage can occur from interaction between exposed dielectric surfaces and ambient space plasma. The conductive elements in the design, including the feedhorns and integrated degenerately doped silicon package, greatly limit exposure of dielectric structures to energetic electrons in the environment. In addition, the comprehensive filtering strategy, stray light control, and metallic beam-forming elements minimize the number of quasi-optical dielectric elements required by the instrument design.

- **Mitigation of Cosmic-Ray Events**: High-energy ionizing particles that interact electromagnetically with the detector have the potential to induce signal contamination. It is impractical to mitigate

cosmic-ray events via shielding. The approach adopted here is to implement structures having simple (easily understood) and fast thermal response, to reduce the affected portion of the data.

The basic operation of these detectors has been demonstrated at 40 GHz and is currently being employed in a ground-based telescope. This work focuses on extending their capabilities through a series of architectural improvements and corresponding validation.

Objectives and Milestones

This development effort centers on three targeted improvements in the focal-plane architecture. The first is to extend stray-light rejection bandwidth up to the 700-GHz gap frequency of the superconducting niobium circuitry. Measurements indicate that the achieved limit is ~500 GHz, limited by the closeout approach adopted in the current generation of device structures. This response has been refined by implementing vias in the silicon substrate that enable the micro-machined backshort assembly to be bonded directly to the ground plane. These vias complete the electromagnetic closeout of the detector and eliminate unintended coupling paths for out-of-band radiation. Second, we implemented direct access to the microwave ground plane to provide greater signal fidelity. This architectural improvement has been demonstrated to improve the noise performance of the devices in a prototype structure. The final architectural improvement extends the use of "crossovers," which allow the microstrip from waveguide-coupling probes to be routed on-chip to higher frequencies.

In our 40- and 90-GHz detectors, this detail has been handled using a novel "via-less" crossover [6]. To extend these design concepts to higher frequencies, we implemented "air-bridge" crossovers, in which one line crosses over the other with an air gap between them. Efforts are also underway to enhance the TES topology and device thermalization. In addition, fabrication-process improvements were targeted to improve yield, reliability, and uniformity.

Progress and Accomplishments

Fabrication processes for the ground-plane contacts and backshort assembly vias (Fig. 2) have been developed and validated. The ground-plane contacts and backshort-assembly vias have been integrated into detector arrays at 90 GHz (Fig. 3) and have passed continuity and environmental tests. These features have also been implemented in the dichroic 150/220-GHz detector designs, and are currently in production (Figs. 4 and 5). Air-bridge crossover designs have been fabricated and tested [7]. In addition, the via-less crossover has been refined and integrated into detector arrays. The TES membrane thermal design has been improved in both the 90- and 150/220-GHz arrays. This improvement decreases the thermalization time scale for the membrane and leads to improved noise performance at low frequencies.
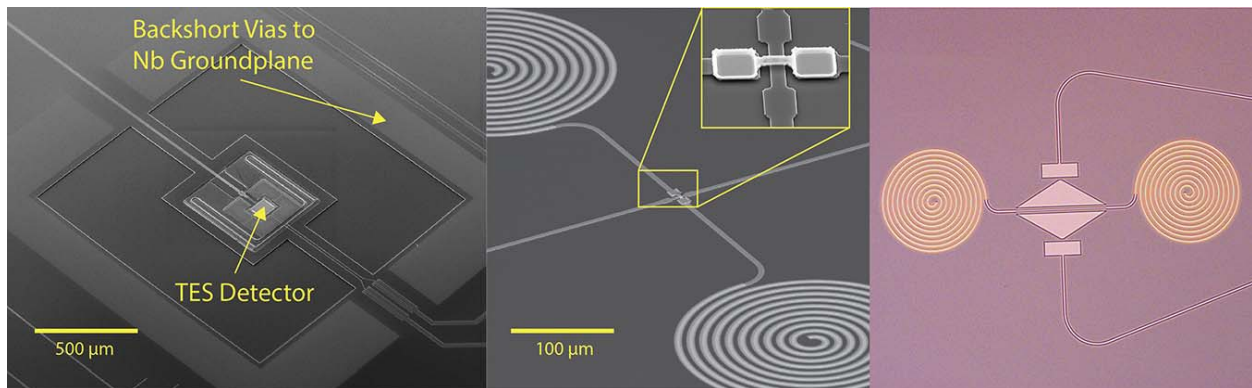
Fig. 2. Left: *Backshort vias are used to connect the backshort assembly wafer directly to the detector wafer ground plane. This forms a complete electromagnetic shield to mitigate stray radiation from coupling to the detector.* Center: *The air-bridge crossover fabrication process has been demonstrated. These millimeter-wave circuit structures on silicon have limited radiation loss and increased coupling bandwidth.* Right: *An alternate via-less crossover approach has been designed and fabricated.*

Fig. 3. Left: *A 90-GHz 37-element array.* Center: *A complete 90-GHz sub-array prototype module.* Right: *Focal plane of the Cosmology Large Angular Scale Surveyor tiled with 7 sub-array modules.*
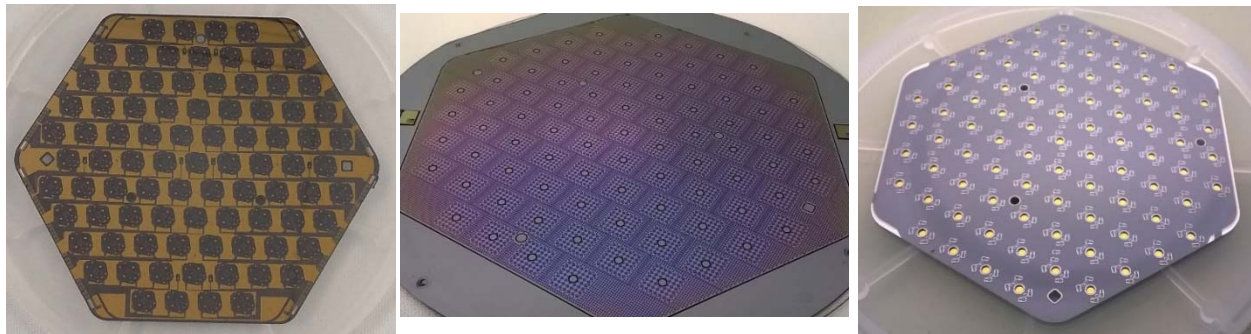

Fig. 4. *Dichroic arrays operating at 150/220 GHz have been fabricated.* Left: *A complete sub-array prototype is shown.* Center: *Micro-machined photonic choke wafer.* Right: *Micro-machined backshort assembly*

A free-space cryogenic flux calibrator has been designed, fabricated, and tested. This enables the testing of the detector efficiency and loading for an entire sensor module simultaneously. The calibrator consists of ~400 absorbing pyramids in a Cartesian tiling and is ~100 mm in diameter (Fig. 6). It is constructed using a silicone molding process to cast a loaded epoxy into the desired shape and to incorporate a copper backplate for thermal control and mechanical connectivity. The calibrator performance was measured and found to agree with the design (< –30 dB reflection from 80-350 GHz). This effort has incorporated the work of undergraduate students and the results were published [8]. Similarly, advances in superconducting modeling [9] and optical material characterization [10] have also been performed and documented under this under this effort.
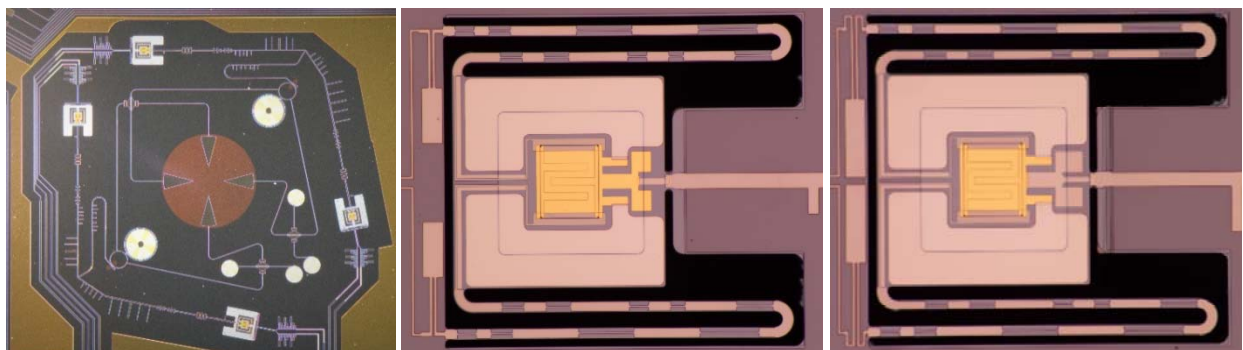
Fig 5*: Left:* Dichroic pixel operating at 150/220 GHz. *Center and Right:* TES termination designs optimized for 150 GHz and 220 GHz respectively.*
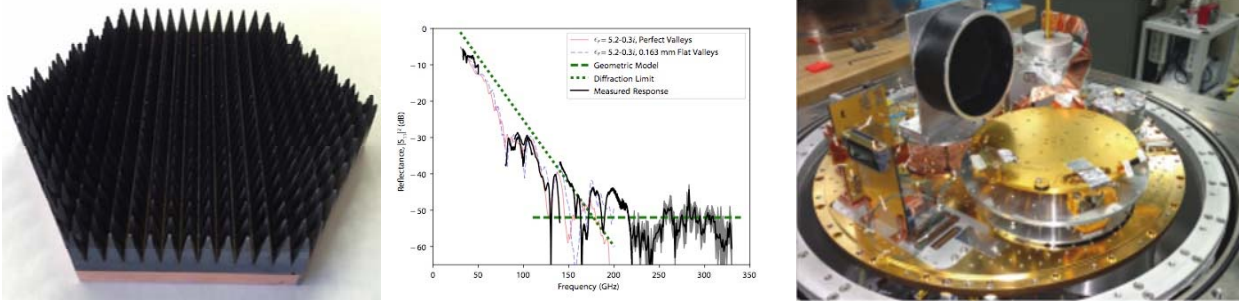
Fig 6*: A cryogenic calibrator developed under this SAT effort (Left) is currently being used to validate full modules (Right). Details of the modeled and measured calibrator response (Center) can be found in [8].*

As a component of this effort, a multi-channel readout system has been commissioned for validating both the 90-GHz and 150/220-GHz arrays [11]. A seven module focal plane operating at 90 GHz has been fabricated, assembled, and is currently fielded in the Cosmology Large Angular Scale Surveyor (CLASS) instrument [12] to achieve and demonstrate the TRL objectives for this technology. Initial 150/220 GHz wafers have been developed and are currently being characterized.

Path Forward

Targeted test structures are planned to investigate the sensors' electron-phonon coupling properties in greater detail, with an eye toward improved device performance and achieving greater control over key fabrication parameters. In addition to the performance improvements achieved on individual devices, these research efforts have driven the maturation of the processes required to realize large focal planes with improved reliability and yield. Development will continue on the 150/220 GHz wafers, and a focal plane will be constructed for integration into CLASS.

References

[1]   Blandford et al., "*New Worlds, New Horizons in Astronomy and Astrophysics*," National Academy of Sciences (2010)

[2]   National Aeronautics and Space Administration, "*Enduring Quests, Daring Visions*," Astrophysics Roadmap (2013)

[3]   D.T. Chuss et al., "*Cosmology Large Angular Scale Surveyor (CLASS) Focal Plane Development*," Journal of Low Temperature Physics, 101007/s10909-015-1368-9 (2016)

[4]   K.L. Denis et al., "*Fabrication of Feedhorn-Coupled Transition Edge Sensor Arrays for Measurement of the Cosmic Microwave Background Polarization*," Journal of Low Temperature Physics, 10.1007/s10909-015-1366-y (2016)

[5]   K. Rostem et al., "*Scalable Background-Limited Polarization-Sensitive Detectors for mm-wave Applications*," Proc. SPIE, **9153**, 91530B (2014)

[6]   K. U-yen, E.J. Wollack, S.H. Moseley, T.R. Stevenson, W.-T. Hsieh, and N.T. Cao, "*Via-less microwave crossover using microstrip-cpw transitions in slotline propagation mode*," in Microwave Symposium Digest, MTT '09, IEEE MTT-S International, 1029-1032 (2009)

[7]   K.L. Denis, A.D. Brown, M.P. Chang, R. Hu, K. Rostem, K. U-Yen, and E.J. Wollack, "*Fabrication of Superconducting Vacuum-Gap Crossovers for High Performance Microwave Applications*," IEEE Transactions on Applied Superconductivity, **27**, 4, 1-4 (2017)

[8]   D.T. Chuss, K. Rostem, E.J. Wollack, L. Berman, F. Colazo, M. DeGeorge, K. Helson, and M. Sagliocca, "*A Cryogenic Thermal Source for Detector Array Characterization*," RSI, **88**, 104501 (2017)

[9]   K. U-Yen, K. Rostem, and E.J. Wollack, "*Modeling Strategies for Superconducting Microstrip Transmission Line Structures*," IEEE Transaction on Applied Superconductivity, **28**, 6, 1-5 (2018)

[10] K.R. Helson, K.H. Miller, K. Rostem, M. Quijada, and E.J. Wollack, "*Dielectric Properties of Conductively Loaded Polyimides in the Far Infrared*," Optics Letters (submitted 2018)

[11] K. Rostem, et al., "*Silicon-based antenna-coupled polarization-sensitive millimeter-wave bolometer arrays for cosmic microwave background instruments*," Proc. SPIE, **9914**, 99140D-99140D-10 (2016)

[12] K. Harrington, et al., "*The Cosmology Large Angular Scale Surveyor*," Proc. SPIE, **9914**, 99141K, (2016)

For additional information, contact Edward J. Wollack: *Edward.J.Wollack@nasa.gov*